CARRIER DYNAMICS STUDY OF ZnSe AND ZnSe BASED QUANTUM WELL STRUCTURES BY USING TIME-RESOLVED SPECTROSCOPY

BY

LI WANG

A DISSERTATION PRESENTED TO THE GRADUATE SCHOOL OF THE UNIVERSITY OF FLORIDA IN PARTIAL FULFILLMENT OF THE REQUIREMENTS FOR THE DEGREE OF DOCTOR OF PHILOSOPHY

UNIVERSITY OF FLORIDA

1996

ACKNOWLEDGEMENTS

First of all, I would like to thank my research advisor, Dr. Joseph Simmons, for all his guidance and support on this work in many ways. The experience of working with him has been extremely rewarding.

Secondly, I would like to express my gratitude to Dr. Robert Park and Minyong Jeon for fabricating the MBE samples used in this work. This work wouldn't be possible without their samples.

Finally, I want to thank my parents, my brother and sister for their love and encouragement which has always been a source of inspiration.

TABLE OF CONTENTS

ACKNOWLEDGEMENTS.....ii

ABSTRACT.....v

CHAPTERS

1 INTRODUCTION TO CARRIER DYNAMICS AND ITS APPLICATION TO SEMICONDUCTOR RESEARCH..... 1

Overview 1
Photoexcited Processes of Carriers In Semiconductors..... 4
Optical Probe As a Tool to Study Carrier Dynamical Processes..... 6
Applications of Carrier Dynamics Study To High Frequency Response Device Design..... 8
Future Development And Outlook..... 10

2 COMMON EXPERIMENTAL TECHNIQUES USED TO STUDY CARRIER DYNAMICS IN SEMICONDUCTORS AND THEIR BASIC PRINCIPLES..... 12

Coherent Time-resolved Spectroscopy..... 13
Incoherent Time-resolved Spectroscopy..... 30
Selection Criteria of Suitable Techniques..... 49

3 REVIEW ON PAST PROGRESS ON SEMICONDUCTOR CARRIER DYNAMICS STUDY 52

Semiconductor Bulk And Films..... 52
Semiconductor Quantum Size Structures..... 65
Semiconductor Devices..... 75

4 CARRIER DYNAMICS INVESTIGATION OF II-VI SEMICONDUCTOR FILMS AND QUANTUM STRUCTURES (ZnSe AND CdZnSe/ZnSe MULTIPLE QUANTUM WELLS)..... 80

Properties And Applications of II-VI Semiconductors..... 80
Material Structures Studied..... 85
Fabrication By Molecular Beam Epitaxy..... 87

5 EXPERIMENTAL TECHNIQUES USED AND THEIR SETUPS.....94

Ultrafast Ti:Sapphire Laser System As The Excitation Source: General Characteristics And Operating Principles..... 94
Population Mixing (or Picosecond Excitation Correlation Spectroscopy): Principle And Experimental Setup..... 116
Transient Differential Absorption: Principle And Experimental Setup..... 122

6 EXPERIMENTAL RESULTS ON QUANTUM WELLS AND THEORETICAL ANALYSIS.....129

Quantum Mechanical Calculation of Band States.....129
Room Temperature Results..... 150
Quantum Mechanical Analysis On Room Temperature Results...152
Low Temperature Results: Exciton And Biexciton Dynamics..... 168
Analysis On Low Temperature Data..... 169
Temperature Dependence Study of Carrier Lifetime 192
Lasing Mechanism in CdZnSe/ZnSe Diode Lasers..... 196
Optical Degradation Study..... 206
Hot Phonon Effect..... 212
Carrier Tunneling Study..... 217
Transient Differential Absorption Results..... 222

7 EXPERIMENTAL RESULTS ON EPITAXIAL FILMS AND BULK CRYSTAL..... 231

Room Temperature Results: Free Carrier Dynamics..... 231
Low Temperature Results: Free And Bound Exciton Dynamics... 237

8 CONCLUSIONS AND FUTURE WORK..... 251

Conclusions of Carrier Dynamics Study 251
Future Work.....255

REFERENCES..... 257

BIOGRAPHICAL SKETCH..... 272

Abstract of Dissertation Presented to the Graduate School
of the University of Florida in Partial Fulfillment of the
Requirements for the Degree of Doctor of Philosophy

CARRIER DYNAMICS STUDY OF ZnSe AND ZnSe BASED QUANTUM WELL STRUCTURES BY USING TIME-RESOLVED SPECTROSCOPY

BY

LI WANG

AUGUST, 1995

Chairman: Dr. Joseph. H. Simmons
Major Department: Materials Science and Engineering

ZnSe and ZnSe based quantum well structures are potential candidates for blue/green light emitting devices and optical switches. Carrier dynamics studies of these structures are important in evaluating device performance as well as understanding the underlying physical processes. In this work, a carrier dynamics investigation was conducted on ZnSe bulk and $Cd_xZn_{1-x}Se/ZnSe$ (x=0.2 and 0.25) quantum well structures grown by molecular beam epitaxy (MBE) at both room temperature and low temperatures. At room temperature, the dynamics of free carriers provides insights into the band-to-band transition dynamics; while at low temperature, the dynamics of excitonic processes provides detailed information on carrier thermalization processes such as carrier-carrier interactions, carrier-phonon interactions and plasmon-phonon coupling. Two techniques were used in this study: a time-resolved photoluminescence technique called population mixing (also called

excitation correlation spectroscopy), and a femtosecond pump-probe technique called transient differential absorption. Both doped and undoped ZnSe films were studied to determine the role of dopants on carrier dynamics. Multiple quantum well (MQW) structures with different barrier widths (50-200Å) and well widths (25-100Å) were studied to determine the effect of carrier localization and tunneling on carrier dynamics. Excitation over a wide range of carrier densities (10^9-10^{13}/cm^2) was used to study hot carrier effects such as hot-phonon effect, carrier-carrier collisions and excitonic molecule formation. Carrier recombination and thermalization dynamics in three-dimensional bulk and two-dimensional quantum wells were compared to examine the difference in fundamental physics involved, such as much-enhanced oscillator strength, higher optical nonlinearity and stronger carrier screening of 2D structures. The most important result of studies on quantum wells is the observation of biexcitons (or excitonic molecules). Biexcitons are formed due to condensation of a high density of excitons, and its emission and decay characteristics are closely related to those of the excitons. Biexciton gain was proposed as the mechanism of stimulated emission in these quantum well structures based on the lasing characteristics of CdZnSe/ZnSe MQW lasers at cryogenic temperatures. The most important result of bulk studies is the identification of different excitonic processes, such as various donor and acceptor bound excitons, by their characteristic temporal decay behaviors. The interest in studying these dynamic processes arises from the current development of diode lasers as well as ultrafast hot electron transistors and tunneling diodes.

CHAPTER 1

INTRODUCTION TO CARRIER DYNAMICS AND ITS APPLICATION TO SEMICONDUCTOR RESEARCH

Overview

Investigation of carrier dynamics plays a central role in modern semiconductor science. Properties of photoexcited carriers are determined by various interactions between carriers and other elementary excitations in the semiconductor. Therefore, investigation of excited carrier properties provide information about scattering processes that are of fundamental interest in the physics of semiconductors. Furthermore, these processes determine high-field transport phenomena in semiconductors and thus form the basis of operations of many ultrafast electronic and optoelectronic devices. The field of carrier dynamics thus provide a link between fundamental semiconductor physics and high-speed devices.

An important milestone in the field of carrier dynamics in semiconductors is the development of ultrafast optical spectroscopy. Optical excitation can create hot carriers and optical spectroscopy can provide information about the distribution function of excited carriers. Although transport measurements provide considerable information about various scattering processes in semiconductors, they are averaged over the carrier distribution functions. In contrast, optical techniques, by

providing the best means of determining the carrier distribution functions, allow one to investigate the microscopic scattering processes. A major advance in the field of optical spectroscopy came recently when ultrafast lasers with pulsewidths as short as 6fs became available. These lasers allow the investigation of the time evolution of carrier distributions on ultrashort time scales. Since different processes occur on different time scales, it became possible to isolate various scattering processes by appropriate choices of time windows.

The emergence of semiconductor quantum size structures grown by molecular beam epitaxy in late 1970s has changed the direction of the field of carrier dynamics considerably. Quantum well (QW) heterostructures consisting of thin layers of semiconductors with different bandgaps have many unique properties, such as resonant tunneling and ballistic transport. These properties have attracted much research attention due to potential novel device applications besides the fundamental interest. In fact, progress in understanding these nanostructures has led to the development of new fast response devices such as modulation-doped field-effect transistors and resonant tunneling diodes.

Electronic states in a quantum confined system are different from those in a bulk semiconductor. The conduction and valence bands break up into various subbands as a result of confinement. The wavefunctions of the confined states penetrate into the barrier for finite barrier heights but vanish at the boundary for infinitely high barriers. For thick barriers, each well in a multiple quantum well structure can be treated as independent of other wells. With decreasing barrier

thickness, the wavefunctions of adjacent wells overlap with each other and lead to the formation of minibands, with interesting transport properties. While the electron states are simple, the hole states are extremely complicated in quasi-2D structures. The valence bands in bulk zinc blende semiconductors are nonparabolic and anisotropic. Inclusion of quantization effects leads to very complicated structures for heavy and light hole subbands. A detailed understanding of hole bands is clearly necessary in order to understand carrier dynamics involved.

Fundamental carrier dynamic processes of interest in semiconductor nanostructures include electron-phonon interactions, many-body physics, hot-phonon effects, carrier tunneling, and quantum transport. Among these processes, the last two are possessed only by nanostructures. Optical spectroscopies such as ultrafast luminescence, femtosecond pump-and-probe transmission, Raman scattering, and coherent four-wave mixing are very valuable tools for the investigation of these processes. Each of these techniques provides detailed information about a specific process, for example, luminescence reflects carrier recombination dynamics, pump-probe transmission reflects carrier-carrier scattering dynamics, Raman scattering reflects phonon dynamics, and four-wave mixing reflects coherent dynamics, therefore, the combination of these techniques will provide us with a whole picture of carrier relaxation dynamics.

Most research efforts in the past have been focusing on GaAs and GaAs based quantum well structures. Tremendous progress has been made and is reflected through the development of a new class of high frequency response

devices and new advances in theoretical physics. New materials such as ZnSe have attracted much attention recently due to their potential applications as light emitting devices (lasers and light emitting diodes) and optical switches. As a result, a fundamental understanding of these materials is of immediate practical importance besides fundamental physics interest. This carrier dynamics study on ZnSe and ZnSe based quantum structures will provide us with insights into the properties of this material.

Photoexcited Carrier Processes in Semiconductors

Excitation. When a typical III-V or II-VI semiconductor is excited by ultrafast laser pulses with an energy equal to or larger than the semiconductor bandgap, electron and hole pairs are created through interband absorption. In general, one excites electrons from all three valence bands in such semiconductors. The distributions of photoexcited electrons and holes are determined by the frequency and spectral width of the laser pulse and the dispersion of the conduction and the valence bands.

Thermalization. The photoexcited semiconductor goes through several nonequilibrium states before it returns to thermal equilibrium. Immediately following photoexcitation, the photopopulated electronic states still retain coherence among themselves and with the electromagnetic radiation. If the dephasing time, or the time to lose the coherence, is faster than any other relaxation process, then the carrier distribution function (DF) is nonthermal even after the photopopulated states have lost their coherence. Subsequently, the energy in the carrier system is

redistributed, primarily as a result of carrier-carrier collisions, and the initial nonthermal distribution approaches a thermalized (i.e. Fermi-Dirac type) distribution with characteristic temperatures T_e and T_h for electrons and holes, different from the lattice temperature T_L. Electrons and holes then thermalize with each other by electron-hole collisions, so that the plasma can be described by a single temperature T_c higher than T_L. The next process is the cooling of this plasma to the lattice temperature by interaction with phonons. For $T_c > 40K$, this occurs primarily through the interaction of the high-energy tail of the distribution with optical phonons. For $T_c < 40K$, this occurs through the interaction of the low energy tail of the distribution with acoustic phonons.

Recombination. Finally, the photoexcited carriers have the same temperature as the lattice temperature and recombine radiatively to bring the semiconductor back to thermal equilibrium conditions, giving off photons with energy close to the bandgap. The electron-hole recombination rate is determined by Fermi's golden rule which relates it to electron and hole densities of states, and the interaction Hamiltonian between electron and hole wavefunctions.

Trapping. In the presence of traps due to lattice imperfections or impurities, recombination kinetics will be more complicated. Traps are metastable states which capture an electron from a higher-energy state and retain it for a considerable time at the end of which the electron is released back to the higher-energy state, from which it can make a transition to a much lower-energy state (i.e., valence band) either radiatively or non-radiatively. It has been shown experimentally that the

carrier trapping time can be as long as in the order of milliseconds (1, p. 379). Carrier trapping is responsible for the time delay in lasers and quenching of light emission in most semiconductors.

The sequence of events and the different regimes, with some approximate time scales, are illustrated in Figure 1-1 (2). It is important to note that various important time scales depend on many parameters (e.g. the density and energy of carriers) and overlap with each other, so the relaxation processes discussed above are not sequential but overlap in time.

Optical Probe as a Tool For the Study of Carrier Dynamic Processes

Photoexcitation of carriers in semiconductors induces processes such as absorption and light emission, which are fundamentally related to the carrier energy and momentum distribution. The temporal evolution of these processes reflects the dynamics of nonequilibrium relaxation processes and is accessible to optical probes such as transient photoluminescence (for probing emission) and transient absorption (for probing absorption). Luminescence measurements provide information on the recombination kinetics of electrons and holes as well as the occupation of near-band-edge states. Absorption pump-probe experiments provide information about excitonic effects and carrier-carrier scattering with excitation near the bandgap. With excitation far above the bandgap, they provide information on processes such as intervalley scattering, and intersubband scattering. With recent advances in the generation of ultrashort pulse lasers having pulsewidths in the

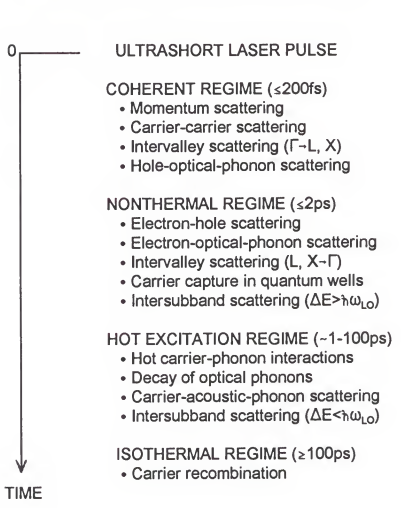

Figure 1-1 A semiconductor photoexcited by an ultrashort pulses passes several regimes before it returns to thermodynamic equilibrium. Various scattering processes and approximate durations of various regimes for photoexcited carriers are indicated. Scattering processes depend on several parameters, so various regimes overlap in time (from ref. 2).

femtosecond time regime, ultrafast optical spectroscopy has become a very powerful tool for investigating the dynamics of carrier relaxation. Significant progress has been made during the last decade in this field both theoretically and experimentally. Carrier thermalization processes which occur extremely fast (less than one picosecond) such as carrier-carrier scattering and plasmon-phonon scattering have been resolved and provide insights into the underlying fundamental physics. New experimental results modify and refine current theories on nonequilibrium physics. For example, the roles of dynamic screening, collision broadening, band non-parabolicities, and hot phonon effect at high carrier densities have been much better understood in semiconductors (3-7).

Applications of Carrier Dynamics Study to High Frequency Response Device Design

To meet the demand for high speed device operation, the study of carrier dynamics is essential. Semiconductor devices such as photoconductors, photodetectors, optical modulators, lasers, resonant-tunneling hot-electron transistors, resonant tunneling diodes, and ultrafast quantum interference switches compose a major part of integrated circuitry technology. To improve the switching speed of these devices and evaluate device performance, understanding carrier dynamics at ultrafast time scales is necessary. The carrier relaxation processes of all material systems responsible for the operation of each device have to be well understood from a fundamental physics point of view in order to optimize the device design. In the past, a majority of semiconductor devices were made from bulk

materials, and the device performance was determined by the bulk properties of semiconductors. Due to advances in fabrication technology such as molecular beam epitaxy, metalorganic chemical vapor deposition, semiconductor nanostructures can be grown with very high quality. Compared to their bulk counterparts, these quantum confined nanostructures have higher optical nonlinearities as well as unique properties not available in bulk, such as the possibility of ballistic transport and ultrahigh frequency response. An investigation of the physics of carrier dynamics in these nanostructures has attracted much interest in recent years due to their desirability in device applications. It has been shown that devices made from these semiconductor nanostructures lead to improved performance in many instances (8). An example follows.

Resonant-tunneling hot-electron transistors (RHETs) are unipolar transistors which use semiconductor heterojunctions. Their very short carrier transient time and low forward-bias emitter capacitance allow the possibility of using the device as an ultimate high-speed device. Unipolar transistors also can have lower power consumption than bipolar transistors, due to decreased supply voltages. However, low-temperature operation is required to achieve higher current gains and higher collector breakdown voltages. In 1985, Yokoyama et al. demonstrated RHETs using a resonant-tunneling barrier as a hot-electron injector (9). Besides functioning as a hot-electron transistor, the RHETs exhibit a negative-transconductance region, which enables them to be used as a new functional device, reducing the number of transistors in the circuit. In recent years, RHETs using InGaAs based materials

have achieved significantly improved performance and small integrated circuits based on them are under development. For a detailed review, see Chapter V.2 in reference 2. A schematic of an InGaAs-In(AlGa)As RHET is shown in Figure 1-2. In order to achieve very high frequency operation, theoretical models simulating the device operation characteristics have been built to understand the physics of fundamental processes involved. For example, in order to model hot electron transport in the base region, in addition to conventional scattering mechanisms, such as ionized impurity scattering, acoustic-phonon scattering, alloy scattering, the coupled plasmon-LO-phonon scattering and electron-electron scattering have to be included since carriers are hot and far from equilibrium. The transport time of hot electrons through the base region is determined by hot carrier relaxation mechanisms which can be determined from the evolution of energy and momentum distribution. Optimum conditions (base doping concentration, base dimension, etc.) were found from the modelling calculations, and superior performance devices (<2ps response time, 100GHz cutoff frequency) were developed (2).

Future Developments and Outlook

The study of carrier dynamics has played an important role in semiconductor research in the past and will continue for the future for both practical device applications and fundamental physics. As devices are getting smaller, down to the submicron size, the electric field can be extremely high, consequently, the carrier temperature will be very hot. Therefore, understanding the exact mechanisms of hot carrier relaxation and transport becomes very important in order to improve device

performance and design. Ultrafast optical spectroscopy is a very powerful tool for obtaining very valuable information on the carrier relaxation dynamics in a material. With the development of high quality, wide-wavelength range ultrashort laser pulses (<7fs, from UV to IR), carrier dynamics studies can be carried out using time-resolved optical spectroscopy in a variety of materials having applications from photonics to electronic transport. In the past few years, novel devices utilizing electron ballistic transport effects and quantum interference effects have emerged as a new class of ultrafast switches. In the meantime, theories on the physics of hot carrier dynamics have been advanced and refined. The excitement in this field will continue and advances will move at a much faster pace in the future.

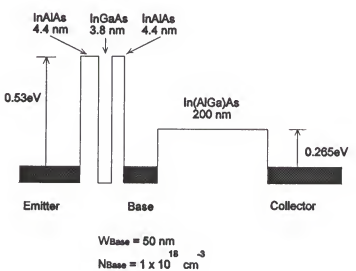

Figure 1-2 Band diagram of the InGaAs-In(AlGa)As resonant-tunneling hot-electron transistors (RHET). (from ref. 2)

CHAPTER 2
COMMON EXPERIMENTAL TECHNIQUES USED TO STUDY CARRIER DYNAMICS IN SEMICONDUCTORS AND THEIR BASIC PRINCIPLES

Dynamic interactions can be directly studied in the temporal domain by time resolved spectroscopy. The development of ultrafast lasers and techniques has advanced to the stage at which direct observation of dynamical processes can be measured in a femtosecond time scale. In the last few years, technological advancements have improved the resolution of photodetectors and photodiodes to less than 10ps. These photodetectors can be used to measure the profile of luminescence in real time. However, various techniques have been developed for time resolved spectroscopy with resolution and sensitivity beyond the time response of the fastest photodetectors and oscilloscopes. The resolution in most cases is limited by the pulse duration of the laser used, which can be in the femtosecond regime. There are two classes of time-resolved spectroscopy: coherent spectroscopy and incoherent spectroscopy. Coherent techniques give information on dynamic processes in the time domain as well as on the line-widths and line positions in the frequency domain. The coherent dephasing time (T_2) is the time that it takes for the photoexcited carriers to lose coherence among themselves and with the electromagnetic radiation. Incoherent techniques give information on dynamical processes in the time domain only. The incoherent dephasing time, also called energy relaxation time (T_1), is the total time that it takes for the carriers to relax to

equilibrium. Carrier relaxation goes through the coherent regime first then into the incoherent regime. The coherent dephasing time in semiconductors is normally less than 10ps, while the incoherent decay time can be in the range from a few picoseconds to nanoseconds or even microseconds. Various experimental techniques are available in each regime and they are discussed in detail next.

Coherent Time-Resolved Spectroscopy

The theoretical model of coherent spectroscopy is described by the density matrix formalism, and a rotating frame approximation is used to solve the wave equation. The details can be found in p.236 in reference 10. Ultrafast coherent techniques include one-pulse excitation, two-pulse excitation, and three-pulse excitation configurations. The schematics of these configurations is illustrated in figure 2-1. In the one-pulse excitation scheme, one short laser pulse transverses the sample. After the excitation of the system by the pulse with wave vector k_a radiation is emitted from the sample in the same direction. For homogeneously broadened transitions, the polarization decays exponentially with dephasing time T_2, while in the case of inhomogeneously broadened transitions the polarization decays much faster due to the interference of the different resonant frequencies. Single excitation pulse coherent techniques are very well established in ultrafast spectroscopy. An example is coherent Stokes and Anti-stokes Raman spectroscopy.

In the two excitation pulse scheme, two excitation pulses (k_a and k_b) separated by a time delay t_1 are applied to the system. The coherent signal

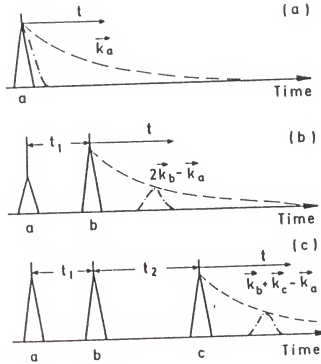

Figure 2-1 Schematic of various coherent techniques. The electric field pulses (solid triangles) excite the sample. The resulting coherent signal is shown for homogeneously broadened transitions (dashed curves), and for inhomogeneously broadened transitions (dash-dotted curves). (a) A single excitation pulse with wave vector k_a. Homogeneously broadened transitions lead to an exponential decay with dephasing time T_2, while inhomogeneous broadening induces a faster decay. (b) Two excitation pulses a and b with wave vectors k_a and k_b give echoes in the direction $2k_b$-k_a. For inhomogeneously broadened transitions the echo is emitted at time $t=t_1$. The echo amplitude measured as a function of t_1 allows determination of the dephasing time T_2. (c) When three excitation pulses are used the coherent signal emitted in the direction $k_b+k_c-k_a$ allows the determination of the dephasing time T_2 and the energy relaxation T_1 (from ref. 10).

consists of three components: one from k_a emitting in the direction of k_a, one from k_b emitting in the direction of k_b, and the last one from a correlation effect (photon echo) emitting in the direction $2k_b$-k_a. For inhomogeneously broadened transitions, this echo is emitted at time $t - t_1$. The echo amplitude measured as a function of t_1 allows a determination of the dephasing time T_2. An example of this category is four-wave mixing.

For the three excitation pulse scheme, three excitation pulses separated in time by t_1 and t_2 are applied to the material. Coherent signals consist of single excitation signals, two-pulse echoes from each pair of the three pulses, and the so-called three pulse echo at time $t=t_1$ emitting in the direction of $k_a+k_b-k_c$. The addition of the third pulse allows the measurement of the dephasing time T_2 as well as the determination of the energy relaxation time T_1. An example for this last category is the three-pulse photon echo spectroscopy.

Time-Resolved Coherent Raman Scattering (CRS)

The Raman scattering process involves a nonlinear coupling between matter and electromagnetic radiation. A incident photon of energy $\hbar\omega_1$ is absorbed by the material while at the same time a scattered photon of energy $\hbar(\omega_1 \pm \omega_{rg})$ is emitted. The energy difference $\hbar\omega_{rg}$ is due to the absorption or emission of phonons, also called Raman mode quanta. If the emitted energy is less than the incident energy, we call it Stokes Raman scattering. Anti-Stokes Raman processes extract energy from the excited Raman mode. A Raman scattering level diagram is provided in figure 2-2 (11).

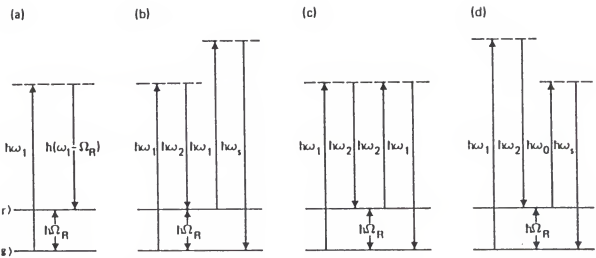

Figure 2-2 Level diagrams in Raman spectroscopy. (a) The spontaneous scattering mechanism operative in conventional Raman spectroscopy. (b) The process in coherent anti-stokes Raman spectroscopy (CARS). The output frequency is denoted ω_s and by convention $\omega_1>\omega_2$. Coherent Stokes Raman spectroscopy (CSRS) would have the same diagram with $\omega_1<\omega_2$. (c) The process operative in stimulated Raman gain (SRG) and the inverse Raman effect as well as the Raman-induced Kerr effect. (d) The process of four-wave mixing with three input frequencies. All resonances are at $\omega_1-\omega_2=\omega_{rg}$ (from ref. 10).

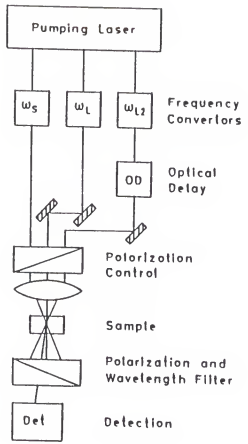

Figure 2-3 Experimental system used for time-resolved coherent Raman scattering. Synchronized pulses at frequencies ω_L, ω_s, ω_{L2} are generated by different frequency converters from one laser source. The pulses at ω_L and ω_s excite the sample via stimulated Raman scattering. The coherent excitation is monitored by the delayed (OD) probing pulses at ω_{L2}. The different beams cross in the sample at phase-matching angles. Polarization and wavelength filters separate the coherent signal from the excitation light (from ref. 10).

In time-resolved Raman spectroscopy, the sample is first excited by a pair of light pulses via transient stimulated Raman scattering, subsequently the degree of excitation is interrogated by a probe pulse, which is delayed in time with respect to the excitation pulses. The probe pulse monitors the coherent amplitude of the Raman scattering signal as the time delay is swept across an adjustable time interval and maps out the time dependence of the coherent signal. The temporal decay of the coherent signal gives the dephasing time of phonons. The experimental setup is shown in figure 2-3. A pumping laser source generates excitation and probe light pulses of very short duration at frequencies ω_L, ω_s, ω_{l2}, the exciting laser pulses are focused into the sample with a specific angle to generate the coherent signal. The probing light pulse at frequency ω_{l2} is delayed in the optical delay system OD relative to the excitation pulses and monitors the temporal profile of the coherent signal. The geometry of the exciting and probing beams has to be adjusted to obtain phase matching for the coherent probe-scattering process. The detection system is a highly sensitive photodetector, and the spectra of the coherently scattered light are analyzed using a spectrometer. In most experiments the signal intensities are much smaller than the intensities of the excitation pulses, so the coherently scattered light must be separated carefully from the incoming light beams by spectral and polarization filtering.

Four-Wave Mixing

Four-wave mixing is the most widely used time-resolved coherent technique. It is a two-pulse photon echo process. This process is symmetry-allowed in all

media and has found numerous applications in spectroscopic investigations with short pulses. When three laser beams at different frequencies ω_1, ω_2, ω_3 are mixed in the sample by the third-order nonlinear susceptibility, the coherently generated nonlinear signal can have the frequency $\omega_4 = |\omega_1+\omega_2-\omega_3|$. The inherent four-photon interaction involves the annihilation of the two quanta (ω_1,ω_2) and the creation of the two new photons (ω_3,ω_4): $\omega_1+\omega_2 = \omega_3+\omega_4$. The intensity of the new component I_4 is determined by the incident intensities (I_1, I_2, I_3) according to (10, p.64)

$$I_4 \propto const \cdot |\chi_3|^2 I_1 I_2 I_3 l^2 \left(\frac{\sin \Delta k l/2}{\Delta k l/2}\right)^2$$

The mismatch $\Delta k = |k_1+k_2-k_3-k_4|$, l denotes the interaction length. This equation refers to low intensity situation neglecting both depletion of incident radiation and stimulated amplification. Usually two instead of three incident fields are coupled by the four-photon interaction; i.e. photons of one field act twice, $\omega_1=\omega_2$ or $\omega_1=\omega_3$ corresponding to $I_1=I_2$ or $I_1=I_3$ in equation 2-1. The specific role that a frequency component plays in the interaction is determined by the mismatch Δk.

The general case involving three (or four) different frequency components ($\omega_1,\omega_2,\omega_3,\omega_4$) is called non-degenerate frequency mixing. In the fully degenerate case, all four frequency components are equal, however, the fields may still be distinguishable by their polarizations and/or beam directions. There also exists a third possibility involving two different frequencies: $\omega_1=\omega_3$, $\omega_2=\omega_4$. This situation, also called scattering from light-induced (or phase) grating, is referred to as partially degenerate four wave mixing. The wave vector diagrams for the three situations are

shown in figure 2-4 (10, p.65). For partial or totally degenerate four wave mixing, the phase matching condition $\Delta k=0$ is satisfied automatically due to the frequency degeneracy. The broken arrows in the figure represent the k vectors of the induced gratings which are often helpful in visualizing the nonlinear process. It is worth noting that the Raman process is a special case of four-wave mixing. Raman resonance occurs when $|\omega_1-\omega_3|=\omega_p$ and $|\omega_2-\omega_3|=\omega_p$. For a detailed theoretical treatment of the four-wave mixing processes, see Oudar and Shen (12), Ye and Shen (13).

Degenerate four-wave mixing (DFWM) is the most commonly used technique in time-resolved studies due to its experimental simplicity and automatic phase matching. In the case far from single or difference frequency resonances of $X^{(3)}$, four-wave mixing process can be visualized in terms of the change of the nonlinear refractive index connected with the real part of the third order nonlinear susceptibility. Electronic transitions in terms of the so-called electronic hyperpolarizability contribute significantly to the nonlinear susceptility, so four-wave mixing at electronic transition resonance can be visualized as polarizability changes associated with the susceptibility (both the real part and the imaginary part) and yield information on the dephasing time of the transition. DFWM can be carried out in several geometries: off-axis or collinear. The special case of pairwise counter-propagating beams displays interesting properties with optical phase conjugation, which can be used for real-time processing of optical fields based on

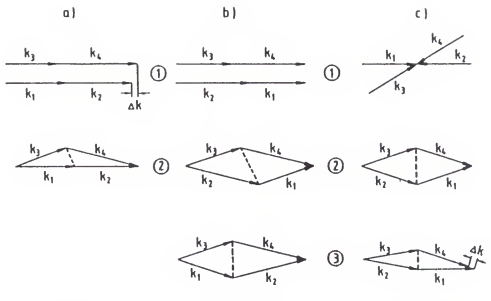

Figure 2-4 Wavevector diagrams of the mixing process $\omega_1+\omega_2-\omega_3+\omega_4$; (a) nondegenerate case with phase-matching $\Delta k=0$ adjustable in the off-axis geometry (2); (b) partially degenerate four-wave mixing with automatic phase-matching in the one-beam (1) and two-beam (2) experiments, whereas in the four-beam geometry, $\Delta k=0$ has to be adjusted; (c) fully degenerate case, DFWM, with automatic phase-matching with pairwise counterpropagating (1) or co-propagating beams (2) for arbitrary beam intersection angle. Broken lines indicate the k-vectors of several induced (non-propagating) phase and/or amplitude gratings (from ref. 10).

phase reversal of the incoming wave. A comprehensive discussion of the effect is given in the volume Optical Phase Conjugation, edited by Fisher (14).

In semiconductor research, most transient DFWM experiments are conducted at electronic resonance to study the dephasing time and homogenous linewidth of the transition and the most commonly used geometry is called two-pulse self-diffraction geometry. In this geometry, two excitation pulses at the resonance are incident on the sample with a certain angle θ between their wavevectors. One of the pulses acts twice: first two pulses together setup a population grating resulting from the interference of the two beams, then one of the beams is diffracted from the grating through a four-wave mixing interaction. The wavevector associated with the grating is given by $2k_1\sin(\theta/2)$. If there is a relative time delay between the two pulses, then the time evolution of the population grating can be mapped out, which gives the dephasing time (T_2) of the transition through the relation $\exp(-2t/T_2)$ for a homogeneously broadened system and $\exp(-4t/T_2)$ for an inhomogeneously broadened system (15). Once the dephasing time is determined, the homogenous linewidth can be calculated from $L_{homo}=2\hbar/T_2$. The homogeneous linewidth yields information on various scattering processes and offers the possibility of determining quantitatively the various contributions. For example, the temperature dependence of the exciton homogeneous linewidth yields a phonon-exciton coupling constant. The schematics of the diffraction geometry are depicted in figure 2-5. (The case of partially degenerate FWM where a third pulse at a different frequency serves as a probe pulse and interacts with the grating

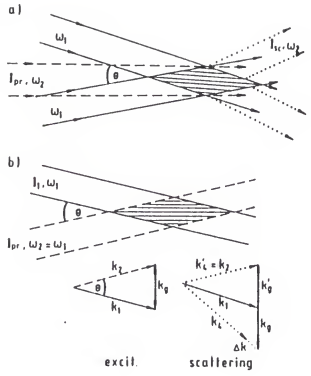

Figure 2-5 Schematic of the beam geometry for light scattering from induced population gratings; (a) three input beams for partially or fully degenerate pulse frequencies ($\omega_1 \neq \omega_2$ or $\omega_1 = \omega_2$); (b) two input beams in the fully degenerate case; k-vector diagrams for the excitation and probing processes are also shown; scattering components occur both in new directions (e.g. wave-vector k_4; mismatch Δk) and parallel to the input beams (e.g. k_4' with $\Delta k = 0$) (from ref. 10).

induced by the other two pulses is also shown, although it is less commonly used.) The advantage of this geometry is that the input and output beams can be easily separated from one another based on their directions. The disadvantage comes from the fact that the interaction is not phase-matched because the two beams have an off-axis geometry, so small angles θ and short samples are required to achieve sufficiently small values of Δkl for phase matching. The theoretical insight of the grating diffraction process through a population induced grating based on a two-level system is given by Yariv (16). The experimental setup of transient DFWM is shown in figure 2-6. Two synchronized pump pulses of equal frequencies excite the sample via resonant absorption. One of the pulses is delayed through an optical delay line relative to the other. The diffracted signals, up to several orders in the forward direction, are collected by a photodetector to monitor the intensity. The time delay can be varied so the temporal profile of the diffracted signal can be obtained to yield the dephasing time. Since the diffracted signals to be monitored are in the forward direction, this technique is called transmission DFWM. However, many semiconductor films and nanostructures are grown on opaque substrate, which means that the diffracted signal in the forward direction will be reabsorbed by the substrate, so the transmission DFWM is no longer suitable. Removing the substrate by chemical etching or other methods can be a solution; however, structural degradation such as internal mechanical stress or a rough surface may result and provide a high background level of scattered light in the experiment. To overcome these difficulties, reflection DFWM is used. In the reflection configuration, the

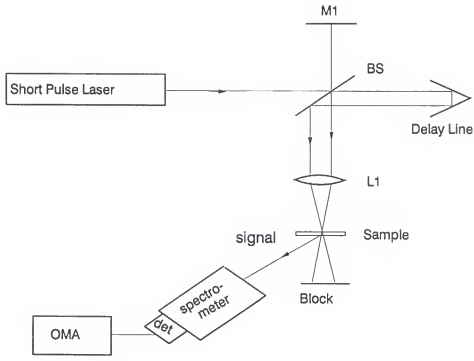

Figure 2-6 Schematic diagram of degenerate four-wave mixing experimental setup. BS-Beam-Splitter, L: Lense, M: Mirror, OMA: Optical Multichannel analyzer.

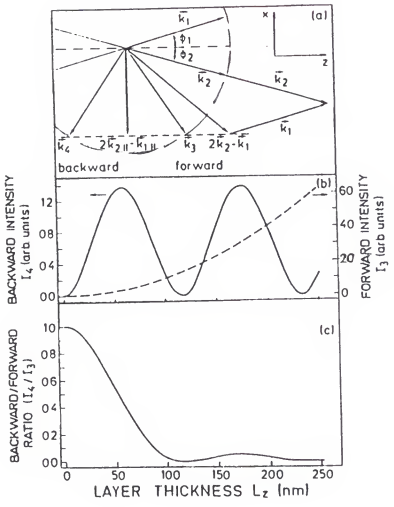

Figure 2-7 Geometry of the exciting beams and the generated signals. (b) Calculated intensities in forward (dashed line) and backward direction (solid line), and (c) the ratio between intensities in forward and backward direction as a function of layer thickness L_z. The calculation was based on excitons in a layer with infinitely high barriers (17).

diffracted signal in the backward direction is monitored. The forward and backward signals from population grating diffraction differ in the amount of phase matching, so the backward intensity is strongly modulated with the interaction length and its maximum saturates at small values. However, in thin layers, where the interaction length is very short, the backward intensity should be stronger. Honold et al. (17) investigated both theoretically and experimentally the forward and backward diffracted DFWM signal at the exciton resonance in GaAs quantum wells for the two pulse self-diffraction scheme. Their result (figure 2-7) shows that for very thin layers (<50nm), the backward intensity is comparable to the forward intensity at excitonic transitions.

Three-Pulse Photon Echo

Three-pulse echo is the extension of two-pulse echo. There are three rather than two excitation pulses involved. Adding a third excitation pulse, which enters the sample at a time t_2 after the second pulse, gives new information on the material system. For a two-level process, the three-pulse technique allows determination of the energy relaxation time T_1 in the coherent experiment by varying the time delay t_2, and determination of the dephasing time T_2. When other energy levels are involved in the energy relaxation process, a third pulse at a wavelength differing from the first two excitation pulses gives information on the path of energy decay.

The solution of polarization associated with three-pulse echo consists of a number of different terms: single pulse excitation terms due to individual pulses,

two-pulse echoes originating from pairs of three excitation pulses, higher order terms, and the three pulse echo term given by (10)

$$P_{3PE}(t) \propto \int d\omega f(\omega) \exp[-i\omega(t-t_1)-(t_1+t)/T_2] G(T_1,t_2) \exp[-i(k_b-k_c-k_a)r]$$

where $G(T_1, t_2)$ depends on the level scheme involved. For the two-level scheme, G has the form of $\exp(-t_2/T_1)$, while for more than two-level systems, G takes the form of $1+\exp(-t_2/T_1)$. From this equation, a variation in t_1 yields the dephasing time T_2 and a variation of t_2 yields the energy relaxation time T_1.

To measure the dephasing time T_2, t_2 is kept constant at a selected value and t_1 is varied. The signal scattered by the third pulse is detected in either of the two directions $k_4=k_c+k_b-k_a$ or $k_5=k_c+k_a-k_b$. To measure the energy relaxation time, the first two pulses enter the sample simultaneously, i.e. $t_1=0$ and the third pulse is delayed through t_2. The scattered energy induced by the third pulse is detected as a function of t_2. Three-pulse echo can be also used to monitor population decay of an energy state in a multiple energy level system. Such an experiment is called two-color echoes. As shown in figure 2-8 (10), the first two excitation pulses 1 and 2 induce a population grating for the two levels a and b. The population of the ground state a and the excited states b are changed. The probe pulse 3 at a new wavelength connects states b and d. When the inhomogeneous broadening in the different levels is correlated, the third pulse generates an echo signal. The echo amplitude is a function of the time delay t_2 and reflects the population decay of state d.

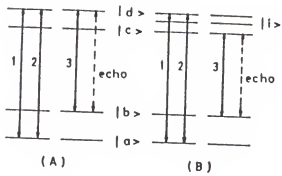

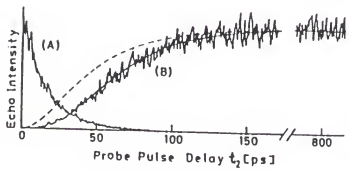

Figure 2-8 Two-color stimulated photon echos applied to the study of energy relaxation pathways. Left part: level scheme of the experiment. In case A the first two excitation pulses 1 and 2 generate the population grating in states a and d. Pulse 3 has a wavelength probing only the grating of level b and d. Varing the delay time t_2 between pulses 2 and 3 allows us to measure the decay of population state |d> (curve A). In case B the wavelength of the probing pulse is selected in order to probe states b and c. An echo found with this probing wavelength allows us to follow the population grating of states c and b built up in the course of relaxation out of state d. Curve B shows a delayed build-up of this echo suggesting the existence of level i populated during the relaxation (from ref. 10).

Incoherent Time-Resolved Spectroscopy

Incoherent time-resolved spectroscopy measures the total carrier energy relaxation time including thermalization and subsequent recombination. Carrier thermalization occurs within one picosecond, while recombination takes far more than a picosecond. There are various processes that contribute to the carrier decay such as carrier-carrier scattering, carrier-phonon interaction and carrier-impurity scattering. The total relaxation time measured is related to the individual processes by the equation: $1/\tau_{tot} = 1/\tau_1 + 1/\tau_2 + 1/\tau_3 + ...$ In most cases, only one or two relaxation processes dominate the total relaxation process under certain conditions, so a particular relaxation process may be studied with simplicity by neglecting the others. In fact, many experiments have been designed in such a way that only the process under study dominates the whole relaxation. For example, by choosing an excitation energy near the bandgap (.i.e, low excess carrier energy), carrier-carrier scattering and many-body effect are dominant during carrier thermalization and other processes such as carrier-phonon interaction are negligible. Once individual processes are qualitatively understood, interactions among these processes in more complicated situations can be studied with greater ease.

There are two major categories of time-resolved incoherent spectroscopy techniques: time-resolved photoluminescence and transient absorption (or reflectance). Both are widely used in carrier dynamics studies in semiconductors. Luminescence and absorption measurements provide complementary information about carrier relaxation. Absorption measurements measure a quantity related to

the sum of the electron and hole occupation functions, while the luminescence experiments measure their products. From the sum and product information, both electron and hole occupation functions can be determined.

Transient Differential Absorption (or Reflectance)

The Pauli exclusion principle states that full occupation of electron or hole states will block further absorption at the corresponding photon energies. The principle yields $\alpha=\alpha_0(1-f_e-f_h)$, where α_0 is the initial absorption, f_e is the electron distribution, and f_h is the hole distribution. Therefore, in principle, one has to measure the absorption spectrum α_0 of the sample without excitation and the absorption spectrum α in the presence of injected carriers. Then, the absorption ratio will give a measure of the sum of the occupation functions. By measuring the absorption spectrum over a wide range of energies using a white light continuum ultrashort pulse as a probe after photoexcitation by an ultrashort pump pulse, the time dependence of the occupation functions which is a measure of the carrier thermalization process can be obtained. This is the simplest picture of the absorption process. Understanding the departure from this picture on a very short time scale is essential. Transient absorption can be done at either near bandgap excitation (low carrier excess energy) or far above the bandgap (high carrier excess energy). For near bandgap excitation, carrier-carrier scattering (electron-electron, electron-hole, hole-hole) can be isolated as the primary thermalization mechanism, since other mechanisms such as intervalley scattering and carrier-phonon scattering are not probable with low carrier excess energies. In the case of

excitation far above the bandgap, many competing thermalization processes participate (intervalley scattering, LO phonon emission) and the situation is very complex. Most experimental work has been concentrating on near-bandgap transient absorption. Even though the picture is simple, there is still much to learn about the carrier thermalization such as the separate contributions of electron-hole, electron-electron, and hole-hole scattering.

Figure 2-9 shows a typical transient absorption measurement apparatus (2). The white light pulses are split into two beams by a beam splitter, with the higher intensity as the excitation pump pulse and the weaker one as the probe pulse. An interference filter is used to select the excitation energy from the white light continuum. The probe beam is delayed relative to the pump by going through a time delay controller. Both the pump and probe beams are focused through the sample at the same spot. The probe beam enters the spectrometer and is detected with an optical multichannel analyzer. The transmitted probe pulse spectrum is scanned while the pump beam is chopped on and off with a synchronized shutter, thus forming the differential transmission spectrum as a function of the time delay between the pump and probe beams. Generally the pump and probe beams are cross polarized to minimize the coherence effect, and also the pump beam is focused to larger size than the probe beam through the sample to ensure probing the excited volume. A detailed discussion of transient differential absorption can be found in reference 18.

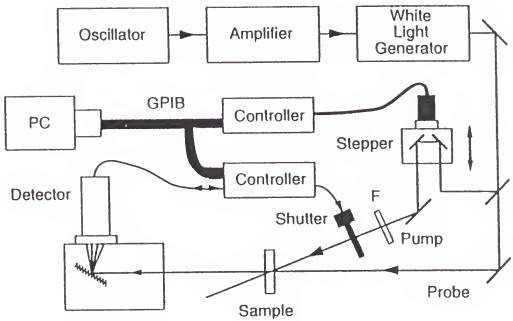

Figure 2-9 Experimental apparatus for transient absorption measurement (from ref. 2).

For transient differential reflectance, the basic principle is the same except that the reflection spectrum is probed as a function of time delay. Reflectance can be considered as complementary to the absorption (R+A+T=1), so the differential reflectance experiment roughly gives the same kind of information as the differential absorption. However, the absorption experiment is more frequently used due to its experimental simplicity. For details on transient reflectance, see chapter 29 in reference 20.

Time-Resolved Photoluminescence

Time-resolved photoluminescence measurements give information on carrier recombination dynamics. Since recombination is the subsequent process following carrier thermalization, it also gives indirect information on carrier thermalization processes through recombination information (4,19). There have been many time-resolved photoluminescence techniques developed so far, and each of them has limitations and advantages. A number of them are discussed below.

The optical Kerr gate (20)

The optical Kerr gate consists basically of a Kerr active liquid (i.e., CS_2) situated between two polarizers. Under intense electric field associated with the laser pulse (10^5V/cm), the molecules of the Kerr active liquid experience an induced birefringence. The light passing through the liquid becomes elliptically polarized and passes partially through the second polarizer. Light can only pass through the gate while it coincides with the intense laser pulse that opens the gate. Thus a short

and intense laser pulse can be used to map out successive portions of the temporal profile of the emitted luminescence as shown in figure 2-10a.

A schematic of the experimental setup is shown in figure 2-10b. An ultrashort pulse is divided by a beamsplitter into a gate pulse and a pump pulse. When a solid-state laser like Nd:glass is used, the gate pulse is the fundamental (1060nm) and the second harmonic (530nm) is the pump pulse used to excite the sample. The gate pulse travels a variable optical path and enters the Kerr cell at 45^0 with respect to the polarizers. The luminescence then passes through the Kerr gate. The two cross-polarizers normally block out the luminescence. When the gate pulse is present, the portion of the luminescence that coincides with it in time passes through the Kerr gate and is measured by a photomultiplier detector. The temporal profile of the luminescence can be measured by changing the delay of the gate pulse with respect to the pump pulse.

The resolution of the optical Kerr gate depends on the duration of the gate pulse and the reorientation time of the molecules of the active medium. For CS_2, one of the fastest Kerr-active media available, the reorientation time is about 2 picosecond (21). With the advent of ultrashort pulse lasers (femtosecond duration), the only limitation of optical Kerr gate is the reorientation time of the Kerr media which is in the picosecond range. Details on the Kerr gate can be found in reference 22.

The parametric upconversion gate (20)

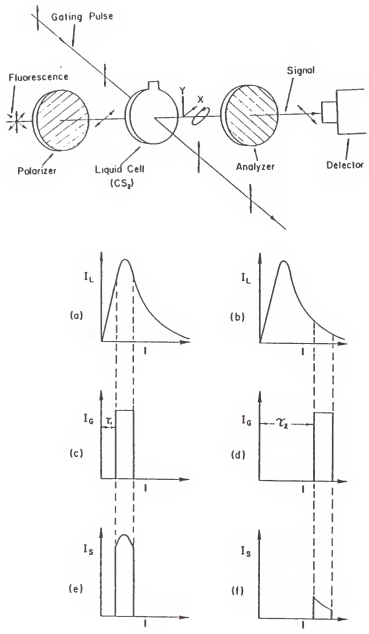

Figure 2-10a Schematic diagram and principle of an optical Kerr gate. The gating pulse is polarized at 45° with respect to the two polarizers. Two segments of luminescence carved out by gating pulse at two different delays are shown. By varying the delay time the luminescence profile can be reconstructed (from ref. 20).

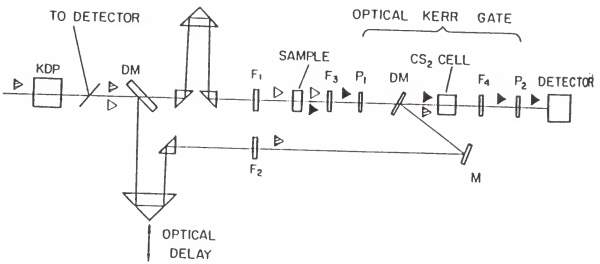

Figure 2-10b Experimental setup for luminescence measurements using an optical Kerr gate. P_1 and P_2 are the two cross-polarizers; F_1, F_2, and F_3 are cutoff filters. A infrared source is used as the gating pulse and its second harmonic is used to excite the sample. A dielectric mirror (DM) separates the two beams. The two beams are delayed relative to each other. The luminescence is collected after the gate, and only the portion of luminescence that coincides with infrared pulse will pass through the gate and get collected (from ref. 20).

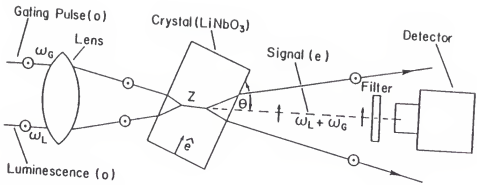

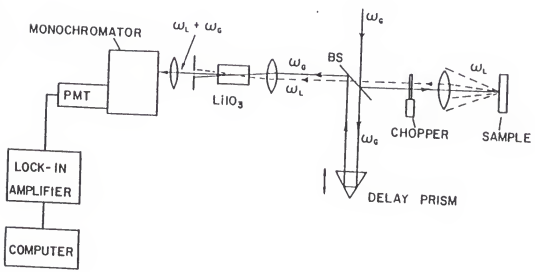

Figure 2-11 Schematic diagram and experimental setup of the parametric upconversion gate. The gating and luminescence pulses are combined inside the crystal to produce a sum frequency wave and this sum frequency beam is selected and measured. BS is the beamsplitter, ω_G is the laser beam, and ω_L is the luminescence signal (from ref. 20).

In this technique, the luminescence from the sample is collected, collimated, and combined with a part of the excitation pulse in a noncentrosymmetric crystal (such as ATP, $LiIO_3$, or KDP), as shown in figure 2-11. The angle of the crystal is set to phase-match the frequency of the gating pulse with a selected frequency of the luminescence. A signal whose frequency is the sum of the laser and the luminescence frequencies is generated in the crystal and detected by a photomultiplier. Figure 2-11 also shows the experimental arrangement for luminescence time-resolved spectroscopy using an upconversion gate. The laser beam is divided by a beamsplitter. One of the beams is directed to the delay line, and the other is modulated by a mechanical chopper and excites the sample. The luminescence from the sample is collected and combined with the original laser beam from the delay line inside the crystal. When the crystal is tuned to satisfy the matching condition, the sum frequency wave is generated. The signal frequency is separated by a monochromator and detected by a photomultiplier. The lock-in amplifier discriminates whatever background remains. Varying the delay of the gate pulse, the temporal profile of the luminescence can be obtained. To obtain the spectra at a given time delay, the wavelength of the laser is usually continuously tuned to allow the phase-matched sum of the gating pulse frequency and selected luminescence frequency to remain the same. Therefore, the upconversion gate, when used with a continuously tunable laser, can provide both the temporal and spectral profiles of the luminescence.

Because upconversion involves virtual electronic transitions, this gate has a response time equal to the pulse width of the pump laser. The efficiency of parametric conversion depends on the interaction length in the crystal and the phase-matching conditions: $k_s=k_L+k_G$, $\omega_s=\omega_L+\omega_G$. Since the nonlinear signal also strongly depends on the input light intensities, this technique is more suitable to the study of relatively strong luminescence processes.

The streak camera (20)

The technique most widely used for luminescence measurements in the picosecond range uses a streak camera. Figure 2-12 illustrates the schematics of the operation of a streak camera as well as the apparatus to measure fluorescence using a streak camera. In a streak camera, photoelectrons emitted by light striking the photocathode are deflected by an applied voltage ramp that causes the electrons to be transversely streaked across a phosphorescent screen. Photoelectrons released at different times from the photocathode strike the phosphorescent screen at different positions, causing a track with a spatial intensity profile proportional to the incident temporal intensity profile of the fluorescence. The phosphorescent track may be analyzed by photographic techniques or electronically sampled by a video system. To measure fluorescence using a streak camera, the ultrashort pulse from the laser is divided into two parts by a beamsplitter. One part of the beam is sent to a photodiode that triggers the streak, and the other excites the sample. The pump pulse has to be delayed for a few nanoseconds before the streak camera is ready. To produce that long delay, the

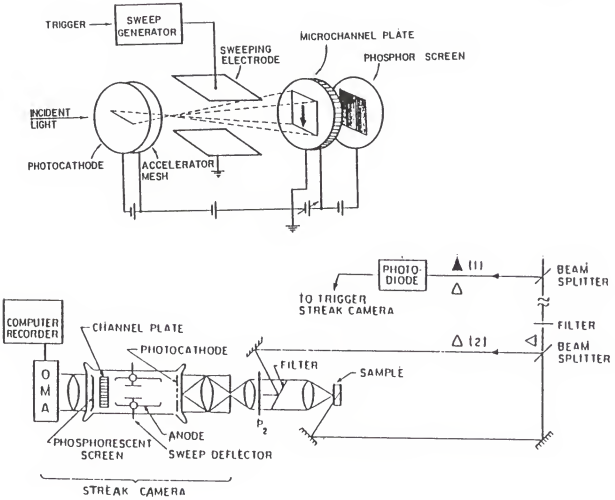

Figure 2-12 The upper diagram shows the operation of a streak tube; the lower portion shows the schematic of the apparatus used to measure fluorescence decay by a streak camera. A beam splitter provides two side beams. Beam 1 triggers the streak camera. Beam 2 arrives at streak camera at an earlier time to provide a calibration pulse. The streak produced at the phosphorescent screen is recorded by an optical multichannel analyzer (OMA) (from ref. 20).

pump pulse travels through a white cell. Before the pump strikes the sample, a wedge reflects part of the beam directly into the slit of the camera. This prepulse is used for the calibration of the zero time. The fluorescence from the sample is collected and passes through a cutoff filter to eliminate the excitation pulse and is focused onto the slit of the streak camera. A streak camera can also be coupled with a spectrograph and a two-dimensional array to provide both temporal and spectral characteristics of the luminescence (23).

The temporal resolution of the streak camera has four components: the range of the initial kinetic energies of electrons emitted from the photocathode; the width of the slit; the scanning velocity; and various edge effects such as optical diffraction and space-charge effects. The temporal resolution of the streak camera is limited to 1-2 picoseconds. Recent advances in streak cameras can be found in reference 24.

Time correlated single-photon counting (20)

The time-correlated single-photon counting method consists of repeated measurements of the time difference between the exciting pulse and the detection of a single photon due to fluorescence. The probability, thus determined, of photon detection as a function of time after the excitation gives the temporal profile of the fluorescence intensity. Owing to the rapid progress in fast electronics, the time interval between two pulses can be measured on a picosecond time scale. Moreover, the single-photon counting method is the most sensitive method for measuring fluorescence and has a large linear dynamic range. Therefore, the time-

correlated single-photon counting method is particularly suitable for the study of very fast time characteristics of weak fluorescence (25).

The heart of the system is a time-to-amplitude converter (TAC), which electronically measures the time interval between the exciting light pulse and the photon detection. The TAC initiates its time sweep when it receives a start pulse, which may be a reference pulse synchronized with the exciting light pulse. When a stop pulse, which may be the output pulse of the photomultiplier due to the detection of a single photon, is sent to TAC during the time sweep, it generates an output pulse whose amplitude is proportional to the time difference between the start and stop pulses. If the output of TAC is fed into a multichannel pulse-height analyzer (MCA), the channels correspond to the increments in time. Therefore, by repeating this timing procedure, it is possible to measure the frequency of photon detection as a function of time after excitation. To ensure that at most only one fluorescence photon is detected by the photomultiplier for every excitation pulse, the ratio of photon detection frequency to the exciting pulse frequency must be sufficiently low. Therefore, very high repetition rate exciting pulse is required in order to accumulate a large amount of data to increase the accuracy of the measurement.

The schematic of a fluorescence-lifetime measuring system using single-photon counting is depicted in figure 2-13 (26). The light source can be selected from cw mode-locked Ar+ and Kr+ lasers (150ps pulsewidth), synchronously pumped cw mode-locked dye lasers (10ps duration), and the second harmonics of

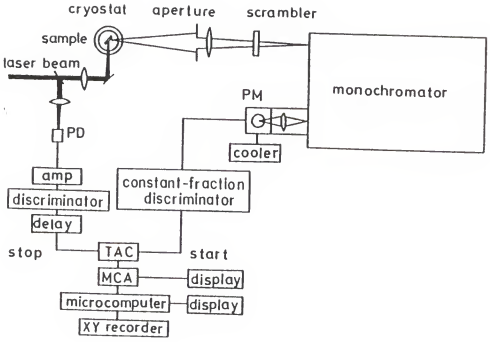

Figure 2-13 Block diagram of a fluorescence-lifetime measuring system using the time-correlated single-photon counting method. TAC: time-to-amplitude converter; MCA: multichannel pulse-height analyzer (from ref. 20).

these lasers. First, the short light pulses from these sources are divided into two by a beamsplitter; one is used for excitation of the sample, and the other as a reference. Fluorescence from the sample is analyzed by a monochromator and detected by a photomultiplier as a single-photon event. Then the output pulse of the photomultiplier is discriminated by a constant-fraction differential discriminator and fed into a TAC as a start pulse. The discriminator is needed to reject noise pulses and also to shape proper signal pulses. The other part of the laser beam is detected by a p-i-n photodiode, whose output is amplified, discriminated, delayed and then used as a stop pulse of the TAC. Because the TAC converts the time interval between the start and stop pulses into pulse amplitude, the pulse-height distribution of the output of the TAC gives the time profile of the photon detection probability by the photomultiplier. This pulse height is analyzed and accumulated into a MCA, and the obtained data are then analyzed by means of a computer.

The resolution of this technique is limited by the response of the electronics besides the pulse duration of the laser. The currently achievable resolution is in the picosecond range.

Nonlinear Luminescence Techniques

A number of luminescence techniques based on the nonlinearity of the luminescence of the sample have been developed as simple and inexpensive techniques with resolution only limited by the pulse duration of the laser used. The nonlinearity may stem from a bimolecular recombination of photogenerated carriers, as in the population mixing technique (27), or from saturation of the luminescence

in organic dyes (28, 29). These nonlinear techniques indirectly give the lifetime of the luminescence from the correlation curve.

In the population mixing technique (figure 2-14), a continuous wave (cw) pulse train is divided equally by a beam splitter. One pulse train is given a variable time delay. The pulse trains are modulated at different frequencies, ω_1 and ω_2 by two mechanical choppers, and focused on a semiconductor sample. The intensity of the luminescence is detected by a photomultiplier and measured by a lock-in amplifier tuned to the difference (or sum) of the modulation frequencies. The luminescence lifetime can be extracted from the correlation curve measured. The details of this technique will be discussed in chapter 5.

In a similar technique developed by Mahr and Sagan (28) and Olsson et. al. (30), two lock-in amplifiers are used in series. The lock-in amplifiers are tuned to ω_1 and ω_2 respectively. The two frequencies are multiples of each other. The ac signal resulting from the choppers has a frequency of ω_1 modulated by ω_2 ($\omega_1 > \omega_2$). The output from the first lock-in which is tuned to ω_1 is a dc signal with a ripple at frequency ω_2. The second lock-in tuned at ω_2 removes the dc component.

In the three-pulse excitation technique (figure 2-15), three pulse trains are focused on the sample (29). One train of intense pulse pumps the sample. The other two pulse trains (probes) are equally intense, but much weaker than the pump, and are chopped 180^0 out of phase with respect to each other. One of the probes is set at a fixed delay relative to the pump. The delay of the second probe

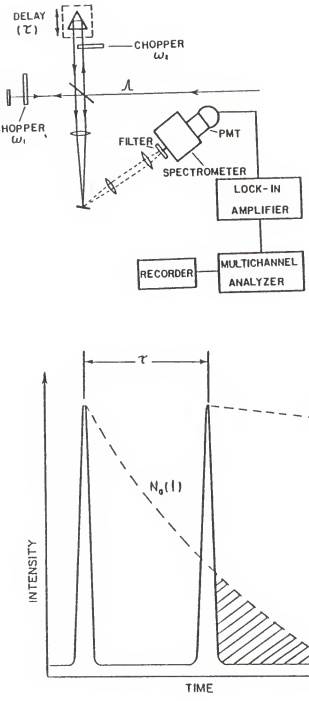

Figure 2-14 The upper diagram shows the schematic of luminescence measurements by population mixing. One pulse train is equally divided into two. One of them is delayed by a movable prism with respect to the other. The lower diagram illustrates the principle of this technique showing how electrons generated by the first pulse mix and recombine with holes generated by the second pulse (from ref. 20).

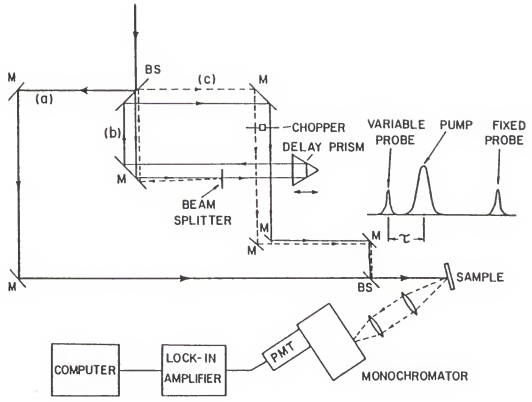

Figure 2-15 Schematic arrangement of the three-pulse excitation. See text. (from ref. 20)

can be varied. The luminescence is detected by a photomultiplier and measured by a lock-in amplifier.

The advantage of these nonlinear luminescence techniques is the simplicity in experimental setup with time resolution only limited by the pulse width of the laser source.

Selection Criteria of Suitable Techniques

Selecting the right experimental technique to study carrier dynamics processes in semiconductors is extremely important to the understanding of the carrier dynamics physics which relies on the accuracy of the data. Generally, more than one technique is used to study a material system. The selection criteria of suitable time-resolved techniques depend on many factors. Some of the important ones are outlined below.

Characteristics of the Material System

Characteristics of a particular material system include the microscopic electronic energy band structure and the bulk structure. The electronic energy band structure determines the characteristic time scales of carrier relaxation processes and the oscillator strength of transitions. The time-resolved techniques chosen must have the time resolution and sensitivity required to resolve these processes. For example, if we are interested in a recombination process occurring in the femtosecond time-scale, picosecond luminescence techniques such as streak camera, optical Kerr gate, and time-correlated single-photon counting are not suitable any more, instead, parametric up-conversion and nonlinear techniques

which can have subpicosecond resolution (depending on the pulsewidth of the laser) are more appropriate. If the recombination process is very weak, then nonlinear techniques should be used since parametric up-conversion requires a relatively strong signal. The bulk structure determines if transmission or reflectance configuration can be used. If the film under study is grown on an opaque substrate, then only reflection configuration techniques can be chosen, such as reflectance four-wave mixing, transient differential reflectance and all luminescence techniques.

Processes Under Study

Processes under study determine which technique to choose. If only coherent processes are of interest, then coherent techniques such as four-wave mixing, three-pulse echo, and coherent Raman should be used. If only incoherent processes are of interest, then transient absorption and luminescence techniques can be selected. Transient differential absorption is more suitable for the study of carrier thermalization, while luminescence techniques are more suitable for the study of recombination processes, although there are overlaps between them. Four-wave mixing studies the coherent dephasing process of electronic transitions, while coherent Raman studies the coherent dephasing process of molecular transitions (phonons).

Experimental Complexity and Availability of Resources

Experimental complexity and availability of resources have to be considered when choosing time-resolved techniques. Experimental complexity challenges the accuracy of data acquisition and requires additional apparatus. The ideal goal is to

have experiments as simple as possible while still be able to obtain the information sought. However, in many circumstances, dynamics of complicated processes have to be obtained from complex experiments and a compromise has to be made in simplicity.

CHAPTER 3
REVIEW ON PAST PROGRESS ON SEMICONDUCTOR CARRIER DYNAMICS STUDY

The field of ultrafast carrier dynamics is new and rapidly developing. Since the advent of ultrashort pulse lasers operating over a broad range of wavelengths, significant progress has been made in understanding carrier relaxation processes in semiconductors by using ultrafast optical spectroscopy. The emergence of novel devices such as resonant hot-electron transistors and quantum interference switches which utilize hot-electron effects such as ballistic transport and transient velocity overshoot has generated much excitement in this field. This chapter reviews some of the progress in common semiconductors: group IV (Si), group III-V (GaAs), and group II-VI (ZnSe).

Bulk Semiconductors And Films

Here bulk semiconductors refer to semiconductor single crystals, while films refer to epitaxial films (normally less than several microns thick) grown on a substrate by a variety of deposition techniques. With the push for higher frequency response devices, more films have replaced bulk crystals in submicron electronic devices. However, research always starts from the bulk because bulk crystal properties provide the basic information necessary for investigating complicated structures of the same material. In fact, all epitaxial film growth techniques are developed after the bulk properties have been understood.

Silicon

Silicon is the most studied semiconductor since it is the mainstay of the semiconductor industry. Carrier dynamics studies on Si have been hindered by its indirect bandgap characteristic and many common optical pump and probe techniques are not very useful. However, a number of novel optical probe techniques have been recently developed to study indirect gap materials like Si and Ge in particular. Tanaka et. al. (31, 32) studied subpicosecond hot carrier relaxation in Ge by time-resolved intervalence band Raman scattering (also known as hot luminescence). They found a hole intervalence band scattering time of 700fs and an electron intervalley scattering time of 1.2ps at a photoexcited carrier density of $10^{17}/cm^3$.

Son et al. (33) studied picosecond dynamics of transient velocity overshoot in Si using a terahertz (THz) radiation technique. In their experiment, a reverse-biased lateral p-i-n structure was used to provide a uniform electric field in the undoped region of a Si wafer. The "i" region was photoexcited with 80fs optical pulses from a Ti:sapphire laser to generate carriers in the lowest conduction band. The dynamics of the photogenerated carriers were then measured using photoconductive detection of the terahertz radiation which emanated from the Si (34). The THz radiation in the far field is proportional to the time derivative of the photocurrent. This broad-band radiation was measured over a wide range of electric fields up to 80kV/cm. They found that the transient velocity overshoot in Si increases as the electric field increases up to 50kV/cm, then saturates. This is

different from the GaAs case which shows a maximum degree of overshoot around 40-50kV/cm and a decrease of overshoot at higher fields (35).

Goldman et al. (36) investigated femtosecond dynamics of electron distribution in Si. Their investigation was accomplished in a pump-probe format by measuring the photoelectron spectrum generated by an ultrashort UV probe pulse. The UHV clean Si sample was excited using 2eV photon energy, 150fs laser pulses to a hot carrier density of $10^{19}/cm^3$. Excited electron distributions were photoemitted using an ultrashort 4eV probe. They found that excited electrons follow a thermal distribution by 120fs, which gives an upper bound on the electron-electron scattering time of <120fs. By 180fs, the distribution cools down very fast due to electron-phonon scattering. Beyond 200fs, the distribution cools down much more slowly and finally reaches equilibrium with the lattice at 1ps. The slower cooling rate at longer delays is consistent with the scattering rate decreasing as electrons move toward lower energies.

Rappen et al.(37) investigated the dephasing of the continuum states at the direct gap of doped and undoped Ge and its dependence on polarization of the two beams by employing femtosecond degenerate four-wave mixing in the self-diffraction geometry. They found that the dephasing time is longer for the n-doped samples (600fs) than that for undoped ones (320fs). They attributed the observation to the final states in the L valley and hence a reduced scattering rate from Γ to L. They also found that the measured decay time on the n-doped samples is longer for the cross-linear configuration (840fs) than for the collinear configuration (600fs),

which is contrary to recent observations and model calculations based on disorder-induced coupling of spin states in quantum well samples (38). More detailed investigations are under progress.

Gallium Arsenide

Compared to Si, GaAs has a direct bandgap (1.42eV at 300K) and higher electron mobility which make it a better candidate for fabricating fast response devices. Most high speed electronic and photonic devices are fabricated from GaAs based structures. For example, ballistic transport devices are based on 2DEG (2-dimensional electron gas) accumulated in a GaAs/AlGaAs heterojunction. In 2DEG, parent donors and acceptors are separated physically from the electron gas to minimize electron-impurity scattering so ballistic transport over extremely long distances can take place. Resonant tunneling hot electron transistors (RHET) consist of InAlAs as emitter and base and InAlGaAs as the collector. The resonant-tunneling barrier between the emitter and the base consists of a very thin layer of InGaAs. The very short carrier transient time in RHETs due to the resonant tunneling effect allows the possibility of high-speed operation. Most carrier dynamics studies have focused on GaAs based structures (39) not only because of the demand for high frequency devices but also because of interest in fundamental science. As a consequence, hot carrier relaxation processes are most understood in GaAs compared to other semiconductors.

Gupta et al. (40) studied ultrashort carrier lifetimes in GaAs based III-V films grown by molecular beam epitaxy at a range of low substrate temperatures by time-

resolved optical absorption, reflection and photoconductive switching measurements. They found a distinct decrease in carrier lifetime with decreasing growth temperature (subpicosecond lifetime for GaAs grown at 200°C). As evidenced by transmission electron microscopy, molecular-beam-epitaxial growth of As based III-V compounds at very low substrate temperatures leads to an excess As incorporation in the epilayers in the form of interstitials, antisites, and microclusters, which in turns leads to the generation of a large density of deep-level defects. Therefore, the carrier lifetime is dramatically reduced due to trapping and subsequent recombination at these centers. In addition to very short carrier lifetimes, these materials also exhibit very high resistivity and good carrier mobilities. Thus these materials have desirable properties for ultrafast optoelectronic applications such as sampling gates, photodectors, and picosecond switching.

Kash et al. (41) studied LO phonon dynamics in GaAs by time-resolved Raman spectroscopy. In their experiment, compressed laser pulses were divided into a pump pulse and a weak (10-20%), orthogonally polarized, delayed probe pulse, which were combined at the sample. Because the pump and probe were perpendicular in polarization, the LO phonon Raman scattering emissions excited by the pump and probe were also orthogonal. Thus, only the Raman scattering from the probe can be detected by using a polarizer filter with probe beam polarization blocking out the pump induced signal. In the presence of injected carrier density less than $10^{17}/cm^3$, they temporally resolved the growth of the optically induced non-

equilibrium LO phonon population and deduced an average electron-phonon scattering time of about 165fs. For higher injected carrier densities, they observed substantial time-dependent changes in the Raman spectra which result from screening of the LO phonons by the free carriers and the relaxation of free carriers to the band edges.

Kash (42) also investigated carrier-carrier scattering in GaAs:Mg through measurements of hot electron neutral acceptor luminescence. The rate at which a single nonequilibrium electron in GaAs loses energy to an optically injected, thermalized electron-hole plasma was measured by comparing the emission from nonequilibrium electrons recombining at neutral acceptors in the presence and absence of the plasma. The intensity of luminescence decreases in the presence of the plasma due to carrier-carrier scattering. The decrease directly gives the scattering rate, which is linear with injected density. At a density about $n=p=8x10^{16}cm^{-3}$, the loss rate of a 0.3-eV electron to the plasma was found to be the same as the polar scattering rate. Both single-particle scattering and collective excitations of the plasma were shown to be important. In this experiment, electrons are excited into the conduction band with low excess energy, so other scattering mechanisms are not important.

Zhou et al. studied hot-phonon effects on carrier cooling in GaAs. In order to separate the hot-phonon effects from other effects such as carrier screening of Frohlich interaction and Landau damping which also cause a reduction in carrier cooling rate in polar semiconductors at high carrier densities ($>10^{18}cm^{-3}$), they

designed a novel experiment to study exclusively the role of hot phonons in carrier cooling. In their experiment, a GaAs sample grown at a low substrate temperature (200^{0}C) by molecular beam epitaxy was studied in a two-pulse experiment by time-resolved photoluminescence in the femtosecond regime. The low temperature grown (LT) GaAs has the same band structure and a similar radiative recombination coefficient as normal GaAs (44). However, LT-GaAs has an extremely short carrier life-time of about 1 ps, which is smaller than the LO phonon lifetime of several picoseconds. Therefore, a few picoseconds after excitation with a strong pre-pump pulse the mobile carriers will have essentially disappeared, while a substantial population of non-thermal phonons remains. The sample then is excited with a second, much weaker pump pulse, creating a substantially lower carrier density so that many-body screening effects don't influence the carrier-phonon interaction. Consequently, the influence of hot phonons on carrier cooling can be directly studied by a variation of the temporal separation of the two pulses and by changing their intensity. Compared to Raman experiments, this experiment is sensitive to optical phonons with a wide range of wave vectors. The excitation source is an 80fs, 82MHz Ti:Sapphire laser and the energy was chosen to be 1.72eV, well below the threshold energy for electronic intervalley transfer. Time and energy-resolved luminescence spectra were obtained using femtosecond up-conversion spectroscopy. Zhou found that the influence of hot phonons starts 500fs after the excitation, consistent with previous work (45). An ensembled Monte Carlo (EMC)

simulation was performed to complement the experiment and shows good agreement with the data.

Elsaesser et al. (4) studied the relaxation of a nonequilibrium distribution of electrons and holes in GaAs following femtosecond photoexcitation via spectrally and temporally resolved luminescence. A rapid onset of luminescence over a broad range shows that both electrons and holes are redistributed over a wide energy range within 100fs, even at excitation densities as low as $10^{17}cm^{-3}$. The data demonstrate carrier-carrier scattering rates higher than predicted by calculations with a statically screened interaction potential. Monte Carlo simulations using dynamical screening agree with the experimental results. The experiment was based on femtosecond luminescence upconversion. The excitation energy of 1.93eV is high above the bandgap. The absence of any structure with optical phonon spacing in the spectrum shows that inelastic carrier-carrier scattering is the main mechanism of thermalization, and is much faster than the LO phonon emission time (about 150fs).

Rodrigues et al. (19) investigated the ultrafast relaxation of minority electrons in highly doped p-type GaAs ($p=1.0 \times 10^{19}cm^{-3}$) through femtosecond time-resolved upconversion luminescence. Using low excitation densities and excitation energies well below the satellite valleys, the cooling of minority electrons under conditions where intervalley scattering and hot phonon effects are not important determines the electron-hole scattering rates. The electron cooling in the time-resolved luminescence experiments directly reveals the scattering rates between a dilute hot-

electron distribution and a dense cold majority hole plasma. For low excitation densities the hole plasma temperature stays at 300K and the transient luminescence spectra reveal the rapid cooling of minority electrons within the first few picoseconds. The electron-hole energy transfer rate is much larger (up to 10^{-7} W) than the known electron-LO phonon scattering rate, which allows a quantitative determination of the electron-hole energy transfer.

Hohenester et al. (5) investigated both experimentally and theoretically the thermalization and relaxation of optically excited electrons and holes in intrinsic and p-type GaAs and InP. Using 50-fs and 2eV laser excitation pulses the hot carrier dynamics were studied by transient absorption changes at 2eV and by time-resolved luminescence spectroscopy, with a time resolution of 50-80 fs. The materials and doping levels were chosen to obtain detailed information on intervalley and interband transfers of electrons and holes and on the effects of nonequilibrium optical phonons, of ionizing carrier-neutral acceptor scatterings, and of dynamical screening of the various carrier-carrier interactions.

For the 2eV photon excitation, the optical responses of the two materials differ mainly in the role of electronic intervalley scattering. In GaAs, this intervalley scattering is more pronounced, because the majority of photogenerated electrons in the central Γ valley of the conduction band are excited to energies larger than the threshold for transfer to secondary conduction band valleys, while in InP all photogenerated electrons are excited to energies below this threshold. By comparing the otherwise similar optical response behavior in the two materials,

qualitative information on the role of valley transfer could be obtained. A wide range of excitation and doping densities was used to separate the relative contributions of various processes. The results show that plasma cooling in InP is strongly retarded by hot-LO-phonon effects while in GaAs it is retarded also by the return of initial Γ→L transferred electrons into the L valley. Also the e→h energy transfer becomes more important with increasing hole concentration. Very good agreement between theory and experiment was found for times beyond 500fs for the effective plasma-temperatures T_{eff} defined from the measured luminescence spectra. For shorter times, the calculated T_{eff} was systematically too high. This deviation was tentatively ascribed to effects of collisional broadening and band nonparabolicities.

Zinc selenide

ZnSe is a II-VI semiconductor compound. Like GaAs, it has a direct bandgap (2.67eV @300K). Because its wider bandgap shifts its interband transition to the blue region, ZnSe has been a potential candidate for fabricating short wavelength light emitting diodes or lasers (46,47). ZnSe is also a suitable material for optical modulators and switches for use in optical signal processing and optical computing (48). However, the development of ZnSe-based devices has long been hindered by the quality of the material. Current injection and photo-pumped laser devices based on ZnSe have been demonstrated recently by improvements in epitaxial growth techniques and, in particular, by the achievement of high p-type doping (49, 50, 51, 52). At present, material quality is still the limiting factor in device performance. ZnSe and ZnSe quantum well based lasers only last 30 seconds at room

temperature and the quantum efficiency is very low (53). The low quantum efficiency is probably due to the presence of deep level defects such as Hall-Shockley-Read dislocations which serve as non-radiative recombination centers and traps (54). These centers are not detected by the conventional methods used to assess the quality of ZnSe, such as the ratio of near-band-edge emission to deep-level emission or the properties of exciton related and donor-acceptor emission at low temperature. Efficient non-radiative recombination results in a short luminescence decay time and measurements on carrier decay time will yield information on the quality of the material. Carrier lifetime also determines the laser threshold condition and the speed or frequency of device operation. Because of all these practical importance, carrier dynamics study on ZnSe has received much more attention recently. Also, the fundamental physics of carrier relaxations in ZnSe have generated much research interest as in the case of GaAs. Some of the recent progress is discussed below.

Milward et al. (55) measured the photogenerated free carrier recombination time in polycrystalline bulk ZnSe to be in the range of 7-14 ns at room temperature. They used an excite and probe technique with near-band-edge nanosecond laser pulses to measure the decay of induced free-carrier absorption, which gives the recombination lifetime. They estimated the free-carrier-pair absorption cross section to be in the range of (3-6) x $10^{-17}cm^2$. In their experiment, a strong excite beam and a weak probe beam were focused on the sample with a time delay controlled by moving a retroreflector. The two beams are collinear and cross polarized to

minimize coherence effects induced by four-wave mixing. Free carrier absorption causes a decrease in the probe transmission. The transmitted probe energy was measured for each value of the delay time.

Bolger et al. (56) studied carrier recombination processes in epitaxial MBE grown ZnSe thin films (both n-type and p-type) using a transient grating technique. In their experiment, the films are optically excited with midgap photon energies. The dynamics of the refractive-index grating established by spatially modulated carrier generation due to two-photon absorption is probed. At midgap photon energies the refractive index change associated with the carriers is strictly proportional to their density, so the diffracted signal is a direct measure of the carrier concentration. Using a conventional four-wave-mixing configuration, carrier gratings were generated by the interference of the forward and probe pulses. For photoexcitation levels in the 10^{17}-$10^{18}cm^{-3}$ range the dominant recombination mechanism was found to be radiative, described by a rate coefficient of 8×10^{-9} cm^3s^{-1}. For densities exceeding approximately 2×10^{18} cm^{-3} ultrafast grating recovery was observed, accompanied by line narrowing of the near-band-edge blue photoluminescence, which was interpreted as due to stimulated radiative recombinations. Also the p-type samples (Nitrogen plasma doped) were found to decay much faster than n-type samples (Iodine doped), and the possible reason was attributed to carrier trapping at selenium vacancies or nitrogen-selenium vacancy complexes (57).

Zheng et al. (58) measured the decay time of the blue luminescence at room temperature in n-type ZnSe grown by metalorganic chemical vapor deposition using

streak camera detection. Over an uncompensated donor concentration range of 10^{17}-$10^{18}cm^{-3}$, they found that the decay time is of the order of 100 ps. The short time was attributed to strong nonradiative recombinations at high concentration of Hall-Shockley-Reed deep level centers. The dominant transitions giving the luminescence radiation were attributed to that between an electron on a shallow donor and a free hole and that between band to band. The radiative lifetime was calculated theoretically using the Dumke (59) model for donor to hole transition and Van Roosbroeck and Shockley method for band to band transition. The non-radiative Hall-Shockley-Reed recombination lifetime was also calculated and yields a deep level concentration in the order of $10^{17}cm^{-3}$.

Massa et al. (60) studied carrier recombinations at room temperature in n- and p-type ZnSe grown by MBE. The experiment was based on photo-counting time-resolved photoluminescence over several decades of excess carrier density from ZnSe with various levels of n- and p-doping. A band-edge photoluminescence decay time of 240 ps was measured for heavily doped n-type material together with a relaxation time of a few microseconds for the associated deep-level emission. It was concluded that carrier recombination in this material was dominated by minority carrier trapping by deep-level acceptors, followed by a radiative donor-acceptor recombination. The band-edge luminescence decay time for p-type material was less than 11 ps and was attributed to a high level of nonradiative Shockley-Reed centers possibly as a result of self-compensation process in p-type ZnSe. Detailed theoretical estimates support the data.

Charbonneau et al. (61) investigated radiative recombination in highly excited high purity ZnSe single crystal at 1.8K by a single-photon counting technique. At high power densities, two new luminescence bands at 2800 meV and 2798.5 meV were observed. These peaks were attributed to the biexciton recombination line and to the biexciton-biexciton collision line by analyzing spectral positions of these emission bands, combined with their transient decay time behavior.

Steiner et al. (62) investigated photoluminescence lifetimes of bound excitons in bulk ZnSe at 1.8K by the single-photon counting method. The trend in bound exciton decay time .vs. exciton localization energy was found to follow that expected from RG (63) and SC (64) theories for purely radiative lifetimes indicating that the Auger process was not an important decay mechanism of bound excitons in ZnSe. A series of time-resolved spectra revealed short lived donor bound excitons and longer lived, perturbed acceptor bound excitons.

Semiconductor Quantum Size Structures

Semiconductor quantum size structures are semiconductor structures with dimensions in the order of or less than the Bohr diameter and with electronic properties controlled by quantum confinement effects. Quantum size structures have attracted a great deal of research attention in recent years. Compared to their bulk counterparts, quantum size structures have many unique properties due to carrier localization, such as higher excitonic nonlinearity and bandgap tailoring by varying the dimension of the structure. Structures with only one confined dimension

are called quantum wells, with two confined dimensions are called quantum wires, and with all three confined dimensions are called quantum dots. With the advances in growth techniques such as molecular beam epitaxy, very high quality quantum well structures can be fabricated with good reproducibility. However, fabrication of high quality quantum wires and dots is still under progress although fabrication of quantum wires shows promise. Quantum well structure based devices such as diode lasers, LEDs, detectors, hot-electron transistors, and resonant-tunneling diodes are now being commercially developed. These devices have demonstrated superior performance over those based on bulk materials. In the meantime, novel physics on quantum well structures is being explored to understand physical processes such as hot carrier relaxations and ballistic transport. Past progress on carrier dynamics studies of quantum wells is reviewed below.

Silicon Based Quantum Wells

Although silicon is an indirect bandgap material, it can shift to direct bandgap behavior under quantum confinement. This property makes silicon quantum wells attractive for optoelectronic applications. Silicon quantum wells carry practical significance since new devices based on them can be directly integrated into current Si circuit technology. However, the fabrication of silicon quantum wells has been a very difficult task due to the lack of closely lattice-matched suitable barrier materials. The recent emergence of MBE grown $Si/Si_{1-x}Ge_x/Si$ multiple quantum wells with Si as the barrier material and SiGe alloy as the well material shows great

promise (65,66), although their quality needs to be improved further. Not much work has been conducted on carrier dynamics due to the lack of high quality structures.

Glaser et al. (67) investigated time-resolved optically detected magnetic resonance (TR-ODMR) of luminescence from Si/SiGe superlattices grown by MBE. These structures exhibit a single, broad photoluminescence band with peak energy 100 meV below the expected bandgap. Fast and slow processes were separated with the TR-ODMR technique. The slow resonances are new and provide detailed information on the nature of the recombination. These features were tentatively assigned to Ge-rich regions in the SiGe layers based on the resonance parameters and the faster spin-lattice relaxation.

Geiler et al. (68) investigated the relaxation of excess carriers in SiGe heterostructures by photothermal measurements. Charge carrier waves generated by a double modulated laser beam probe the mobility, lifetime and the radiationless relaxation channels in layered structures of semiconductor materials. The information on amplitude and phase of the response is gained by modulated reflectivity measurements of the same laser beam. This double modulation method of thermal and carrier wave analysis was applied to the investigation of the relaxation of photogenerated excess carriers in SiGe heterostructures grown by MBE. One part of these excess carriers was collected by the buried superlattice region creating a laterally spreading carrier spreading wave. Its damping was governed by the lifetime and mobility of carriers in the superlattice. Results were

presented for the determination of the dependence of the carrier and thermal wave amplitude on the Ge content in the superlattice region.

Gallium Arsenide Based Quantum Wells

Most current quantum well devices (diode lasers, transistors) are based on GaAs, partially because the fabrication process of this material is very well controlled, and partially because this material has many suitable properties for device applications. A tremendous amount of research effort has been devoted to carrier dynamics studies in GaAs-based quantum well structures and significant progress has been made.

Gobel et al. (69) conducted picosecond luminescence experiments on GaAs/AlGaAs quantum structures at low temperature using a streak camera. They observed a significant influence of carrier localization on the transition probabilities of photo-excited carriers. The spontaneous lifetime of electrons and holes within the quantum well was found to decrease with well thickness, Lz, from 1 ns for Lz=14 nm to 350 ps for Lz=5 nm because of the enhanced recombination due to localization of carriers. By monitoring the luminescence decay of the barrier material AlGaAs, carrier trapping into the QW was found to be extremely efficient and requires diffusion velocities in AlGaAs on the order of 10^6 cm/s.

Feldmann et al. (70) studied the dependence of exciton lifetimes on quantum well thickness and temperature in GaAs/AlGaAs QWs both theoretically and experimentally and demonstrated a fundamental relationship between radiative lifetime and spectral linewidth of free excitons resulting from the fact that the

coherent extension of an exciton is determined by exciton scattering and the decay time of excitons is determined by the homogenous part of the linewidth. The experiment was conducted on GaAs/AlGaAs MQWs with GaAs well thickness between 2.5nm and 15nm grown by MBE. The luminescence spectra were time-resolved by a Synchroscan streak camera with a time resolution of 20 ps. The experimental data on decay time dependence on well thickness agrees with theory: decay time decreases with decreasing well thickness. The data on decay time .vs. temperature also agrees with the theory: in the limit of bandwidth far less than thermal energy kT, the exciton decay time is proportional to kT.

Kim et al. (71) reported a strong excitonic resonance in time-resolved (100 fs) four-wave mixing (two pulse self-diffraction configuration) in GaAs/AlGaAs MQWs as a function of the incident photon energy and showed that it results from the large difference in the dephasing rates of excitons and free carriers. They concluded that excitons dominate even when they make up only a small fraction of the excited states. The dephasing rate dependence on temperature was also measured to determine the exciton-phonon scattering rate. It was found that both the exciton and free carrier dephasing times decrease with increasing temperature and both acoustic and optical phonons contribute to exciton dephasing.

Schultheis et al. (72) investigated ultrafast phase relaxation of excitons in GaAs via exciton-exciton and exciton-electron collisions by degenerate four-wave mixing. In their experiment, the ultrafast relaxation of excitons in GaAs/AlGaAs, coherently excited by a short optical pulse and subjected to collisions with free

carriers and noncoherent excitons which are independently created by a second synchronized light pulse, was studied directly in the time domain by probing the excitonic phase coherence. The relaxation rates reveal strong exciton-exciton scattering with a collision efficiency of $1.6 \times 10^{-4} cm^{-4} s^{-1}$ and even 10 times more efficient exciton-free carrier scattering.

This same group (73) also investigated picosecond phase coherence and orientational relaxation of excitons in GaAs by time-resolved four-wave mixing at 2K. In their experiment, an optically thin layer of GaAs with a thickness in the range of 100 to 200 nm was used to reduce absorption and reabsorption of the nonlinear signal which normally prevents accurate data acquisition on unperturbed dynamics of excitons. The excitation density in the experiment was very low, so exciton-exciton scattering and exciton-electron scattering are unimportant and the observed relaxation times directly measure the residual interaction of excitons with phonons and impurities. The phase coherence was measured by a two-pulse experiment. For the orientational dephasing, diffraction of a delayed third pulse from an orientational grating formed by two orthogonally polarized pulses was analyzed by monitoring the randomization of the excitonic dipoles. They observed a surprisingly short phase coherence time of 7 ps and an orientational relaxation time of 7 ps independent of the excitation densities provided that the exciton density is below 2×10^{14} cm^{-3}. The results demonstrate that residual scattering of the excitons with acoustic phonons is much more efficient than the coupling to the photons.

Sucha et al. (74) conducted time-resolved measurements of carrier dynamics in bulk and quantum wells of InGaAs, using differential absorption spectroscopy. They found that the carrier thermalization time was 200-300 fs at comparable excitation densities and excess energies regardless of layer width for sample thickness ranging from 100 to 6000Å and the efficiency of screening relative to phase space filling was larger in the bulk than in the quantum wells. The excitation energy in their experiment was chosen so that the excess energy of photoexcited electrons is less than the LO phonon energy, thus carrier-phonon scattering can be neglected and the carrier-carrier scattering process can be studied exclusively.

Smith et al. (75) conducted a pump-probe investigation of biexcitons in GaAs/AlGaAs quantum wells. They observed biexcitonic contributions to time-resolved pump-probe measurements of 25 nm MQWs. Results from wavelength and polarization dependence studies of the differential transmission in the vicinity of the heavy-hole exciton transition demonstrated the strong influence of the biexciton state on the nonlinear response (induced absorption). When both the pump and probe pulses are σ^+ circularly polarized, biexciton transitions are not allowed due to the selection rule and the induced absorption disappears. Biexciton formation was also confirmed by its superlinear photoluminescence intensity dependence on excitation density.

Zinc Selenide Based Quantum Wells

ZnSe based quantum wells are the most promising candidates for short wavelength (blue-green) emitting devices. However, devices based on ZnSe

quantum wells haven't been realized, partly because the material quality still needs to be improved, and partly because the physics of the lasing mechanism and hot carrier dynamics in this material is not quite well understood compared to that in GaAs quantum well devices. Over the past few years, research efforts have focused on ZnSe quantum wells and some of the progress is discussed in the following. Clearly, much more research on this material is needed before an unambiguous understanding is achieved.

Kim et al. (76) conducted femtosecond four-wave mixing experiments in ZnCdSe/ZnSe multiple quantum wells at 10K. Extreme high order nonlinear diffracted signals (up to 13th order) were found in two beam, self-diffraction geometry. Diffracted signals of all observed orders were shown to originate predominately from excitonic resonances. Using four-wave mixing, an indication of hole-LO phonon scattering between the heavy and light hole states was found (lh exciton dephases much faster than hh exciton) and exciton-phonon interaction was studied by investigating the temperature dependence of the FWM signal. The temperature dependence data were fitted theoretically and yield acoustic phonon-exciton coupling constant of 8.3μeV/K and optical phonon-exciton coupling constant of 81meV for the hh excitons, which were much stronger than those of GaAs quantum wells.

Becker et al. (77) investigated femtosecond dynamics of exciton bleaching in II-VI CdZnTe/ZnTe quantum wells at room temperature by transient absorption measurements with both filtered probe and broadband probe. Compared to III-V

GaAs quantum wells, II-VI structures have carriers about one order of magnitude colder due to the higher exciton binding energy and smaller LO phonon energy. The carrier relaxation physics is expected to be different in the two systems. An exciton ionization time of 110 fs was determined (compared to 300fs in GaAs), and the bleaching strength of excitons on excitons were found to be larger than that of a comparable density of "cool" free carriers (same as in GaAs), which is opposite to what current many body theory (78) predicted.

Ding et al. (78) investigated gain and dynamics in separate confinement ZnCdSe/ZnSSe/ZnMgSSe quantum well heterostructure diode lasers from 77K to room temperature by both steady-sate and time-resolved photoluminescence. The gain spectral lineshapes were derived and show the pronounced effects of contributions by optical phonon scattering and electron-hole interactions. These effects suppress the maximum gain predicted from simple theory and provide gain in the low-energy region of the spectrum where optical attenuation by the uninverted portion of the optical volume is reduced. Radiative lifetime data also demonstrated the presence of this interaction.

The same group (79) also studied the origin of gain and laser action in optically pumped CdZnSe/ZnSe MQWs using both steady state spectroscopy and transient absorption/pump probe. They found that the origin of gain and laser action was of excitonic nature based on the following set of evidences: lasing action occurs at the low energy side of the exciton line and doesn't move with increasing excitation densities; pump-probe experiments show the presence of real gain at

probe energies on the low energy side of the exciton. A hypothesis was proposed which is based on exciton energy relaxation to lower energy states of the line, phase space filling of these states, and exciton-exciton interaction.

Kreller et al. (80) investigated strain, confinement, carrier dynamics and high density effects in ZnSe/ZnMnSe quantum structures grown by MBE. Steady state photoluminescence and excitation spectroscopy as well as time-resolved luminescence by streak camera were used. Steady-state measurements demonstrate an enhanced effective band offset due to tensile strain and a confinement induced shift of excitonic resonances up to 100 meV. Time-resolved results reveal progressive localization of the excitons on a 10 ps time scale followed by rapid recombination within 100 ps. With increasing excitation density, optical gain appeared in the lower energy side of the exciton line and was attributed to stimulated emission from degenerate e-h plasma. Optical gain on the order of $100cm^{-1}$ was observed under $400KW/cm^2$ excitation.

Stevens et al. (81) studied exciton dynamics and recombination in ZnSe/ZnSSe superlattices by differential transient absorption and time-resolved photoluminescence using a streak camera at 8K. At an excitation density of 10^{18} cm^3, below the threshold for stimulated emission, the time-resolved behavior of the lasing transition was a combination of behaviors of free excitons and localized excitons, and pump-probe results showed induced absorption above and induced transmission below the hh exciton line. They suggest that stimulated emission in the structure involves strong interaction between free exciton and LO phonons

$h\upsilon(E_{hhx})\rightarrow h\upsilon(\text{laser})+h\upsilon_{LO}$. However, since the excitation density they used was below the threshold density for lasing, direct predictions of a lasing mechanism may not be valid.

Semiconductor Devices

In addition to investigating carrier dynamics in semiconductor bulk and quantum structures, time-resolved techniques also provide an excellent means of studying transport dynamics of carriers in semiconductor devices. Some of the progress achieved on device transport studied in the past is reviewed in this section.

Tunneling

The dynamics of tunneling, which determine high frequency response of resonant tunneling diodes, has been investigated extensively in recent years by using it as a model for studying issues in quantum transport such as quantum interference effects (83). A resonant tunneling diode (RTD) consists of a double barrier structure (DBS) surrounded by doped cladding layers with contacts. Transmission through a DBS has peaks associated with quasi-bound or metastable states in the quantum well. The transmission resonance can be characterized by Γ, the full width at half maximum of the transmission curve for each quasi-bound state. The lifetime of the metastable state, or the escape time τ_{ee} of electrons in the quantum well, is related to Γ by $\tau_{ee}=\hbar/\Gamma$. The escape time determines the charge buildup in the quantum well and ultimately affects the speed of RTDs.

Time-resolved measurements provide an excellent technique for determining the escape time of electrons and holes out of the quantum well through barriers. If this escape time is shorter than the normal recombination time, it can be simply determined by measuring the decay of the luminescence intensity following pulsed excitation of quantum well. Such an experiment was first conducted on GaAs/AlGaAs DBS by Tsuchiya et al. (84). The measured escape time increases nearly exponentially with the barrier thickness and then saturates because it becomes comparable to the recombination lifetime.

Norris et al. (85) measured the dependence of the escape times on an applied electric field for a GaAs/AlGaAs DBS with one thin barrier and another thick barrier embedded in a p-i-n structure. The escape time decreases with increasing electric field because the effective barrier thickness decreases. Jackson et al. (86) also studied the escape times in a GaAs-AlAs DBS using a luminescence correlation technique. All the measurements above were performed on DBS without the doped cladding layers, so they didn't correspond exactly to actual device applications. Preliminary measurements on actual devices using electrooptic techniques have been reported (87, 88).

Investigations of tunneling dynamics between adjacent wells were conducted in an asymmetric double well structure (a-DQWS) which consists of a wide well and a narrow well separated by a barrier. The a-DQWs provides a unique spectral signature for each well, so that time-resolved optical measurements can be used to determine the escape and arrival of carriers in each well. By choosing different

structures and appropriate perpendicular electric fields, various resonant and nonresonant processes for electrons and holes can be isolated and investigated directly.

A large number of time-resolved experiments on a-DQWS have been reported in the literature. Tada et al.(89) conducted time-resolved experiments on isolated a-DQWs with 300 ps time resolution. Norris et al. (90) reported the dynamics of charge transfer luminescence (electrons and holes in separate wells). Oberli et al. (91, 92) reported a quantitative determination of electron tunneling rates and a demonstration that electron resonances strongly enhance tunneling rates (93). The same group also investigated the effect of barrier thickness on tunneling rate and observed a threshold in the tunneling rate at the optical phonon energy (93, 94), demonstrating the importance of optical-phonon-assisted tunneling processes. Many other studies on tunneling have been reported, primarily using time-resolved luminescence spectroscopy. These studied include resonant and nonresonant processes as a function of well thickness (95, 96) and electric field (97, 98). Tunneling between two quantum wells has also been used to demonstrate fast recovery of excitonic absorption (99, 100). In addition, resonant and nonresonant tunneling of holes has been investigated (101, 102), demonstrating the importance of collisions and relaxation on tunneling.

Ballistic Transport

At very low temperatures the main scattering mechanism that electrons experience is due to ionized impurities. If these impurities are removed from the

electron gas, ballistic transport over extremely long distances could take place, provided that the potential difference across the device is small. Ballistic transport in a two dimensional electron gas (2DEG) where electrons are separated spatially from their parent donors forms the basis of ultrafast MODFET and SISFET switching devices. The dominant scattering of hot electrons in a 2DEG at low temperatures is due to cold electrons and plasmons, and due to emission of optical phonons. Elastic scattering is mainly due to impurities in the 2DEG region and to remote parent donors intentionally introduced into an existing adjacent barrier. In regions where the carrier concentration is low and injection energies are small, inelastic scattering is the main mechanism limiting the mean free path.

Ballistic transport of cold electrons in 2DEG was confirmed before by measuring the quantized ballistic resistance (103, 104), and the mean free path has been shown to be many microns long by magnetic focusing experiments (105, 106). For hot electrons, the methodology of injection and spectroscopy, is direct and suitable. The principle of injection and spectroscopy is to inject energetically narrow electron beams and varying their mean energy by employing a tunnel barrier injector and then a spectrometer consisting of a simple potential barrier acting as a high-pass filter is used to collect electrons with energies exceeding its potential barrier. The carrier momentum distribution can be mapped out by changing the barrier height of the spectrometer. To a good approximation, the momentum distribution is proportional to the carrier distribution.

Heiblum et al. conducted detailed studies of hot electron transport in a three-terminal, lateral tunneling GaAs/AlGaAs hot-electron transfer amplifier device by this technique (107). They found that below 36 meV (LO phonon energy) the mean free path of hot electrons can be very long (an order of magnitude higher than theoretically predicted), on the order of the mean free path of the cold ones. By investigating electronic velocity .vs. injection energy in the presence of magnetic field, they resolved this discrepancy by discovering a new mechanism where hot electrons traverse the sample in higher subbands while the cold ones occupy the lowest one. The electron-electron mean free path is thus enhanced due to the reduced overlap between hot electrons and cold ones.

CHAPTER 4
CARRIER DYNAMICS INVESTIGATION OF II-VI SEMICONDUCTOR FILMS AND QUANTUM WELL STRUCTURES
(ZnSe FILMS AND CdZnSe/ZnSe MULTIPLE QUANTUM WELLS)

In this study, a carrier dynamics investigation was conducted in ZnSe epitaxial films and ZnSe based quantum well structures grown by molecular beam epitaxy. The motivation for this work is to understand the mechanisms of stimulated emission as well as basic hot carrier physics (ie. exciton bleaching, exciton-phonon interaction) in ZnSe three dimensional and two dimensional structures.

Properties And Applications of II-VI Semiconductors

Common II-VI semiconductors include ZnSe, ZnTe, CdTe, CdSe. They have direct and wider bandgaps than GaAs which make them attractive for optoelectronic applications. Among them, ZnSe has attracted much attention as a promising candidate for fabricating blue/green light emitting devices as well as optical switches. Figure 4-1 shows the detailed band diagram of ZnSe (108). Some of the important parameters of ZnSe are tabulated in tables 4-1 and 4-2 (1, 109). ZnSe assumes a cubic zinc-blende crystal structure characterized by three-fold degeneracy of the valence band: heavy-hole, light hole, and split-off bands. Two parallel cleavage planes in ZnSe structure provide the Fabry-Perot cavity necessary for a laser. N type doping of ZnSe is easily achievable and the common dopant is chlorine. The development of ZnSe diode lasers has long been hindered

by the lack of p doped material (doping concentration is limited by self-compensation effect). Since the achievement of p-type doping by using a nitrogen plasma (49), lasing has been observed in ZnSe although the lifetime of lasers is extremely short due to the presence of the native defects existing in the material and their subsequent propagation. More research efforts are needed to improve the quality of the epilayers.

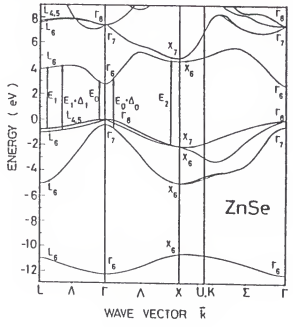

Figure 4-1 Electronic energy-band structure of ZnSe (108).

Table 4-1. Energies of CP's and positions of peaks in the optical spectra of ZnSe at 300 K (in eV)

E_0	$E_0+\Delta_0$	E_1	$E_1+\Delta_1$	E_0'	E_2	$E_2+\delta$	E_1'	$E_1'+\Delta_1'$	d_1	d_2
2.67	3.10	4.7								
		4.85	5.2	8.5	6.7		9.1			13.5
		4.80	5.1							
		4.80			6.5	7	9		10.6	13.8
		4.73	5.03	8.45	6.6	7.2	9.25	9.6		13.4
2.67	3.10	4.75	5.10		6.7		9.1	9.6		
2.69	3.10	4.8	5.1							
		4.75	5.05		6.50		8.46	8.97		
					6.63					
					7.15					
2.663		4.8	5.05		6.42					
					6.7					
2.692										
2.688										

Table 4-2 Properties of ZnSe

crystal structure	cubic zinc-blende
Energy bandgap (in eV)	2.82 (at 0K)
	2.67 (at 298K)
lowest conduction band minimum	[000] direct
exciton binding energy (in meV)	19 (at 10K)
effective masses	$0.17m_0$ for electrons
	$0.75m_0$ for holes
Luttinger parameters	4.3 γ_1
	1.14 γ_2
	1.84 γ_3
dielectric constant	9.14 ϵ_0
	6.3 ϵ_∞
index of refraction	2.89
lattice parameter (in Å)	5.6676
density (g/cm^3)	5.28 (at 4K)
Debye temperature (K)	339
melting point (K)	1793
thermal conductivity (W/cm·K)	0.19
optical phonon energy (meV)	31 (longitudinal)
	26 (transverse)
mobility ($cm^2/V·s$)	500 @ 300K (electron)
	30 @ 300K (hole)

The emergence of ZnSe quantum well structures fabricated by MBE offers better choice for device applications. The major advantages of quantum confined structures are the tunability of the bandgap and the higher optical nonlinearity at excitonic resonance. As a consequence, quantum well LEDs (light emitting diodes) and lasers have demonstrated improved quantum efficiency and a wide range of emission wavelengths. There are several kinds of ZnSe-based quantum well structures: one consists of $ZnSe/Zn_xMn_{1-x}Se$ quantum wells with ZnSe as the well material and $Zn_xMn_{1-x}Se$ as the barrier material; another one consists of $ZnSe/ZnS_ySe_{1-y}$ quantum wells with ZnSe as the well material and ZnS_ySe_{1-y} as the barrier material; and another one consists of $Cd_xZn_{1-x}Se/ZnSe$ quan*tum wells with ZnSe as the barrier and $Cd_xZn_{1-x}Se$ as the well material. All three systems are of type I superlattice structures in which both electrons and holes are confined in the well region. Among them, ZnSe/ZnMnSe and ZnSe/ZnSSe systems have the capability of tuning the emission wavelength into deeper blue spectral range, and CdZnSe/ZnSe system can be tuned into the deep-green spectral range. Since in quantum well structures, the thickness of each layer is very thin (about 100Å) and below the critical thickness, so the layers are strained in the presence of lattice mismatch between barrier material and well material. The strain has the effect of shifting the band edge of heavy-hole and light hole excitons. In $Cd_xZn_{1-x}Se/ZnSe$ and $ZnSe/ZnS_ySe_{1-y}$ systems, compressive stresses are present in the well layers, while in the $ZnSe/Zn_xMn_{1-x}Se$ system, tensile stress is present in the well layers. Among these three systems, $Cd_xZn_{1-x}Se/ZnSe$ system is the most promising

candidate. This structure can be grown with higher structural quality and exhibits very high nonlinear gains at moderate injection currents (110, 81). Present blue-green quantum well diode lasers are fabricated from this structure. However, one major problem associated with these lasers is the very short device lifetime which is believed to be due to the presence of pre-existing defects and their subsequent propagation in the material during device operation. Efforts are now being made to improve material quality and this problem may eventually be overcome. An excellent review on physical features and device characteristics of CdZnSe/ZnSe QW diode lasers is given by Nurmikko and Gunshor (111).

Besides the device applications, the fundamental physics of II-VI semiconductors and quantum wells is very interesting. Compared to III-V materials, II-V semiconductors have smaller LO phonon energies and larger exciton binding energies. Consequently, free carriers in II-VI material are "colder" and the screening dynamics as well as carrier-phonon scattering process will be different. For example, in III-V quantum well structures, ionized excitons yield "hot" free electron-hole pairs ($kT/E_x \approx$ 3-10, T is the carrier temperature), since the LO phonon energy ($h\nu_{LO} \approx$30-40 meV) is much larger than the exciton binding energy ($E_x \approx$1-8 meV). As a result, ionized e-h pairs in III-V QWs have initially very large excess energies and remain hot. In II-VI QWs, however, E_x (≈30-40 meV), $h\nu_{LO}$ (≈31 meV), and kT are all comparable. In such a case, the ionized e-h pair from the resonantly created exciton is initially cold and stays cold at equilibrium. The dynamics of exciton ionization and screening in II-VI QWs as compared to that in III-V QWs will

be very interesting to investigate to gain further insights into the many body physics (bandgap renormalization, phase space filling) of excited semiconductor QWs. Enhanced carrier-LO phonon interaction and reduced exciton bleaching are expected in II-VI QWs from current theories.

One of the most remarkable features of II-VI quantum wells is the strong excitonic effect present even at room temperature due to the large exciton binding energy (for $Cd_{0.2}Zn_{0.8}Se/ZnSe$, $E_x \approx 40$ meV). Given the strong excitonic effect in the QW structure, a closer examination of the microscopic mechanism responsible for gain and stimulated emission is appropriate. Does the excitonic process play a role? Is the conventional degenerate electron-hole plasma model valid? Investigating the microscopic lasing mechanism in CdZnSe/ZnSe multiple quantum well lasers is of great research interest today. The details on this issue will be discussed in chapter 6.

Material Structures Studied

In this study, carrier dynamics investigations are conducted on ZnSe crystal, ZnSe epitaxial films (doped and undoped), and CdZnSe/ZnSe multiple quantum wells at both room temperature and low temperatures. The ZnSe single crystal was purchased from Sumitomo Electric Inc. and was fabricated by vapor phase transport method (VPT) at very high quality. ZnSe epitaxial films and CdZnSe/ZnSe multiple quantum wells (MQWs) were fabricated by molecular beam epitaxy (MBE) by Dr. Robert Park's research group at the University of FLorida. All ZnSe epitaxial films were grown on GaAs substrates to 2μm thickness. The p type films were doped by

nitrogen plasma and the n-type films were doped with chlorine. The doping concentrations were found by Hall measurements to be in the order of $10^{17}/cm^3$ for both n- and p-type films. MQW samples are undoped and were grown in a variety of well thickness and barrier thickness combinations. The general sample structure consists of a substrate, a 2μm ZnSe buffer layer, and undoped MQWs of period of 10. Most MQW samples were grown on GaAs substrates heteroepitaxially except one which was grown on a ZnSe substrate homoepitaxially. Tables 4-3a and 4-3b summarize the characteristics of all samples used in this study.

For epitaxial films, the role of dopants on exciton dynamics was determined at low temperature. The role of defects such as nonradiative deep level centers on carrier lifetime behavior in band-to-band recombination process was investigated at room temperature. Also, hot carrier dynamics at high densities (carrier-carrier scattering, plasmon-phonon coupling) were examined.

For CdZnSe/ZnSe MQWs, the roles of well thickness and barrier thickness on carrier localization and tunneling were studied in detail. Exciton dynamics at high densities were examined (biexcitons, exciton-biexciton coupling) to determine the microscopic mechanisms responsible for gain and stimulated emission as well as hot carrier relaxation processes in this material system.

Table 4-3a Characteristics of MQW Sample Structures

MQW sample ID	1	2	3	4	5	6
substrate	GaAs	GaAs	GaAs	GaAs	GaAs	ZnSe
Cd concentration	0.2	0.2	0.2	0.2	0.2	0.25
well width (Å)	25	50	50	50	100	50
barrier width(Å)	100	50	100	200	100	200
# of QW periods	10	10	10	10	10	10

Table 4-3b Characteristics of Bulk Samples

bulk sample ID	1	2	3	4
substrate	GaAs	GaAs	GaAs	none
dopant	nitrogen	chlorine	undoped	undoped
thickness	2μm	2μm	2μm	1mm
carrier concentration cm^{-3}	10^{17} p	10^{17} n	10^{8}	10^{6}
fabrication technique	MBE	MBE	MBE	VPT

Fabrication By Molecular Beam Epitaxy

Molecular beam epitaxy (MBE) is a high-vacuum technique for the growth of epilayers, usually semiconductors, that utilizes thermal beams of source atoms or molecules impinging on a single-crystal substrate. The ultrahigh vacuum nature of the process permits in situ metallization and growth of insulating materials on freshly grown semiconducting surfaces resulting in contamination-free interfaces. The biggest advantages of MBE are its precise control over film thickness and doping profile and in situ deposition of metallic and insulating layers. Ultrathin layered structures and superlattice structures (resolution less than 10Å) have been

grown by MBE and modulated doping of superlattice structures has yielded increased mobility over uniformly doped structures. Many optical and electronic devices have been prepared by MBE, such as field effect transistors with high power gain (112), millimeter-wave Schottky mixer diode with very low noise temperature (113), and GaAs/AlGaAs double heterostructure lasers lasing at room temperature (114).

A typical MBE system is shown in figure 4-2 and Figure 4-3 (115). It is typically stainless-steel bell-jar system, ion pumped, with normal base pressures ≈1 x 10^{-10} torr after an 8 hour bakeout. The systems shown here are equipped with electron guns and energy analyzing optics for Auger spectroscopy and with the provision for reflection electron diffraction (RED) and/or low energy electron diffraction (LEED). Surface reconstruction as well as crystalline quality can thus monitored during growth. Quadruple mass spectrometer is used for residual gas analysis and analysis of the molecular beams. All constituents are directed at the substrate as molecular or atomic beams. The beams are derived from thermal effusion cells whose temperatures are accurately controlled within ±2° by negative feedback of a thermocouple, which is equivalent to a flux generation of ±7% or better for most elements. A requirement for the effusion ovens is a very low production of impurities in the molecular beam, either from outgassing or from reaction of the crucible walls with the contents. Pyrolytic BN has a very low rate of gas evolution and is commonly used. The addition of an air-lock sample exchange

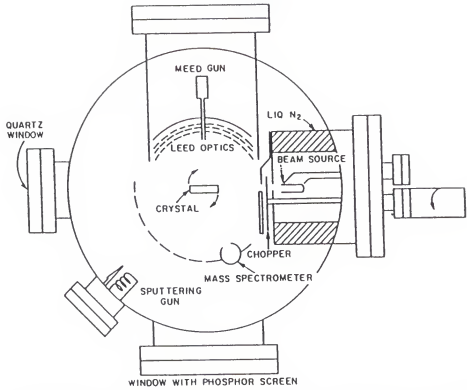

FIG. 2. Top view of MBE system used for measurement of beam reaction kinetics.(115)

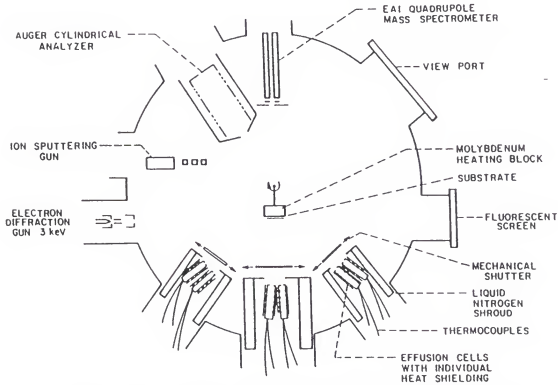

FIG. 3. Top view of MBE system used for the growth of multi-layered devices.(115)

mechanism permits rapid insertion of wafers without breaking the vacuum in the growth chamber.

An advantage of MBE is that only the source cells and the substrate are heated; this greatly reduces outgassing from the walls. Outgassing is further reduced by providing cryogenic pumping in the form of liquid nitrogen filled chambers surrounding the source ovens as shown in the figures. In order to reduce the unused material to flux into the chamber, a plate with beam-forming apertures is mounted on the liquid nitrogen cooled shroud. By means of externally controlled shutters the beams can be intercepted in order to abruptly alter the film composition. The ease of switching "on" or "off" is the main advantage of the use of atomic or molecular beams for growing thin films.

Ideally, the beam source should be a Knudsen cell containing vapor and condensed phases at equilibrium; in this case the flux F at the substrate is given by the Knudsen equation:

$$F = \frac{P_{(T)}a}{\pi L^2\sqrt{2\pi mkT}} \text{ molecule /cm}^2\text{sec}$$

where $P_{(T)}$ is the equilibrium pressure at the cell temperature T, a is the area of the cell aperture, L is the distance to the substrate, and m is the mass of the effusion species. Designs for knudsen cell sources have been described by Foxon and coworkers (116). In practice, a wide aperture is needed to provide a useful rate of mass transfer and smaller cells are desirable so that several may be placed in close proximity to the substrate. Tubular crucibles open at one end made from pyrolytic

BN or high purity graphite are generally used. The crucibles are mounted within spiral Ta heater windings which are themselves enclosed within Ta foil radiation shields. These cells have desired features of small size (~1.5"x3/4"), low gas evolution, rapid thermal response, low radiant power loss, and uniform heating.

Substrate cleaning is a very critical step in MBE growth. Depending on the substrate material, different cleaning techniques have been developed. Thermal heating, ion bombardment followed by elevated temperature annealing, hydrogen plasma etching, and UV irradiation are commonly used methods.

Since MBE is an epitaxial growth technique, the choice of substrate and growth temperature directly determines the film quality. Lattice mismatch and thermal expansion coefficients are very important parameters to consider in heteroepitaxial growth where films are grown on single crystal substrates of a different material. Below the critical thickness (pseudomorphic regime), films assume the same lattice parameter as the substrates and are under stress. Above the critical thickness, films are fully relaxed and dislocations caused by lattice parameter and thermal expansion coefficient mismatch start to propagate through the film and degrade the film quality. For the material system under study, ZnSe epilayers on GaAs substrates (a_{GaAs}=5.653Å, a_{ZnSe}=5.667Å), the lattice mismatch is about 0.27% and the thermal expansion mismatch is about 17%, which yield a critical thickness of 180nm. Thus growth of ZnSe on GaAs below the critical thickness results in an in-plane biaxial compressive strain in the ZnSe being counteracted by greater thermal contraction during cooling down. If samples are

grown thicker than critical thickness, misfit dislocation are created in the ZnSe layer which leads to gradual strain relaxation. All our ZnSe epilayer films are of 2μm thick, well above the critical thickness, so the films are fully relaxed. For the MQW structures under study, 2μm of ZnSe buffer layers were grown before the growth of multiple quantum well structures. The purpose of this 2μm buffer layer is to relax the ZnSe layer completely and damp out the imperfections from the film-substrate interface, so that subsequent MQW growth can be based on a nearly defect-free ZnSe surface (117). Each layer of the MQWs is very thin (below the critical thickness), so the quantum well layers are strained. For CdZnSe/ZnSe system, CdZnSe well layers are under compressive stress because CdZnSe has a larger lattice parameter than ZnSe. The effect of stress on band structure is to shift the valence band states relative to the conduction band states. A detailed calculation of the shifts will be presented in chapter 6. The MQW structures studied were grown at different well and barrier thickness combinations with a period of 10 (well/barrier thickness in Å) as follows: 50/50, 50/100, 50/200, 25/100, 100/100. All samples are undoped. These structures can only be possibly grown by MBE, since precise thickness control over each ultrathin layer is essential.

Another form of epitaxy is called homoepitaxy where epilayers are grown on single single crystal substrates of the same material. In this case, the problem of lattice parameter and thermal expansion mismatch is eliminated. However, since the two materials are the same, diffusion of impurities from substrates into epilayers becomes much more enhanced. Consequently, homoepitaxial growth puts very

stringent requirement on the substrate quality. For ZnSe, extremely high quality single crystal ZnSe substrates are still lacking at present, so homoepitaxial growth of high quality ZnSe films has not been possible. In fact, the quality of current homoepitaxial films is far inferior to that of heteroepitaxial films grown on GaAs despite the fact that misfit dislocations are present in the latter case. In this study, one of the MQW samples investigated was homoepitaxially grown on a ZnSe substrate. The comparisons of optical properties between this sample and others grown on GaAs substrates will be presented in chapter 6.

CHAPTER 5
EXPERIMENTAL TECHNIQUES USED AND THEIR SETUPS

In this chapter, two time-resolved techniques used in this study are discussed in detail, including their basic principles and experimental setups: one is a nonlinear luminescence correlation technique called excitation correlation spectroscopy (PECS) or population mixing, the other one is a pump-probe technique called differential transient absorption (DTS). The former technique is a measure of the products of electron and hole occupation functions ($f_e \cdot f_h$) and thus gives information on recombination dynamics; while the latter one is a measure of the sum of the two occupation functions ($f_e + f_h$) and thus gives information on carrier thermalization process. By combining these two techniques, an overall scenario of carrier relaxation dynamics can be obtained.

Ultrafast Ti:Sapphire Laser System As The Excitation Source: General Characteristics And Operating Principles

The emergence of Ti:Sapphire femtosecond pulsed laser system has provided a major breakthrough in the area of ultrafast spectroscopy. This system generates pulses with femtosecond duration, high repetitation rates (76MHz), wide-range wavelength tunability (UV to IR), and high pulse energy (up to several μJs), sufficient to generate a white light continuum. Femtosecond pulse duration allows us to investigate carrier relaxation processes occurring in a wide range of time

scales, down to the pulse width in the femtosecond regime; the high repetition rate reduces data acquisition time; the wavelength tunability makes it possible to study different semiconductor materials (e.g., materials with different bandgaps) as well as various processes at resonances for a particular material; the high pulse energy allows the study of nonlinear processes and many-body interaction in semiconductors. The white light continuum is an ideal tool for probing carrier thermalization processes over a broad energy range in pump-probe experiments.

The Ti:Sapphire ($Ti:Al_2O_3$) laser system consists of a continuous wave (cw) Ar ion pump laser, a Ti:Sapphire femtosecond passively modelocked oscillator (Mira), a Ti:Sapphire regenerative amplifier (Rega), and an optical parametric amplifier (OPA). A schematic layout is shown in figure 5-1. The Ar ion pump laser produces 22 Watts of multiline radiation in the blue-green spectrum from 457 to 515nm. The output is in a high beam-quality, low divergence TEM_{00} mode. The single Argon ion pump beam is directed into the femtosecond oscillator with a single mirror and mount. At the base of the pump control optical assembly inside the oscillator, the 22W pump beam is divided by a beamsplitter into 8W to pump the oscillator (Mira) and 14W to pump the amplifier (Rega).

The 8W oscillator pump beam is directed to the Ti:Sapphire crystal of the Mira in the normal pump geometry shown in figure 5-2. The oscillator in femtosecond modelocked operation produces an ultrafast pulse train with 500mW average power. A typical pulsewidth is 120fs (180fs autocorrelation). The output is tunable from 740nm to 1070nm, but for optimum Rega operation, the Mira is tuned

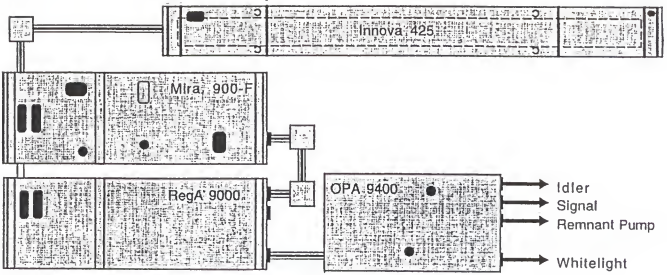

Figure 5-1 System configuration of Ti:Sapphire ultrafast pulse laser system.

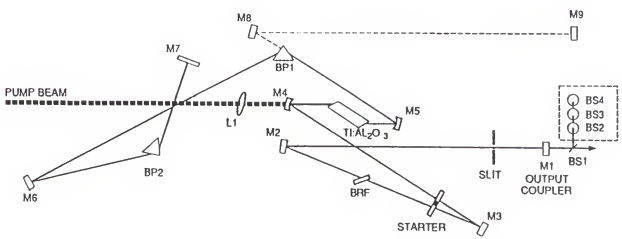

BP : Brewster prism
BRF : Birefringent filter
BS : Beamsplitter
L : Focusing lens
M : Mirror
$TiAl_2O_3$: Titanium:sapphire crystal

Figure 5-2 Optical schematic of Ti:Sapphire femtosecond oscillator (Mira).

to the peak of the Ti:Sapphire gain at 800nm. The output power of both Mira and Rega is maximum at this wavelength.

The remaining 14W of the pump laser passes through the beamsplitter, exits the opposite side of the Mira, and enters directly into Rega. This pump is then directed to the Ti:Sapphire crystal in the same geometry as in the Mira as shown in figure 5-3. A 120 fs pulse from the Mira oscillator is fed into the Rega amplifier with two turning mirrors and is injected into the amplifier cavity with a TeO_2 acoustic-optic cavity dumper. Amplification over 25 roundtrips allows the dispersion in the TeO_2 Q-switch in the Rega to expand this pulse to a 40 ps length. The cavity dumper then extracts a single pulse of several microjoule energy. At 250 kHz repetition rate, the average output power is 1W if the output energy per pulse is 4μJ. The accumulated chirp acquired by the pulses in amplification is canceled with a simple single-grating double pass compressor. At greater than 50% efficiency, the compressor produces microjoule pulses with autocorrelation pulsewidths of less than 300fs FWHM. A sapphire crystal (Al_2O_3) is used to generate stable, high efficiency broadband white-light continua from these pulses through a process called self-phase modulation.

The optical parametric amplifier is a wavelength conversion accessory for the regenerative amplifier system. The output pulses from Rega are sufficiently intense to allow efficient conversion by OPA to any wavelength in the visible from 500 to 700nm, called OPA signal, and simultaneously to a paired wavelengths in the near infra-red range from 940nm to 2400nm, called OPA idler. The OPA architecture

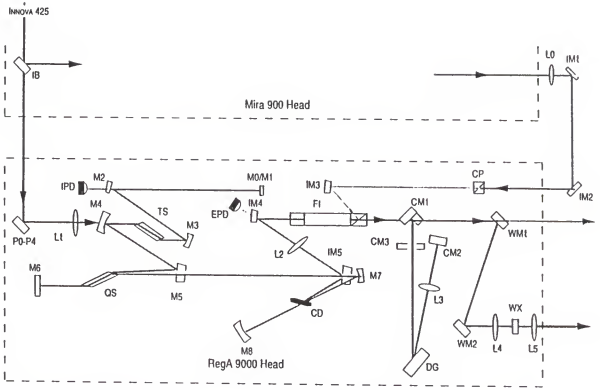

IB:	Ion Beamsplitter	WX:	White-Light Crystal
IPD:	Injection Photodiode	M0 - M8:	Cavity Optics
EPD:	Ejection Photodiode	IM1-IM5:	Injection Optics
QS:	Q-Switch	CM1-CM3:	Compressor Optics
CD:	Cavity Dumper	WM1 - WM2:	Whitelight Optics
FI:	Faraday Isolator	L0 - L5:	Lenses
CP:	Cube Polarizer	P0 - P4:	Pump Optics
DG:	Diffraction Grating	TS:	Ti:Sapphire Crystal

Figure 5-3 Optical schematic of Ti:Sapphire regenerative amplifier (Rega).

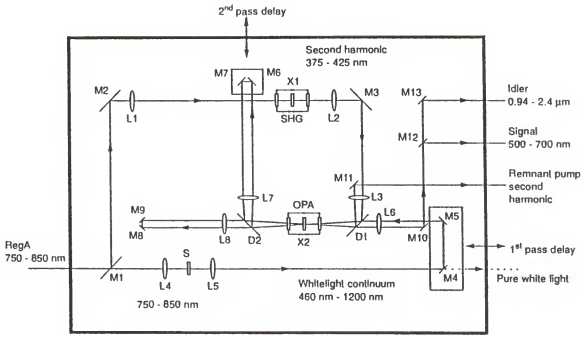

M: Mirror
D: Dichroic mirro
L: Lens
S: Sapphire crystal

OPA BBO: Optical parametric amplifier Beta Barium Borate crystal
SHG BBO: Second harmonic generator Beta Barium Borate crystal

Figure 5-4 Optical schematic of optical parametric amplifier (OPA).

(shown in figure 5-4) involves splitting the Rega output into two portions: one part (25%) generates a clean, low energy continuum to seed the OPA; the other part is converted to the second harmonic at 400nm to pump the BBO type I OPA crystal. Then these two parts are combined on a beamsplitter and focused in the OPA crystal. The crystal angle allows the selection of one wavelength out of the continuum and then strongly amplifies the signal at that wavelength. To increase the efficiency of optical parametric amplification process, the OPA crystal is double passed. Then using wavelength selective dielectric mirrors, the 400nm pump, the visible signal and the infrared idler are separated and passed out the front of the unit. A very small portion of white light continuum pulse is also outputed from OPA.

The ultrashort pulses available in the whole visible spectrum from Ti:Sapphire system fill the spectral gap that exists in the outputs of conventional colliding pulse modelocked Dye lasers (CPM), marking a major improvement in the field of ultrafast lasers. To gain further insights into the operation principles of the whole system, theories on the major processes utilized in this system are presented in detail next.

Processes in Mira Oscillator (122)

Modelocking

A detailed review on the theory of modelocking is given by Shank (118). A laser typically consists of a pair of mirrors which enclose a gain medium. The range of frequencies over which a laser will oscillate is determined by the gain bandwidth and the loss in the cavity. The precise frequencies which oscillate within this range

are determined by the resonator. The modes of oscillation of a laser are the self reproducing field distributions which are established in the optical cavity. A variety of such laser modes exist, some of which have field distributions normal to the resonator axis (termed transverse modes). Each of these transverse modes has an infinite set of eigenfrequencies or longitudinal modes separated in frequency by c/2L, where L is the optical length of the resonator and c is the speed of light. Normally only the lowest order fundamental modes having gaussian profiles are permitted to oscillate. The corresponding set of longitudinal modes consist of a picket fence of regularly spaced modes separated by c/2L. The number of modes which oscillate is limited by the bandwidth $\Delta\upsilon$ over which the laser gain exceeds the loss of the resonator as illustrated in figure 5-5.

In general, the relative phases between the modes are randomly fluctuating. If nothing fixes the relative phases, the laser output will vary in time although the average power will remain constant. If the modes are forced to maintain a fixed phase and amplitude relationship, the output of the laser will be a well defined periodic function of time, specifically, a train of regularly spaced pulses, and the laser is considered to be modelocked. The pulses have width $\Delta\tau$, which is approximately equal to the reciprocal of the total modelocked bandwidth, $\Delta\upsilon$, and temporal periodicity $T_p=2L/c$. The ratio of the pulsewidth to the period is approximately equal to the number of locked modes. A physical picture corresponds to a single pulse travelling back and forth between the resonator mirrors. Figure 5-6 illustrates a modelocked train.

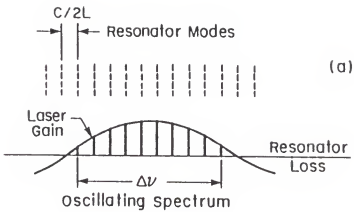

Figure 5-5 The resonator modes which oscillate are determined by the gain profile and the resonator loss (118).

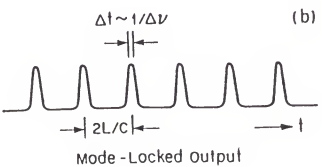

Figure 5-6 The temporal output of the laser with all modes locked in the proper phase.

There are two ways to modelock a laser: active modelocking and passive modelocking. In active modelocking, an intracavity phase or loss modulator driven at the frequency corresponding to the mode spacing is inserted into the optical cavity which acts like a shutter (119). Another way to actively modelock a laser is to use a modelocked laser as a pumping source. In this scheme, the two cavity lengths should be closely matched. Rapid modulation of the gain medium by the short optical pumping pulse provides the coupling mechanism to phase lock the cavity modes. Passive modelocking utilizes the insertion of saturable absorbing element inside the optical cavity. The saturable absorber is typically an organic dye but gases and solids have been used as well. Due to its unique property, the saturable absorber acts like a self-adjusting modulator which is modulated by the laser beam itself rather than an external control. This approach has proven to be extremely successful from the fact that the first optical pulses in the picosecond and femtosecond time domain were obtained by this method (120, 121).

For the Mira femtosecond oscillator, the saturable absorber system by which passive modelocking is achieved is quite unique. The Mira cavity has been designed so that the beam diameter within the cavity changes by a small amount as the intensity of the light changes. More specifically, the beam diameter at certain locations within the cavity is large when the laser is operating at continuous mode (CW) but become smaller when the laser is producing high intensity modelocked pulses. A simple slit is now placed at an appropriate location, and its width is adjusted so that the large diameter CW laser beam will be interrupted at its edges.

A high intensity pulse, however, will pass uninterrupted through the slit, since the beam is smaller. Thus, the modelocking saturable absorber consists of two parts: a material that decreases the beam size in the presence of high intensity pulses and a slit that introduces losses for large beams.

The phenomenon utilized to change the beam diameter is very interesting. The properties of light passing through any material depend on, among other parameters, index of refraction of the material n. The higher the n, the lower of the velocity of the light. If the velocity of light is different for different parts of the light beam, the beam will be reshaped (refraction), since different parts of the beam are travelling at different speeds. A common refractive element is a optical lens (e.g. a biconvex lens), which is thicker in the middle that at the edges, so that the center of the beam is slowed down more than the edges. This causes the beam to bend toward the center. A lens can also be formed by making the refractive index at the center of the material higher than the index at the edges. A gradient index lens is an example.

In Mira, the refractive index of the Ti:Sapphire crystal is changed by the light beam. At sufficiently high intensity, the electric fields associated with the light can actually distort the electronic bonds of the material and alter its index. This effect is known as optical Kerr effect. Since the beam is less intense at its edges as compared to the center, the index at center will be higher and a gradient index lens is formed. The Kerr lens is formed only when the intensity of the light is extremely high (10^5V/cm). The instantaneous intensity of modelocked light pulses are

sufficient to form this lens, but the weak intensity of CW beam is not. Hence, the lens is only formed upon arrival of a modelocked pulse. A mechanism has now been created which narrows the beam only for modelocked pulses. The addition of a slit to allow only narrow beams to pass unattenuated forms the complete saturable absorber system which provides the driving force for modelocking.

Now the question is how to generate sufficiently high peak power to open the saturable absorber system as a start. By changing the cavity length at the proper speed in the CW mode, very high power fluctuations can be induced. Once the instaneous power in one of these fluctuations becomes sufficiently high, a Kerr lens is formed, the beam is narrowed and can pass unattenuated through the slit. The pulse will become amplified and become the dominant pulse which will form the modelocked output. In principle, by changing the cavity length, the mode themselves can be shifted in wavelength. However, if the cavity length is changed rapidly enough, the previously oscillating modes will be dying out, leaving atoms available for the new modes and there will be a period during which both can be lasing simultaneously. Thus a transient condition has been created under which the output of the laser contains more longitudinal modes than normally possible. Once a larger number of modes are lasing, peak intensities are produced to initiate Kerr lens formation and modelocking process begins. Once modelocking starts, it will continue without the need of the starting mechanism. The length of the cavity is changed not by increasing the distance between the mirrors, but by tipping the angle of a glass plate through which the beam must travel. As the plate is tipped,

more glass must be transversed, and since light travels more slowly in glass than in air, it is entirely equivalent to increasing the distance between the mirrors.

Group Velocity Dispersion and Dispersion Compensation

The spectral content of an ultrashort pulse of light consists of a distribution of wavelengths on either side of the center wavelength. The width of the distribution is inversely proportional to the duration of the pulse based on Heisenberg uncertainty principle. In order to produce a very short pulse from the distribution, the timing or phase between each component wavelength must be controlled, or the pulse will not be as short as it could be. For example, an ultrashort pulse will become longer after it passes through glass. This is due to the fact that in all normal materials, the index of refraction, hence the speed of light varies nonlinearly with wavelength. Figure 5-7 is a dispersion curve typical of many transparent materials. The index decreases with increasing wavelength while maintaining a gradual curvature. If the curvature is upward as shown, then the material has normal dispersion, while a material having downward curvature is referred to having anomalous dispersion. The second derivative of the curve, $d^2(n)/d\lambda^2$, determines the group velocity dispersion (GVD), which governs the rate at which the frequency components of the wave packet change their relative phases. GVD causes temporal reshaping of wave packets—this can be broadening or shortening depending on the initial condition of the wave packet (chirp) as well as the transmitting material. If the blue components are retarded with respect to the red, the pulse is said to be positively chirped (+GVD). Similarly, a pulse is said to be negatively chirped if its

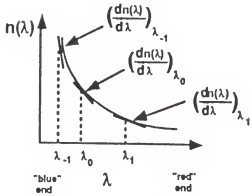

The curvature and hence GVD is determined by the 2nd derivative of the dispersion relation.

$$\frac{d^2n(\lambda)}{d\lambda^2} \propto \text{"Group Velocity Dispersion"}$$

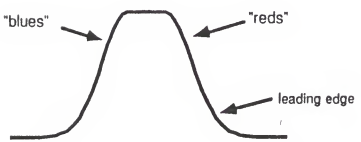

b. Positive Chirp — Red Frequency Components Lead The Blues (Results From + GVD)

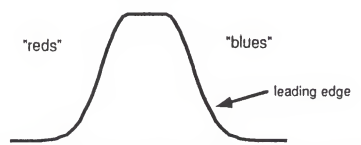

a. Negative Chirp — Blue Frequency Components Lead The Reds (Results From – GVD)

Figure 5-7 Illustration of group velocity dispersion (GVD).

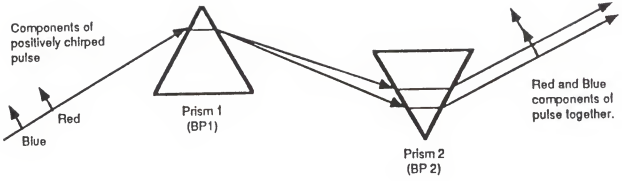

Figure 5-8 Schematic of GVD compensation with prism pairs.

red components have been retarded with respect to the blue (-GVD). Besides normal dispersion, self phase modulation (SPM) also introduces positive GVD, which results from the intensity dependence of the refractive index. The center of the pulse where the intensity is the highest will cause a bigger change in the index than the edges. This will cause part of the beam to move faster, thus altering the pulse shape.

Because of SPM and GVD from the many dispersive elements within the laser cavity, compensation must be employed to allow slow wavelengths to catch up with faster ones. An optical system must have a source of negative GVD in order to cancel the positive GVD accumulated from dispersive elements in the cavity. The optical system used in Mira to accomplish this task consists of a pair of prisms separated by a distance oriented in a specific way with respect to each other. The net GVD of this prism pair can be made negative by proper choice of prism material and the distance between them. Figure 5-8 illustrates the compensation scheme. The chirped pulse enters prism 1. Since prism bends or refracts different wavelengths into different angles, the beam spreads as it heads for the second prism. The blue components are bent more severely than the red ones (-GVD) thus creating wavelength dependence of optical paths for various rays. The amount of GVD compensation can be easily controlled by over a range of values by prism glass path adjustment. In Mira, the beam passes through the two prisms twice for complete GVD compensation.

Processes in Rega Amplifier (123)

A Ti:Sapphire amplifier pumped by CW argon laser has the potential for high repetition rate, and high average power amplification of ultrafast pulses. For pulsed operation, the Rega output power is only limited by the energy storage time of the gain medium. In Ti:Sapphire at room temperature, this storage time (T_2) is approximately 2.5μs. The maximum pulsed energy (E_p) expected is given by $E_p=P_{cw}T_2$, where P_{cw} is the CW power determined by the pump power. At repetition rates up to $1/3T_2$=130KHz, no decrease in pulse energy is observed. For higher repetition rates (R) the energy is reduced and follows the general form:

$$E_p \sim P_{cw} T_2 (1-\exp(-\frac{1}{T_2 R}))$$

At 250kHz, which is where Rega is routinely operated, the pulse energy is reduced to 80% of the maximum while the average power is 50% of the CW average power. However, the repetition rate has to be sufficiently high to allow faster data acquisition and averaging. This is seen as a reasonable compromise between the pulse energy, average power, and the repetition rate.

Q swithing

The Q switch in the Rega amplifier is an acoustic-optic (AO) modulator used to prevent lasing in the Rega cavity until a pulse from Mira laser is injected. This allows the Ti:S crystal to store energy for amplification of the injected pulse. The Q switch uses a thick Brewster angled TeO_2 crystal with AO transducer matched to respond to 80MHz RF excitation. The 80MHz acoustic wave generated by the RF excitation is aligned with the Brewster angle to diffract out part of the beam in the

cavity and hold off lasing. The Q switch is turned off suddenly and a single Mira pulse is injected into the cavity by the cavity dumper. After amplification over 25 round trips, the pulse is ejected by the cavity dumper. The Q switch is turned back on again to allow the storaged energy in the crystal to build up for the next pulse.

The Q switch has a second important function in the Rega cavity. The long TeO_2 Q switch is a highly dispersive element which stretches the Mira pulse in each roundtrip of the amplification to longer pulse lengths for safe energy extraction. The 10nm Mira pulse bandwidth and the GVD of the Q switch produce a significant stretching of the pulse. For safe energy extraction, the final pulsewidth after full amplification is approximately 40 ps. The total amount of dispersion is maximized by double-passing through the Q switch on each cavity transit.

Cavity dumping

The cavity dumper is a high speed acoustic-optic modulator used to inject and eject the single pulse amplified in the Rega cavity. It is a Brewster angled TeO_2 plate with an AO transducer matched to respond to 380MHz RF excitation. The 380MHz acoustic wave generated in the cavity dumper efficiently diffracts out any optical beam aligned at the Bragg angle. A electronic controller supplies a sufficiently short RF pulse to create a short acoustic pulse and diffract only one pulse out of 76MHz pulse train. Two pulses are launched into the cavity dumper by the controller; one to inject a pulse into the cavity soon after the Q switch is turned off; and a second to eject this pulse from the cavity after it has reached maximum energy.

The diffraction process of the cavity dumper AO modulator is induced by the interaction in a nonlinear medium between an acoustic wave and an optical wave. The acoustic wave, corresponding to the pressure modulation in the TeO_2 material, can be considered approximately as a plane wave. The index of refraction of TeO_2 is coupled to the modulating strain field of the acoustic wave through the photoelastic effect. The regions of compression and expansion exhibit different indices. The index distribution in TeO_2 constitutes a traveling optical phase grating which will diffract incident light beams.

One important limitation of diffraction efficiency is due to the speed of sound in the material. In the case of TeO_2, the speed is 4.2μm/ns. To select a pulse from the 76MHz Mira pulse train, the acoustic pulse time is limited to be less than the single cycle time of 13ns. The 4.2μm/ns speed of sound means that a 10ns acoustic pulse is only 42μm in width. An optical beam with a diameter in the cavity dumper cell greater than 40μm will therefore only have its center diffracted by the acoustic pulse. For Rega cavity, the beam diameter at cavity dumper is between 50 and 60μm, so this effect limits the diffraction efficiency. Reducing the spot size is not desirable because of potential for optical damage. To improve the diffraction efficiency, a double pass cavity dumper scheme is used in Rega as shown in the optical layout of Fig. 5-3.

Pulse compression

After full amplification in the Rega cavity, the 120 fs Mira pulse is stretched to about 40 ps pulse duration for safe energy extraction. The spectral content of the

pulse is not significantly altered (10nm) by amplification since gain saturation, gain narrowing, and self-phase modulation are all negligible in the Rega. For the level of pulse expansion in Rega, the material dispersion leads to higher order delays in the pulse-shape besides linear chirp from second order $d^2n/d\lambda^2$. The third order term, $d^3n/d\lambda^3$, also becomes important. The pulse compressor therefore needs to correct for both orders to bring the pulsewidth back to the original value.

The Rega pulse compressor contains a single holographic diffraction grating with a 4-pass configuration as shown in figure 5-9. This is accomplished by using a lens and mirror combination to relay-image the pulse from the front of the grating back onto itself. The operating principle can be understood in comparison with a standard, 4-pass, two grating compressor shown in the same figure. In the standard configuration two parallel gratings are used to first disperse in angle and then rediffract back parallel the range in wavelengths in a chirped pulse. This introduces a linear variation in optical path with wavelength and can be used to cancel linear chirp. The standard configuration retroreflects the beam after the first pass through the grating pair to reverse the spectral dispersion in space and reproduce the round input beam. An important advantage of the single grating 4-pass compressor is the addition of lens relay between gratings which allows the correction of third order dispersion. The third order dispersion term manifests itself as a non-centrosymmetric beam distortion between gratings and simply rotating the lens in the relay arm allows this to be canceled by an equal and opposite distortion. The

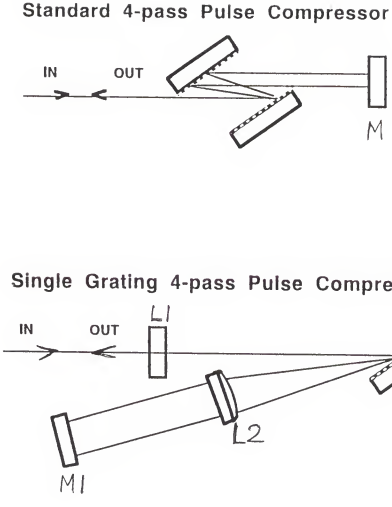

Figure 5-9 Configuration of Rega single grating, 4-pass pulse compressor as compared to that of the standard double grating, 4-pass pulse compressor. L: lense; M: mirror.

Rega compressor therefore allows the 40 ps output pulse to be compressed to around 200fs (300fs autocorrelation).

White light continuum generation

The recompressed output pulse from the Rega has several microjoules of energy and around 200fs pulsewidth. For a focused beam the intensity is sufficient to create strong whole beam self-focusing in most materials. This effect collapses the beam size and increases the laser intensity by another order of magnitude to the level where self-phase modulation has a drastic effect on the instantaneous phase of the optical pulse. The self phase modulation generates a rapid frequency sweep from the infrared to the ultraviolet.

Both self-focusing and self-phase modulation are based on the Kerr non-linearity of the refractive index with intensity, n_2. The time response of this non-linearity is on the order of 10fs. Whole beam self focusing is a nonlinear optical effect where the laser beam intensity leads to a significant increase in the local index of refraction in the material. The spatial variation of the Gaussian beam leads to change in index in space and creates a positive lens in the material which cause the beam to collapse on itself. The limit of this collapse is a beam diameter on the order of the wavelength of the light. The very high intensities in the collapsed filament are sufficient to increase the index variation even further. The temporal shape of the pulse creates a rapidly changing index in time which in turn changes the laser phase and frequency in time. Because of the slope of variation of intensity with time the leading edge of the pulse is converted to IR and the trailing edge to

UV. This self phase modulation conversion may be expected to be symmetric about the center wavelength except for the time response of n_2. This time response causes the trailing edge of the pulse to undergo self phase modulation more than the leading edge and therefore favors conversion to shorter wavelengths.

Process in OPA (124)

Optical parametric amplification

Optical parametric amplification is a nonlinear frequency mixing process. In OPA, the short wavelength beam (400nm) is called the "pump" and has the most power. The other input beam (white light) is called "signal" and the resulting difference frequency wave is called the "idler". Upon proper phase matching, the conversion process will occur where both the signal and idler waves grow with the pump wave decaying, i.e. pump photons are split into signal and idler photons: $h\upsilon_{pump} = h\upsilon_{signal} + h\upsilon_{idler}$. For a given pump wavelength (400nm), the phase matching can be achieved by rotating the direction of beam propagation through a birefringent crystal (type I BBO). Figure 5-10 shows the phase matching curve for type I BBO pumped at 410nm. By rotating the crystal just a few degrees the signal wavelength can be tuned from 500nm to 700nm and idler scans simultaneously from 933nm to 2000nm. A double pass scheme is used in OPA to improve conversion efficiency.

Population Mixing (or Excitation Correlation Spectroscopy): Principle And Experimental Setup

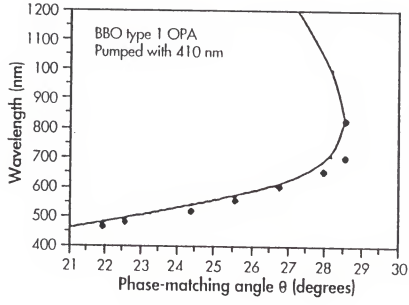

Figure 5-10 Phase-matching curve for BBO type 1 OPA. Experimental data points and fit to Sellneier prediction.

Population mixing is a nonlinear time-resolved luminescence technique. In this technique, an ultrafast pulse train is equally divided into two by a beamsplitter. One pulse train is given a variable time delay by a movable prism. The two pulse trains are modulated at different frequencies, ω_1 and ω_2, by mechanical choppers, and focused onto a semiconductor sample. The intensity of the luminescence is detected by a photomultiplier and measured by a lock-in amplifier tuned to the difference (or the sum) of the modulation frequencies. The correlation luminescence decay as a function of the time delay yields the carrier lifetime.

The underlying principle is as follows (27, 125): In the semiconductor the photogenerated electron and hole densities of the first pulse, at time t, are n(t) and p(t), and of the second pulse $n(t+\tau)$ and $p(t+\tau)$. The photoluminescence produced by radiative recombination of these carriers is given by

$$I_e(t,\tau) \propto [n_0 + n(t) + n(t+\tau)][p_0 + p(t) + p(t+\tau)], \qquad (5\text{-}1)$$

where n_0 and p_0 are background electron and hole densities. The two excitation pulses are repeated at rate N ($N \leq 1/T$, where T is the carrier lifetime). The total average signal measured by a slow photodetection system is given by the time integral

$$I_L(t,\tau) > \propto I_e(\tau) + I_B, \qquad (5\text{-}2)$$

where the signal at delay time τ is

$$I_s(\tau) \propto \int_{-\infty}^{\infty} n(t+\tau)p(t)dt + \int_{-\infty}^{\infty} n(t)p(t+\tau)dt, \qquad (5\text{-}3)$$

and the background is

$$I_B \propto (n_0 p_0 / N) \cdot 2\int_{-\infty}^{\infty} n_0 p(t)dt \cdot 2\int_{-\infty}^{\infty} p_0 n(t)dt, \qquad (5\text{-}4)$$

In the population mixing technique, the time delay dependence remains only in $I_s(\tau)$. The excited carriers from the first pulse mix and recombine with the excited carriers from the second pulse, generating the luminescence $I_s(\tau)$. The lock-in amplifier isolates the luminescence $I_s(\tau)$ from background I_B. If the lifetimes of the electrons and holes are T_E and T_H, respectively, $I_s(\tau)$ is given by

$$I_s(\tau) \propto \exp(-|\tau|/T_E) \cdot \exp(-|\tau|/T_H), \qquad (5\text{-}5)$$

The rate equations are used to derive relations for n and p. The theoretical results of lock-in signals is given by:[125]

$$\begin{aligned} I_{lock}(\omega_1) &\propto I_{lock}(\omega_2) \propto (Bg^2 T/4t_{rep})(1+e^{-|\tau|/T}) \\ I_{lock}(\omega_2-\omega_1) &\propto I_{lock}(\omega_2+\omega_1) \propto (\beta Bg^2 T/t_{rep})e^{-|\tau|/T} \end{aligned} \qquad (5\text{-}6)$$

Where T is the lifetime of electrons or holes, t_{rep} is the repetition rate of the pulses, g is the amplitude of the pulses, and B is the electron hole recombination rate.

$$\beta = \frac{4}{\pi^2}\sum_{n=0}^{n=\infty}\frac{1}{(2n+1)^3} \approx 0.136, \qquad (5\text{-}7)$$

For τ=0,

$$I_{lock}(\omega_2-\omega_1)/I_{lock}(\omega_1)\text{-}0.27$$

Therefore, It is possible to obtain the carrier lifetime T by monitoring the lock-in signal intensity verus the time delay. The relationship follows an exponentially decaying behavior as shown in the above equations.

Figure 5-11 illustrates the schematic of the experimental setup used in this study. The second harmonics from the ultrafast Ti:Sapphire Rega laser (280fs, 400nm, 250kHz)) was used as the excitation source. A 50/50 beamsplitter divides this beam into two beams. One beam goes through a motorized variable delay line (10cm travel range or 670ps delay range). The two beams are chopped at different frequencies, ω_1 and ω_2, by a dual frequency chopper and are focused to a 500μm spot size on the sample surface. The luminescence signal was spectrally resolved by a single grating, 640mm spectrometer and detected by a GaAs photomultiplier (PMT) tube. The voltage output from the PMT was amplified and input into a programmable lock-in amplifier. The lock-in amplifier was locked to either $\omega_1+\omega_2$ or $\omega_1-\omega_2$. The lock-in amplifier, spectrometer, and the delay line are controlled by a computer so that scans of signal versus wavelength or delay time can be made automatically. For low temperature measurements, the sample was maintained in a close-cycle helium cooled cryostat at 10K. A resistance heater was also mounted on the sample holder to allow the temperature of the sample to be adjusted. The overall temporal resolution of the system is that of the laser pulse, approximately

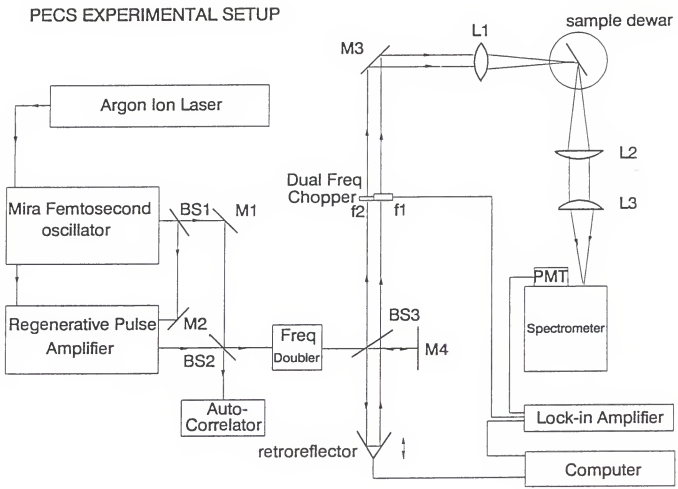

Figure 5-11 Schematic of population mixing experiment.

280fs. The zero time delay was calibrated at the maximum of the lock-in signal based on equation 5-5. The laser pulse energy can be tuned in a wide range of values.

This technique has two distinct advantages. One is its fast time resolution only limited by the pulse duration of the laser; the other one is the simplicity of the experimental setup. No fast detectors or other extensive instrumentation are required.

Transient Differential Absorption (or Pump-probe): Principle And Experimental Setup

The differential transient absorption (DTS) technique is a very valuable tool for the investigation of carrier thermalization processes in semiconductors. In DTS, a strong intensity ultrafast laser pulse (called the pump) excites the sample. A second beam (called the probe), much weaker than the pump, goes through a variable time delay with respect to the pump and is focused to the same spot on the sample. The probe sees the change in absorption characteristics of the sample induced by the pump. The transmission spectrum of the probe after the sample as a function of the time delay yields the absorption dynamics, which directly reflects the carrier thermalization process. There are two categories of pump-probe experiments: single wavelength probe experiments and broadband continuum probe experiments. In the former, the probe is fixed at a specific wavelength and only absorption dynamics in that wavelength are detected; while in the latter, a broadband probe is used to detect the absorption change in a wide range of

wavelengths. The broadband continuum experiments are more desirable since they also provide spectroscopic evidence for nonthermal distributions.

The basic principle follows: As described by the Pauli exclusion principle, the occupation of electron and hole states in any material will block further absorption at the corresponding photon energies. Mathematically, this principle can be expressed by $\alpha=\alpha_0(1-f_e-f_h)$, where α_0 is the initial absorption (absorption without the pump), α is the absorption in the presence of the pump, and f_e and f_h are electron and hole distribution functions respectively. The ratio $\alpha/\alpha_0=1-f_e-f_h$ gives a measure of the sum of electron and hole occupation functions. By measuring the absorption spectrum over a wide energy range using a broadband continuum pulse of ultrashort duration at various times after the pump, both temporal and spectral profiles of the occupation functions can be obtained.

The theoretical formulation of pump and probe measurements is given by Ippen and Shank (126), which includes both the pure pump and probe response as well as the coherent transient contribution. The intensity modulation $M(\tau)$ of the probe beam, produced by the pump beam, is given by

$$M(\tau)\alpha\gamma(\tau) + \beta(\tau)$$

where the two terms γ and β are:

$$\gamma(\tau)=\int_{-\infty}^{\infty}A(t-t')\int_{-\infty}^{\infty}I_{pr}(t,\tau)I_{pr}(t')dt'dt$$

$$\beta(\tau)=\int_{-\infty}^{\infty}E_{pr}(t,\tau)E_{pr}^{*}(t)\cdot\int_{-\infty}^{\infty}E_{pr}(t')E_{pr}^{*}(t',\tau)A(t-t')dt'dt$$

A(t) is the impulse response of the system to a delta function excitation, I_{pu} and E_{pr} are the intensities of the pump and probe, respectively, E_{pu} and E_{pr} are the electric fields of the pump and probe, respectively, with parallel excitation, and the pump and probe pulses have a relative delay of τ. Assuming that the intensity profiles of the pump and probe can be expressed by sech (127) functions, and the pulse widths of pump and probe are T_{pu} and T_{pr}, respectively, assuming also that excitons and free carriers are the only pump generated processes, which is reasonable for near-bandgap low excess energy pumping, then A(t) will be the sum of the response of the excitons and that of the free carriers, $A(t) = A_{ex}(t) + A_{fc}(t)$, where the individual response functions are given by:

$A_{ex}(t) = \alpha_{ex}N_{ex} = \alpha_{ex}\exp(-t/T)$

and

$A_{fc}(t) = \alpha_{fc}N_{fc} = \alpha_{fc}(1-\exp(-t/T))$

where N_{ex} and N_{fc} are the exciton and free carrier populations, respectively, and α_{ex} and α_{fc} are the respective bleaching strengths of the excitons and free carriers on the exciton resonances, and T is the exciton ionization time. It is assumed that the excitons decay into free carriers with a time constant T, and the free carriers have much longer lifetimes. In this case, the population dynamics can be modelled by the following rate equations:

$$\frac{dN_{ex}}{dt} = G_{ex}(t) - \frac{N_{ex}}{T}$$

and

$$\frac{dN_{e\text{-}h}}{dt} = \frac{N_{ex}}{T}$$

where G_{ex} is the exciton creation rate by the pump beam. By combining all the above equations, pure pump probe response $\gamma(\tau)$ as well as the coherent transient signal $\beta(\tau)$ can be obtained. The results can be plotted and compared with experimental data to determine important parameters like T, α_{ex}, α_{fc}.

Pump-probe experiments can be conducted at either near bandgap excitation or far above bandgap excitation. In the case of near bandgap excitation, carriers have low excess energies, consequently carrier-carrier scattering is the principal thermalization mechanism. In the case of excitation far above the bandgap, carriers have high excess energies, so many competing thermalization processes participate and the situation is more complex. Processes such as carrier-carrier scattering, carrier-phonon scattering, and intervalley scattering all contribute to carrier thermalization, and it is difficult to determine the individual contributions from each process. However, there are still ways of studying individual processes by isolation. For example, Hohenester et al.(5) studied the intervalley scattering by comparing the thermalization processes in GaAs and InP. The two materials have similar optical response behaviors at a 2eV excitation except that carriers in GaAs are excited above the threshold for intervalley transfer while carriers in InP are excited below this threshold. Therefore, qualitative information on the comparable role of intervalley transfers in these materials can be obtained. Based on this knowledge, specific experiments can be designed which can give

quantitative information on the strength of the Γ→L transfer rate in GaAs. This study of CdZnSe/ZnSe MQWs was focused on near resonance excitation pump-probe experiments.

Figure 5-12 illustrates the differential transient absorption experimental setup utilized in this study. The ultrafast pulse train from the optical parametric amplifier (OPA) tuned to the exciton resonance was used as the pump (200fs, 250kHz). The white light continuum from OPA (200fs, 250kHz) was used as the probe. The probe was passed through a motorized variable delay line. Both beams were focused on the same spot of the sample. The transmitted probe beam after the sample was directed into a 320mm spectrometer and detected with a silicon linear diode array. The signal output of the linear diode array was input to an optical multichannel analyzer (OMA). A small portion of the incident probe was split off for reference. The spectral transmission of the sample is obtained by taking the ratio of the transmitted and the reference spectra, which eliminates the effect of spectral structure of the probe beam. The OMA, the delay line and the spectrometer were controlled by a computer, so both absorption temporal and spectral profiles could be scanned automatically. The pump and probe beams are orthogonally polarized to each other to minimize coherent artifacts. For low temperature measurements, the sample was maintained in a close cycle Helium cooled cryostat at 10K. The time resolution of the whole system is about 200fs, the pulse duration of the laser. The zero delay time was determined at the maximum coherent artifact with pump and probe beams parallely polarized to each other. The probe beam was focused to a

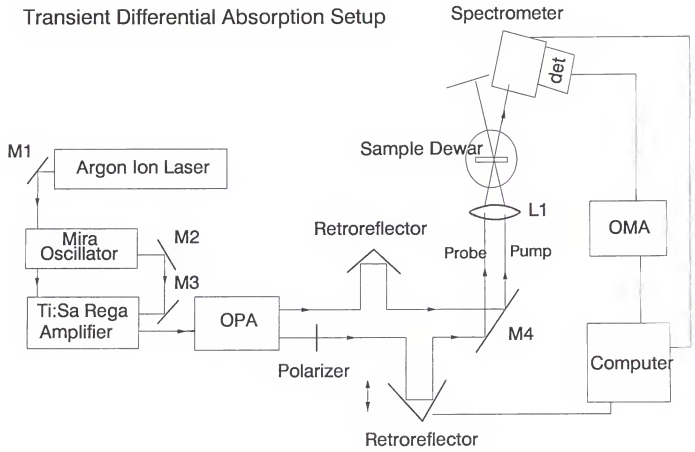

Figure 5-12 Schematic of differential transient absorption experiment.

smaller spot size on the sample than the pump to ensure that the whole probe beam "was contained" in the pump beam. The probe was attenuated to intensities such that there was no self bleaching or other nonlinear effects at the exciton peak.

The DTS technique gives direct information on electron and hole occupation functions thus carrier thermalization dynamics. Also, its experimental setup is relatively simple. As a result, DTS technique is one of the most commonly used techniques in ultrafast spectroscopy.

CHAPTER 6
EXPERIMENTAL RESULTS ON QUANTUM WELLS AND THEORETICAL ANALYSIS

In this chapter, the experimental results from carrier dynamics study of $Cd_xZn_{1-x}Se/ZnSe$ multiple quantum well structures are presented. Detailed theoretical analysis of these data are given and the underlying physics is emphasized.

Quantum Mechanical Calculation of Band States

Electron and Hole States

Electron states

The electronic states of the conduction band in quantum well structures can be calculated quite easily in the approximation of the envelope wave function (128, 129), using a Kane model (130) for describing the electron and hole states of the well and barrier materials. The approximation assumes that the well barrier interface potential is only localized at the interface and the interface potential doesn't mix with the band-edge wavefunctions but only shifts them. The electron wave function takes approximately the form,

$$\Psi = \sum_{w,b} e^{ik_\perp \cdot r} u_{ck}^{A,B}(r)\psi_n(z)$$

where z is the growth direction, $k_\perp$ is the transverse electron wave vector, $u_{ck}(r)$ is the Bloch wavefunction in the well or barrier material, and $\psi_n(z)$ is the envelope

wavefunction, determined to a good approximation by the Schrodinger-like equation (128, 129),

$$\left(-\frac{\hbar^2}{2m^*(z)}\frac{\partial^2}{\partial z^2}+V_c(z)\right)\psi_n(z)=\varepsilon_n\psi_n(z) \qquad (6\text{-}1)$$

where $m^*(z)$ is the electron effective mass of the well or barrier material, $V_c(z)$ represents the energy level of the bottom of the conduction bands, and ϵ_n is the confinement energy of the carriers.

The continuity conditions at the interfaces z=0 and L are

$$\psi_w(k_z,z) = \psi_b(k_z,z)$$

$$\frac{1}{m_w^*}\frac{\partial\psi_w}{\partial z}=\frac{1}{m_b^*}\frac{\partial\psi_b}{\partial z} \qquad (6\text{-}2)$$

where k_z is the wavevector in the plane. Rather than use the continuity condition of the derivative of wavefunction as derived in most quantum mechanics textbooks (131) it is necessary for conservation of particle current to use the continuity of $(1/m^*)(\partial\psi/\partial z)$, since the well and barrier are made from different materials (129, 133).

In the infinite potential well approximation ($V_c=\infty$), the solutions to equation 6-1 are very simple and the wavefunctions and energies are given by

$$\psi_n=A\sin\frac{n\pi z}{L_z}, \qquad E_n=\frac{\hbar^2}{2m}\left(\frac{n\pi}{L_z}\right)^2 \quad n=1,2,3,..... \qquad (6\text{-}3)$$

where L_z is well thickness, A is an arbitrary constant. The electronic energies are quantized due to confinement.

In the case of finite potential barriers, electrons and holes are not totally confined inside the well and their wavefunctions penetrate into the barriers, as depicted in figure 6-1. Taking the center of the well as the center of the coordinate, the solution wavefunctions of equation 6-1 can only be even or odd. They can be written as

$$\psi_n(z) = A\cos kz, \quad \text{for } |z| < L/2$$
$$= B\exp[-k'(z-L/2)], \quad \text{for } z > L/2 \qquad (6\text{-}4)$$
$$= B\exp[+k'(z+L/2)], \quad \text{for } z < -L/2$$

or

$$\psi_n(z) = A\sin kz, \quad \text{for } |z| < L/2$$
$$= B\exp[-k'(z-L/2)], \quad \text{for } z > L/2 \qquad (6\text{-}5)$$
$$= B\exp[+k'(z+L/2)], \quad \text{for } z < -L/2$$

where

$$\mathcal{E}_n = \frac{\hbar^2 k^2}{2m_w^*} - V_0, \qquad \mathcal{E}_n = \frac{\hbar^2 k^2}{2m_b^*}, \qquad -V_0 < \mathcal{E} < 0 \quad (6\text{-}6)$$

For the solution of equation 6-4, the continuity conditions at $z = \pm L/2$ yield

$$A\cos(kL/2) = B, \qquad (k/m_w^*)\sin(kL/2) = k'B/m_b^*$$

therefore,

$$(k/m_w^*)\tan(kL/2) = k'/m_b^* \qquad (6\text{-}7)$$

Similarly, equation 6-5 yields

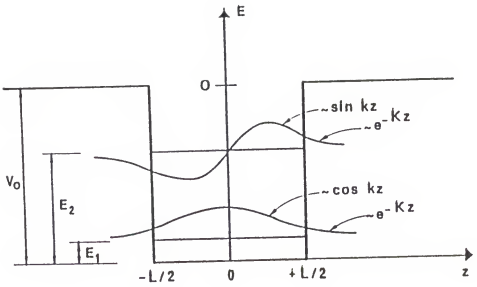

Figure 6-1 First two bound energy levels and wave functions in a finite quantum well. Penetration of wavefunctions into barriers is shown.

$(k/m_w^*)cotan(kL/2)=-k'/m_b^*$ (6-8)

Equations 6-7 and 6-8 can be solved either numerically or graphically. For the case of $m_w^* \approx m_b^*$, a simpler solution can be developed. Using equation 6-6, equations 6-7 and 6-8 can be rewritten in terms of k alone:

$\cos(kL/2)=k/k_0$, for tan kL/2 >0 (6-9)

$\sin(kL/2)=k/k_0$, for tan kL/2 <0 (6-10)

where

$k_0^2=2m^*V_0/\hbar^2$

Hole states

Describing the confinement of holes in semiconductors is not as simple. The bulk hole bands are described in Kane's model by basis equations with angular momentum J=3/2 symmetry, i.e., 4-fold degeneracy at k=0 (neglecting the split-off band). The dispersion near k=0 can be described by the Luttinger Hamiltonian (134). For hole levels in a quantum well, the perturbation from the quantum well potential and that from the k·p, which yields the dispersion, have to be treated on equal footing (135, 136). Thus, the perturbed Hamiltonian given by $H=H_{k\cdot p}+H_{qw}$ will be added to the degenerate valence band levels at k=0. The first-order solutions are linear combinations of k=0 valence-band wavefunctions. Complications arise because of the boundary conditions which have to be satisfied simultaneously for the quantum well as well as for the k·p. The functions which diagonalize $H_{k\cdot p}$ are not a basis set for H_{qw}. Strong mixing of J=±3/2 (heavy-hole) and J=±1/2 (light-hole) is required to satisfy the boundary conditions (133, 137).

The case of holes in an infinitely deep well has been solved analytically (136, 137). Neglecting band warping in the spherical approximation ($\gamma_2=\gamma_3$), the energy levels at k=0 are given by

$$E_{(l,h)n}=n^2\frac{\pi^2\hbar^2}{2m_0L^2}(\gamma_1\pm2\gamma_2) \qquad (6\text{-}11)$$

where γ_1 and γ_2 are Luttinger parameters, and m_0 is the electron rest mass. From equation 6-11, hole band degeneracies at k=0 are lifted due to quantum confinement. For the finite well case, only numerical results were obtained (135). However, the features obtained from the infinite well case are still retained.

Excitons

Excitons are electron-hole pairs coupled by the Coulomb attraction between them. As in the case of the hydrogen atom, this Coulomb attraction leads to bound levels, the lowest of which is one effective Rydberg (Ry^*) below the continuum, and in which the electrons and holes are bound to each other within an effective Bohr radius a_B^*. The effective Rydberg and Bohr radius are given by

$$R_y^*=\frac{2m_{red}e^4}{\hbar^2(8\pi\varepsilon)^2}=\frac{m_{red}}{m_0}\frac{1}{\varepsilon_r^2}Ry, \qquad a_B^*=\frac{4\pi\varepsilon\hbar^2}{m_{red}e^2}=\varepsilon_r\frac{m_0}{m_{red}}a_B \qquad (6\text{-}12)$$

where m_{red} is the reduced mass of electron and hole ($1/m_{red}=1/m_e+1/m_h$); ε_r is the relative permittivity of the semiconductor; R_y=13.6eV; and a_B=0.529Å.

For two dimensional quantum wells, the well thickness is usually in the order of, or smaller than the Bohr diameter $2a_B$, the upper limit of quantum confinement regime. The wavefunctions and energy levels of excitons are quite modified. In the

limit of exact 2D case where $L<<a_B$, the 2D Rydberg value $R_{2D}=4R_{3D}$ for the infinitely deep well (138). The energy levels are given by (139, 140)

$$R_{n,2D}=R_{3D}[1/(n-1/2)^2] \qquad (6\text{-}14)$$

For finite well thickness, exciton binding energies have recently been calculated through a variational method using simple parabolic hole bands (141). The calculated exciton binding energy as a function of well thickness is shown in figure 6-2.

The increase in exciton binding energy has a significant influence on optical properties of quantum wells. Exciton effects dominate nonlinear optical properties of QWs (e.g.GaAs/AlGaAs, CdZnSe/ZnSe QWs) even at room temperature (144). This is rather unique as compared to the bulk semiconductors: usually large exciton binding energies are associated with large reduced masses or bandgaps (142), also to large ionicity (143) and therefore to strong LO-phonon coupling which ionizes excitons at room temperature. A number of interesting properties associated with room temperature excitons in QWs were discussed in detail by Chemla et al. (144)

Cross-Coupling in Superlattices

In the case of finite barriers, electron and hole wavefunctions are not fully confined inside the wells and penetration of the wavefunctions into the barriers takes place. A superlattice structure (or coupled MQWs) consists of many periods of QWs with finite barrier potentials. As the barrier thickness is decreased, the exponentially decaying wavefunction in a barrier from one well can have some finite

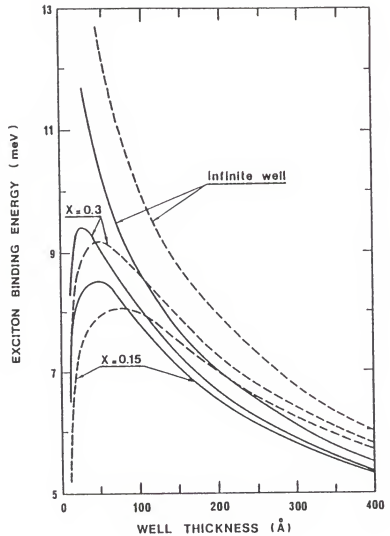

Figure 6-2 Calculated exciton binding energy as a function of well thickness for $GaAs/Al_xGa_{1-x}As$ quantum wells. The solid lines correspond to heavy-hole exciton and dash lines to light-hole exciton. Curves for three well depths are shown: an infinite well; ΔE_v=190meV and ΔE_g=380meV corresponding to x=0.15 and 0.3 respectively (141).

SUPERLATTICES

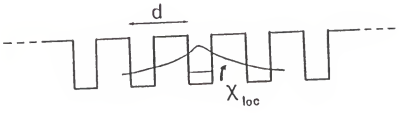

N WELLS

N-DEGENERATE GROUND STATE

TIGHT-BINDING APPROXIMATION

$$\Psi_q(z) = \frac{1}{N^{1/2}} \sum e^{iqnd} \chi_{loc}(z-nd)$$

$$\boxed{E = E_1 + S + 2T\cos qd}$$

$$S = \int \chi_{loc}(z-d) V(z) \chi_{loc}(z-d)\, dz$$

$$T = \int \chi_{loc}(z-d) V(z) \chi_{loc}(z)\, dz$$

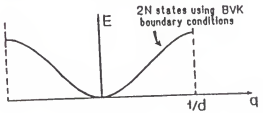

Figure 6-3 Tight-binding model of superlattices (149).

value in the next well. The resulting wavefunction overlap will perturb the original isolated wells, consequently, wavefunctions and energy levels of each well will be altered. The energy-level schemes of coupled MQWs can be calculated by several theoretical techniques, such as Kronig-Penny model (145), perturbative tight-binding model (146), or successive multiple tunneling model (147). Dingle et al. (148) studied the transition from single wells to coupled MQWs by optical absorption. The formation of a continuous band of states (minibands) was observed on coupled MQW structures. The simplest treatment of this is to consider a tight-binding model of the N-well chain (149). (illustrated in figure 6-3) The Bloch-like envelope wave function can be written as

$$\psi_q^{(l)}(z)=\frac{1}{\sqrt{N}}\sum_n e^{iqnd}\psi_{lcc}^{l}(z-nd)$$

where $\chi_{lcc}^{l}(z-nd)$ is the ith wave function of the quantum well centered at z=nd and q is the Bloch wave vector. Assuming only nearest-well interaction, the energy is $\epsilon_i(q)=E_i+s_i+2t_i\cos qd$,

with

$$s_i=\int_{-\infty}^{\infty}\chi_{lcc}^{l}(z-d)V(z)\chi_{lcc}^{l}(z-d)dz$$

$$t_i=\int_{-\infty}^{\infty}\chi_{lcc}^{l}(z)V(z)\chi_{lcc}^{l}(z-d)dz \qquad (6\text{-}15)$$

where s_i and E_i are the unperturbed energies. The last term $2t_i\cos qd$ is the coupling term between wells and yields a bandwidth of $4t_i$.

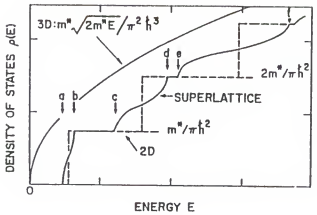

Figure 6-4 Comparison of the density of states of a superlattice with that of the 2D system (----) and a 3D system (from ref. 8).

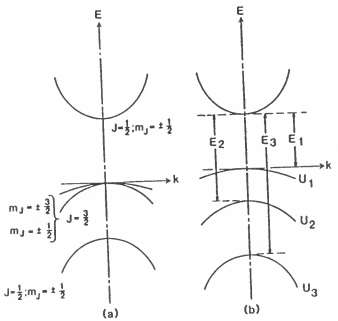

Figure 6-5 Schematic representation of the valence bands and the lowest conduction bands (a) unstrained and (b) strained due to biaxial compressive stress, in zinc-blende-type semiconductors.

The cross-coupling effect causes a profound change in the 2D density of states function. The formation of miniband destroys the steepness of the square density of states as illustrated in figure 6-4.

Strain Effect on Band Edge Offsets (150, 151)

When the thickness of the superlattice layers is well below the critical thickness, the layers assume nearly the same lattice constant as the buffer layer, i.e., any relaxation is negligibly small. The CdZnSe/ZnSe MQW structures under study were grown on GaAs substrates with a 2μm ZnSe buffer layer, consequently, the CdZnSe layers with larger lattice constant than ZnSe are under an in-plane biaxial compressive strain. For the zinc-blende-type material, the valence bands at k=0 consist of a fourfold $p_{3/2}$ multiplet (J=3/2, m_j=±3/2,±1/2) and a twofold $P_{1/2}$ multiplet (J=1/2; m_j=±1/2). For the case of in-plane biaxial compression, the $P_{3/2}$ valence band splits because of lowering the symmetry from T_d to D_{2d}. In addition, the hydrostatic component of the stress shifts the center of the gravity of the $P_{3/2}$ and $P_{1/2}$ multiplets relative to the bottom of the lowest conduction band and affects the effective masses of the multiplets. The fourfold degenerate $P_{3/2}$ splits into a doubly degenerate U_1 band and U_2 band (shown in figure 6-5). The effective mass of the heavy hole U_1 band becomes lighter, while that of the light hole band U_2 becomes heavier. The spin-orbit split-off band is given as U_3. Pikus and Bir (152) have shown that the orbital strain Hamiltonian for a given band at k=0 can be written as

$$H_\varepsilon = -a(\varepsilon_{xx}+\varepsilon_{yy}+\varepsilon_{zz}) - 3b[(L_x^2 - \frac{1}{3}L^2)\varepsilon_{xx} + c.p.] - \sqrt{3}d[(L_xL_y)\varepsilon_{xy} + c.p.],$$

where ε_{ij} denotes the components of the strain tensor, L is the angular momentum operator, c.p. denotes the cyclic permutation with respect to the indices x, y, and z, and (L_x, L_y) indicate the symmetrized product: $1/2\ (L_xL_y + L_yL_x)$. The parameter a is the hydrostatic deformation potential. The quantities b and d are the shear deformation potentials appropriate to the strain of tetragonal and rhombohedral symmetries, respectively. If we define z parallel to the growth direction [001], then the strain tensors ε_{ij}, corresponding to the CdZnSe layers, are given by

$$\varepsilon_{xx} = \varepsilon_{yy} = \left(\frac{a_{ZnSe} - a_{CdZnSe}}{a_{CdZnSe}}\right), \quad \varepsilon_{zz} = -\frac{2C_{12}}{C_{11}}\varepsilon_{xx}, \quad \varepsilon_{xy} = \varepsilon_{yx} = \varepsilon_{zx} = 0$$

where C_{ij}'s are the elastic stiffness constants, a's are the lattice parameters.

The hydrostatic potential a here is the relative hydrostatic pressure constant between the conduction band and the valence band, since we experimentally measure only the energy difference between the two bands. However, it is useful to define hydrostatic potentials a_v and a_c for the valence and conduction bands separately, then $a = a_c - a_v$. It worth noting that the direct conduction band minimum at Γ is only subject to the hydrostatic component of the strain, and not influenced by uniaxial components.

In the case of z parallel to [001] direction, the strain Hamiltonian becomes

$$H_\varepsilon = -2a\left(\frac{C_{11}-C_{12}}{C_{11}}\right)\varepsilon_{xx} - 3b\left(\frac{C_{11}+2C_{12}}{C_{11}}\right)\varepsilon_{xx}\left(L_z^2 - \frac{1}{3}L^2\right)$$

where the first term represents the shift of the center of the gravity of $P_{3/2}$ and the second term describes the splitting of $P_{3/2}$ due to tetragonal distortion. The eigenvalues of the strain Hamiltonian can be calculated by using the unperturbed wave functions of the conduction and valence bands in a zinc-blend type material. The calculated energy difference between conduction and valence bands at k=0 is given by (153)

$\Delta E_1 = E_H + E_U$,

$\Delta E_2 = E_H + 1/2(\Lambda - E_U) - 1/2(9E_U^2 + 2\Lambda E_U + \Lambda^2)^{1/2}$,

$\Delta E_3 = E_H + 1/2(\Lambda - E_U) + 1/2(9E_U^2 + 2\Lambda E_U + \Lambda^2)^{1/2}$,

where

$$E_H = -2a\left(\frac{C_{11}-C_{12}}{C_{11}}\right)\varepsilon_{xx}, \quad E_U = -b\left(\frac{C_{11}+2C_{12}}{C_{11}}\right)\varepsilon_{xx},$$

and Λ is the spin-orbit splitting.

The values of the various deformation potentials can be derived from first-principles calculations, using local-density-functional theory and ab initio pseudopotentials (154). They can also be obtained experimentally: a can be obtained from the hydrostatic pressure dependence of the lowest energy gap using the relation $a = -1/3(C_{11}+2C_{12})\partial E/\partial P$ (155), and b can be obtained from fits to the dispersion of photoelastic constants (156).

In the case of biaxial tension, the reverse shifts occur, i.e., the (J=3/2, m_J=±1/2) branches move to the top of the valence band and the (J=3/2, m_J=±3/2) branches move to lower levels. The overall energy gap decreases.

The band shifts caused by the strain effect in superlattice structures influence the relative band lineups and thus the band discontinuities between the two materials. As a result, the degree of quantum confinement and electronic or hole states for the structures will be altered. It will be shown in the next section that strain effects can be responsible for almost entire valence band offsets in CdZnSe/ZnSe MQW structures. Strained layers are normally considered to be undesirable since they are in metastable states, however, strain effect can induce unique electronic properties which are very beneficial in many applications. For example, diode lasers fabricated from strained semiconductor superlattice structures have demonstrated much higher gain and lower threshold current compared to the devices fabricated from the unstrained ones due to the increased oscillator strength induced by the strain (157, 158).

Band Structure Calculation of ZnCdSe/ZnSe Multiple Quantum Well Structures

One important step in this study is the calculation of band structures of the material heterostructure system based on which experimental data can be interpreted and understood properly. The schematic diagram of the band structure of the MQW system is shown in figure 6-6. This MQW system is classified as type I superlattices since both electrons and holes are spatially confined in the well material, whereas in the case of type II superlattices electrons and holes are

confined in well and barrier materials separately. Since the well material CdZnSe has a larger lattice parameter than the barrier material ZnSe, the well material is under an in-plane biaxial compressive strain. The calculation was based on the quantum mechanics formalism outlined in the previous sections. The electronic band structure was calculated by solving the Schrodinger equations with wavefunction and space charge continuity across the well-barrier interface. The hole states are calculated using spherical approximation neglecting band warping and applying the first order perturbation hamiltonian. The effect of biaxial compressive strain was included in the electronic and holes band offsets. The cross-coupling effect between wells was included in a separate perturbation matrix element. The electron and hole states are given by the numerical solutions to the following dispersion relations: (159)

$$\cos(kl)=\cos(k_z l_z)\cosh(k_b l_b)+\frac{1}{2}\left(x-\frac{1}{x}\right)\sin(k_z l_z)\sinh(k_b l_b)$$

where l is the superlattice period and l_z and l_b are well and barrier widths and

$$x=\left(\frac{k_b m_z}{k_z m_b}\right),$$

$\hbar k_z=(2m_z E)^{1/2}$, $\hbar k_b=[2m_b(V-E)]^{1/2}$,

where m_z and m_b are the effective masses in the well and barrier layers and V is the potential barrier height corresponding to valence or conduction-band offsets. Note that in the above equation x is an explicit function of m_z and m_b.

The material parameters used in the band structure calculation were taken from Landolt-Bornstein New Series III/22a (160) and are listed in table 6-1. The listed parameters of the CdZnSe ternary compound were obtained by linear interpolation of the corresponding parameters of the composing binary compounds. The calculated results for T=10K are outlined in table 6-2. Although a more rigorous calculation including the valence band nonparabolicity and heavy and light hole band mixing can give more accurate results, such a calculation requires a tremendous amount of computer memory and is difficult to put into practice. It will be shown in later sections that the current calculation results are in good agreement with the experimental data and are sufficient to explain the fundamental processes involved. It is worth noting that the determined conduction and valence band offsets are very close to those reported in the literature for similar material systems obtained by spectroscopic techniques (161, 162). The heavy-hole exciton binding energy of about 40meV agrees with those reported recently in the literature (80, 163).

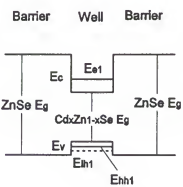

Figure 6-6 Simplified band diagram of $Cd_xZn_{1-x}Se$/ZnSe QWs

Table 6-1
Parameters used in the calculation of band states (10K)

parameter	symbol	ZnSe	CdSe	$Cd_xZn_{1-x}Se$	
				x=0.25	x=0.2
electron eff. mass	m_e^*	$0.16m_0$	$0.13m_0$	$0.153m_0$	$0.154m_0$
heavy hole eff. mass	m_{hh}^*	$0.72m_0$	$0.49m_0$	$0.663m_0$	$0.674m_0$
dielectric constant	ϵ_r	9.1	9.3	9.15	9.14
electron affinity(eV)	χ	4.09	4.95	4.305	4.262
energy gap (10K)	E_g	2.793	1.85	2.557	2.6
elastic moduli($10^{10}Nm^{-2}$)	c_{11}	8.1	7.49	7.948	7.98
	c_{12}	4.88	4.609	4.81	4.826
deformormation potential (eV)	a	-5.4		-5.4	-5.4
	b	-1.2		-1.2	-1.2
lattice parameter(Å)	a_{latt}	5.6676	6.052	5.7637	5.7445
Luttinger parameter(10K)	γ_1	4.3		4.3	4.3
	γ_2	1.14		1.14	1.14
	γ_3	1.84		1.84	1.84

*Note: Blank entries indicate that the data for CdSe (cubic) are not available in the literature. In that case, those parameters of the ternary QWs are taken to be the same as those of ZnSe.

Table 6-2
Calculation Results (10K)
for CdZnSe/ZnSe Multiple Quantum Well Samples (L_z/L_bÅ)

parameters	calculated results for $Cd_xZn_{1-x}Se$/ZnSe MQW samples					
	x=0.2					x=0.25
	50/50	50/200	50/100	100/100	25/100	50/200
ΔE_c (meV)	172	172	172	172	172	215
ΔE_v (meV)	52	52	52	52	52	60
E_{hh} (eV)	2.552	2.561	2.558	2.547	2.654	2.495
E_{ghh} (eV)	2.591	2.602	2.598	2.573	2.699	2.536
B_{hh} (meV)	39	40.6	40.3	25.8	45	40.8
E_{lh} (eV)	2.627	2.636	2.633	2.622	2.729	2.573
a_B (Å)	42	42	42	42	42	44

Symbol Notations:

ΔE_c---conduction band offset or discontinuity
ΔE_v---valence band offset or discontinuity
E_{hh} ---heavy-hole exciton transition energy
E_{ghh} –heavy-hole energy gap, also called electron to heavy hole absorption continuum
B_{hh}--- heavy-hole exciton binding energy ($B_{hh}=E_{ghh}-E_{hh}$)
E_{lh}--- light-hole exciton transition energy
a_B --- CdZnSe ternary compound Bohr radius

The validity of the calculation results was verified by comparison to experimentally obtained absorption spectrum at 10K of a $Cd_xZn_{1-x}Se/ZnSe$ (x=0.25) MQW sample grown homoepitaxially on a ZnSe single crystal substrate. Since ZnSe has a bandgap larger than that of the CdZnSe quantum wells, it is transparent over the region of absorption of the quantum wells. Consequently, absorption experiments can be conducted without the need for removing the substrate. Figure 6-7 shows the absorption spectrum of the sample at 10K. The whole spectrum was sitting on the top of the ZnSe band edge and exciton absorption tail. There are several distinct features present in the spectrum: heavy-hole (hh) exciton transition E_{hh} at 2.49eV, electron to heavy-hole absorption continuum E_{ghh} at 2.636eV, light-hole (lh) exciton transition E_{lh} at 2.567eV, and n=2 transition of hh exciton. Comparing these experimental values with the calculated positions of the hh exciton transition E_{hh}, hh energy gap E_{ghh}, and lh exciton transition E_{lh} in table 6-2, we found excellent agreement between data and calculations. The calculated hh exciton binding energy of 40meV is also confirmed from the spectrum (energy separation between E_{hh} and E_{ghh}). The success of band state calculation on the MQW system offers a solid proof that the quantum mechanical models and parameters utilized are indeed valid. Although more elaborate treatment (taking into account valence bands mixing and non-parabolicity) would provide more physical insights, current results are sufficient enough to interpret experimental results.

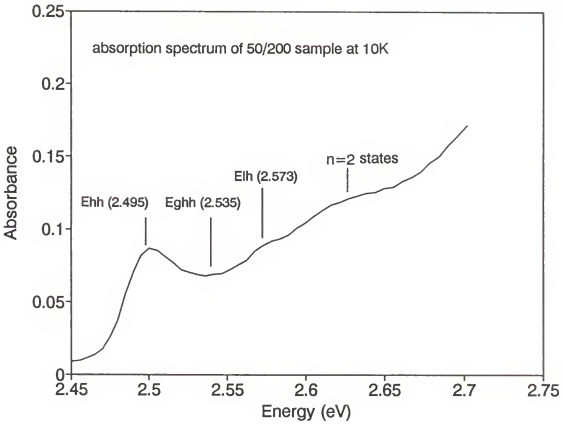

Figure 6-7 Absorption spectrum of 50/200Å $Cd_{0.25}Zn_{0.75}Se/ZnSe$ MQW sample at 10K.

For room temperature band states calculation, the procedure is exactly the same except for changing all the parameters to room temperature values (298K) (mainly energy gaps of the two materials). The results are listed in table 6-3.

Table 6-3
Calculation Results of Band States of CdZnSe/ZnSe MQWs
at Room Temperature

parameters	calculated results for $Cd_xZn_{1-x}Se$/ZnSe MQW samples					
	x=0.2					x=0.25
	50/50	50/200	50/100	100/100	25/100	50/200
E_{hh} (eV)	2.451	2.47	2.463	2.448	2.56	2.39
E_{ohh} (eV)	2.49	2.511	2.503	2.474	2.605	2.431
B_{hh} (meV)	39	40.6	40.3	25.8	45	40.8
a_B (Å)	42	42	42	42	42	44

Room Temperature Experimental Results

One distinct feature of II-VI semiconductors is the strong coupling of electronic band states with LO phonons through the Frohlich interaction due to their large ionicity. Inelastic scattering of excitons by LO phonons into free electron-hole pair continuum is the primary reason for the lack of exciton features in absorption in bulk ZnSe above cryogenic temperatures (E_x for bulk ZnSe is about 18meV). In striking contrast to bulk ZnSe, CdZnSe/ZnSe quantum wells have a very large exciton binding energy about 40meV (as shown in the previous section), exceeding the LO phonon energy $\hbar\omega_{LO}$=31meV, so the dissociation of excitons into free

electron hole pairs by LO phonon scattering is much weakened. Strong and distinct exciton absorption features can be seen in these MQWs beyond room temperature (164). Consequently, room temperature carrier dynamics in these QWs are dominated by exciton dynamics. However, processes such as LO phonon scattering, impurity scattering, and deep-level trapping all can possibly contribute to the overall exciton dynamics and linewidth at room temperature. In such a situation, the exciton transition is characterized by a rather wide emission linewidth.

Both steady-state photoluminescence and time-resolved photoluminescence experiments were conducted on these samples at room temperature. Second harmonic from the amplified Ti:Sapphire regenerative amplifier system (@400nm, 280fs autocorrelation, 250KHz) was used as the excitation source. The population mixing technique was used to measure carrier lifetime and the experimental setup has been described previously in Chapter 5. For steady-state experiment, the same experimental setup was used, except that the dual frequency chopper and lock-in amplifier were not used. The excitation density was chosen to be in the order of 160μJ/cm^2 at the sample, which corresponds to a photoexcited carrier density of 10^{14}cm^{-2}, assuming an absorption coefficient of 10^5cm^{-1} (i.e., an absorption length of 0.1μm) (165). This excited carrier density level is very close to the carrier density level at which normal devices operate at room temperature(166), so the carrier dynamics result will also provide some insights into device operating characteristics.

The samples are divided into two groups: one group consists of three samples with the same barrier thickness and different well thickness, and the other group consists of three samples with the same well thickness but different barrier thickness. The first group (25/100Å, 50/100Å, 100/100Å samples) allows the study of the role of well thickness on exciton dynamics, while the second group (50/50Å, 50/100Å, 50/200Å samples) allows the study of the role of barrier thickness on exciton dynamics. Figures 6-8 and 6-9 show the steady state PL and transient PL results for the first group, and figures 6-10 and 6-11 show the steady-state and transient results for the second group. Table 6-4 summarizes the experimental results from these figures. The measured exciton lifetimes from 80ps to 1.6ns are consistent with the excitonic model, while estimates on the free electron-hole pair recombination in the effective mass approximation suggest a much slower radiative decay (167). The data are also consistent with exciton lifetimes reported in the literature for similar structures (168).

C Quantum Mechanical Analysis On Room Temperature Results

The Role of Barrier Thickness

First, a comparison of the PL intensity and peak position in figure 6-8 gives us the information on carrier localization or confinement, since the emission intensity is characterized by the oscillator strength, which is given by

$$f \propto \frac{2m\omega}{\hbar} |\langle e|\eta \cdot r|p\rangle|^2$$

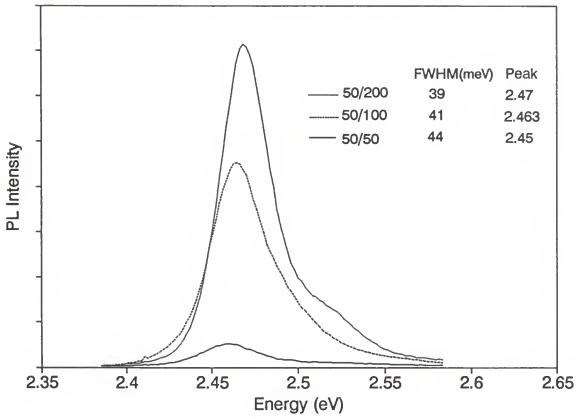

Figure 6-8 Room temperature PL spectra of the first group of samples (50/50Å, 50/100Å, 50/200Å).

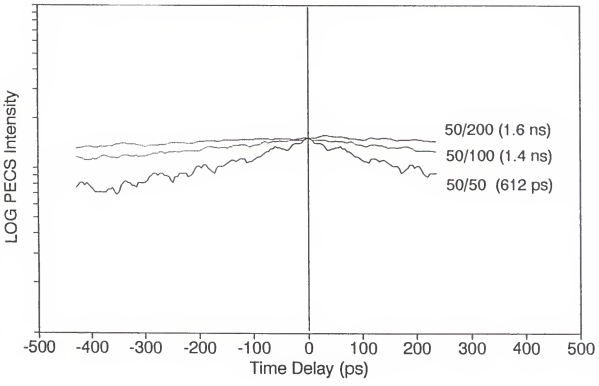

Figure 6-9 Time-resolved PL spectra (PECS) of the first group of samples at exciton transition at room temperature.

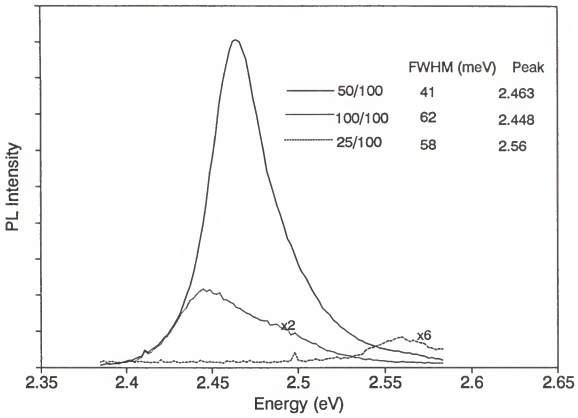

Figure 6-10 Room temperature PL spectra of the second group of samples (25/100Å, 50/100Å, 100/100Å).

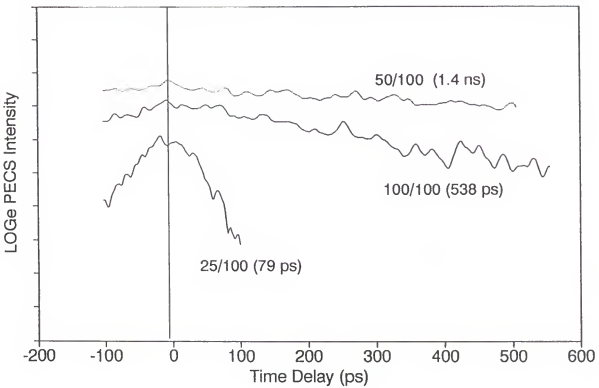

Figure 6-11 Time-resolved PL spectra of the second group of samples at exciton transition at room temperature.

where e and p denote the electron and hole states, and $\eta \cdot r$ is the interaction Hamiltonian.

Table 6-4
Summary of Room Temperature Experimental Results of MQWs

sample	peak position (eV)	FWHM (meV)	exciton lifetime (ps)	PL intensity
50/50Å	2.45	44	612	low
50/100Å	2.463	41	1400	higher
50/200Å	2.47	39	1600	highest
25/100Å	2.56	41	79	weak
50/100Å	2.463	41	1400	strongest
100/100Å	2.448	62	538	stronger

If the electron and hole pairs are more localized, their wavefunctions will have enhanced overlapping. Consequently, a strong coupling interaction between wavefunctions occurs and the oscillator strength is much more enhanced. In quantum well structures, electron and hole wavefunctions are confined within the Bohr diameter and are thus strongly coupled. As a result, quantum wells have stronger oscillator strength and larger exciton binding energy as compared to their bulk counterparts. To first approximation that these three samples should have the same oscillator strengths since each sample has the same well thickness. However, this is not reflected from the data. As shown in figure 6-8, the 50/200Å sample has the highest emission intensity thus the highest oscillator strength, followed by the 50/100Å and the 50/50Å samples. Since the only difference between these three

samples is the barrier thickness, the barrier thickness undoubtly plays an important role. We explain the steady state results in terms of cross-coupling effect present in all our MQW samples, since the conduction and valence band offsets are relatively shallow (as shown in table 6-2). The cross-coupling effect induces an interaction between wavefunctions among individual wells (mainly adjacent wells) and leads to the formation of minibands. The whole structure moves to a more bulk-like behavior. As a consequence, the oscillator strength which is determined by the electron-hole states interaction is reduced compared to the isolated well case. The theoretical treatment of cross-coupling was outlined in the previous section "cross-coupling in superlattices". The superlattice bandwidth calculated from a tight-binding model was given by Equation (6-15)

$$t_r \int_{-\infty}^{\infty} \chi_{loc}^{l}(z) V(z) \chi_{loc}^{l}(z-d) dz$$

where $\chi_{loc}^{l}(z-nd)$ is the ith wave function of the quantum well centered at z=nd and V(z) is the barrier height, and $4t_l$ is the bandwidth. Figure 6-12 shows the calculated superlattice bandwidths of GaAs/GaAlAs superlattices versus different barrier thicknesses by Bastard (149). The three curves on the graph are for different well thickness, and all shows decreasing bandwidth with increasing barrier thickness. It also worths noting that with decreasing well thickness, the influence of barrier thickness on cross-coupling become much more pronounced.

Apply the above theory to our samples, 50/200Å sample is expected to have smallest bandwidth, 50/100Å is the next, followed by 50/50Å sample. This is exactly

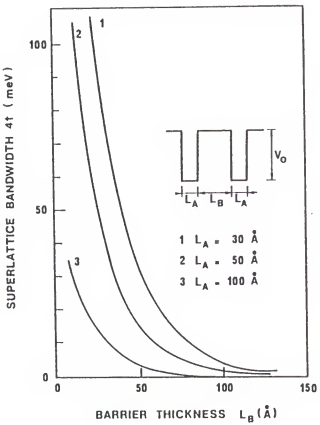

Figure 6-12 Calculated GaAs/GaAlAs superlattice bandwidth as a function of barrier thickness for three different well thicknesses by tight-binding model. x=0.2; V_0=212meV (149)

what is observed as shown in the insert of the figure. Consequently, the 50/200Å sample is least bulk-like and has the highest oscillator strength thus the highest emission intensity. The PL peak positions of the three samples is another proof of the above conclusion. As shown in the insert, the 50/200Å sample has the highest peak energy thus the strongest confinement or oscillator strength, 50/100Å is the next, and the 50/50Å sample exhibits the weakest oscillator strength.

Next, the exciton decay lifetime comparison in figure 6-9 shows that the 50/200Å sample has the longest lifetime, followed by 50/100Å sample, and then 50/50Å sample. This is not expected, since the strongest coupling of electron hole wavefunctions in 50/200 MQWs should shorten the exciton recombination lifetime, as contained in Fermi's golden rule

$$W=\frac{2\pi}{\hbar}\sum_{i,f}|\langle f|H_I|i\rangle|^2\delta(E_f-E_i-\hbar\omega)$$

where i, f are transition initial and final states with energies E_i and E_f, respectively, H_I is the interaction Hamiltonian, which is -er•E in the electric dipole approximation. The summation over initial and final states introduces reduced density of states for QWs. For the 50/200Å sample, H_I should be larger, and the transition rate is expected to be faster with other parameters being close to the other two samples.

We resolved this discrepancy by taking into account the effect of carrier escape from wells into the barriers. The decay time of exciton we measured experimentally contains contributions from all possible processes during the interband transition, i.e. $1/\tau_{tot}=\Sigma\, 1/\tau_i$. For all three samples, there are mainly two

parallel processes which are different among them due to the difference in barrier thickness: exciton decay through direct interband recombination, and carrier escape from well into barrier without recombination inside the well. Then, the total exciton lifetime is determined by the overall contributions from these two parallel processes, i.e. $1/\tau_{tot} = 1/\tau_{rec} + 1/\tau_{esc}$, where τ_{rec} denotes the direct recombination lifetime in the well, and τ_{esc} denotes the carrier escape time into the barriers. For 50/200Å sample, τ_{rec} is the fastest due to the strongest overlapping of electron and hole wavefunctions. However, τ_{esc} is the slowest since this sample has the narrowest miniband bandwidth and weakest cross-coupling interaction among wells. As a result, the overall exciton decay lifetime is a balance between these two counter acting components. It has been demonstrated experimentally by several research groups that carrier escape time is much faster than interband recombination time in QW structures and increases exponentially with increasing barrier thickness (89-96, 169), so we expect that τ_{esc} term should be more dominant in our samples if same principle applies. In that case, τ_{tot} for 50/200Å samples will the longest, that of 50/100Å sample will be the next, and that of 50/50 sample will be the shortest. This is exactly what we observed from our decay lifetime data. Based on the above discussion, we conclude that carrier escape out of well (also called tunneling) plays a dominant role over direct interband recombination in exciton decay dynamics. This conclusion was further verified by experimentally measuring carrier escape times for the same three samples at low temperature

(10K). As will be shown in low temperature result section, 50/200Å sample has the slowest carrier escape time and 50/50Å sample has the shortest, which indeed supports our conclusion.

The Role of Well Thickness

Figure 6-10 shows the steady-state PL results from the second group of sample with different well thickness but same barrier thickness. The emission intensity comparison is evident. The 50/100Å sample has the highest emission intensity, 100/100Å sample comes next, and 25/100Å sample shows the weakest intensity. As discussed previously, PL intensity is determined by the oscillator strength of the transition. With decreasing well thickness, electron and hole wavefunctions are more confined, consequently, the oscillator strength is much more enhanced and stronger PL intensity is expected. The 50/100Å sample and 100/100Å sample follow this trend, however, the 25/100Å sample shows the weakest intensity rather than the strongest. The weak PL intensity of 25/100 sample can also be explained in terms of penetration of electron and hole wavefunctions into the barrier material. Due to its very thin well thickness (25Å$\approx a_B/2$), the electrons and holes are highly confined to very high energy levels inside the well. Since the potential barrier heights or band offsets are finite and shallow for the multiple quantum well structures, carrier penetration into the barrier material increases dramatically when the carrier energy level approaches the potential barrier height. This is evident from the following basic quantum mechanical equation

$$\Delta x \sim \frac{\hbar}{\sqrt{2m(V_0-E)}}$$

where Δx is the penetration distance, V_0 is the barrier height, E is the energy level of carriers.

As a consequence, the excitons tend toward to the 3D exciton of the barrier material and only a fraction of total number of excitons participates in the recombination process in the well region. Since photoluminescence intensity is the product of the transition oscillator strength and the number of transitions, we expect reduced PL intensity due to the reduced number of transitions although the oscillator strength is high. As evidenced by the calculated results shown in table 6-3, the 25/100Å sample has much larger exciton transition energy as compared to other samples with wider well thickness. The n=1 electron state for this sample is only 40meV ($E_{g(ZnSe)}-E_{gHH}-\Delta E_v \approx 40meV$) below the potential barrier, so the penetration of electron wavefunction into ZnSe barrier is indeed significant. The strong confinement of electron-hole pairs is reflected from the data shown in figure 6-10. The PL peak position of 25/100Å sample is blue shifted from the other two samples by a very large amount in energy. The peak position of the 50/100Å sample is at higher energy than that of the 100/100Å sample, indicating the stronger carrier confinement or oscillator strength present in 50/100Å than in 100/100Å sample. All the peak positions from the data agree well with the calculated values in table 6-3.

The phenomenon of carrier penetration into barrier material in very thin

quantum wells with finite barriers was discussed in detail by Schmitt-Rink et al. (170). The exciton binding energy versus well thickness in GaAs/AlGaAs MQWs was calculated by Greene et al.(171, 172) using variational method and is shown in figure 6-13. The curves for the infinite well show a monotonic increase as $L_z \to 0$; conversely, the curves for finite well depth go through a maximum and then decrease indicating the dominance of penetration effect when the wells are too thin.

Figure 6-11 shows the exciton decay lifetime results for the three sample. The 50/100Å sample exhibits the longest lifetime, 100/100Å sample is in the middle, and 25/100Å sample exhibits the shortest lifetime. From our conclusion with the decay lifetime analysis of the other three samples with same well thickness, we know that carrier escape into the barrier plays an dominant role over direct exciton interband recombination on the overall exciton decay behavior. We are interested to see if same principle applies to these three samples also. In 25/100Å sample, carrier escape τ_{esc} is extremely significant compared to the other two samples due to very small (V_0-E). On the other hand, the strong transition oscillator strength due to its very narrow well width shortens the exciton recombination lifetime τ_{rec}. Consequently, overall exciton lifetime τ_{tot} ($1/\tau_{tot} = 1/\tau_{esc} + 1/\tau_{rec}$) of this sample is expected to be very short. Compared to 25/100Å sample, the 50/100Å and 100/100Å samples are much less confined (i.e. longer τ_{rec}) and the carrier escape is less significant(i.e. longer τ_{esc}), so the overall exciton lifetimes of these two

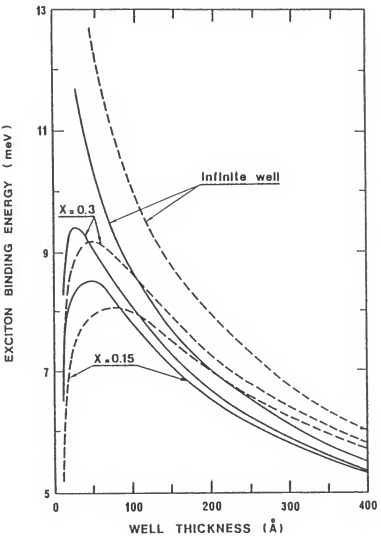

Figure 6-13 Calculated exciton binding energy as a function of well thickness for $GaAs/Al_xGa_{1-x}As$ quantum wells. The solid lines correspond to heavy-hole exciton and dash lines to light-hole exciton. Curves for three well depths are shown: an infinite well; ΔE_v=190meV and ΔE_0=380meV corresponding to x=0.15 and 0.3 respectively (141).

samples τ_{tot} are expected to be much longer. The data in figure 6-11 indeed show the predicted behavior.

Compare the 50/100Å sample with the 100/100Å sample, 50/100Å has narrower well thickness and thus carriers are more confined (i.e. shorter τ_{rec}). The 50/100Å sample is also expected to have shorter τ_{esc}, since electronic states are at higher energy level and carrier escape out of well (or tunneling) is stronger (small ΔE_c-E). However, this prediction is proved to be incorrect. As shown figure 6-10, the 100/100Å sample exhibits much wider transition luminescence bandwidth compared to 50/100Å sample, which means that cross-coupling effect is stronger in 100/100Å sample rather than in 50/100Å sample. Closer examination of 100/100Å sample enable us to solve this dilemma. Since the well thickness of 100Å is larger than Bohr diameter ($2a_B$=84Å), the carriers in this sample is nearly unconfined and the density of states is close to continuous bulk-like. In this situation, carrier escape is much more probable because tunneling can always occur at near resonance. This explains why cross-coupling is much stronger in 100/100Å sample. Because of the weak oscillator strength, the exciton recombination lifetime τ_{rec} is much longer. If taking into consideration the fact that this sample has faster τ_{esc}, the overall exciton lifetime will be faster if τ_{esc} is dominant over τ_{rec}. The experimental data are thus reasonably well explained. A strong evidence of strong tunneling effect in this sample is its rather wide FWHM exciton bandwidth as compared to 50/100Å sample

(62meV versus 41meV) as shown in the insert of Fig.6-10. The dominant role of carrier escape on exciton decay was also confirmed in these three samples.

To summarize the room temperature results, we found that carrier escape from the wells plays a more important role over direct interband recombination on overall exciton decay dynamics. For the samples with same well thickness but different barrier thickness (50/50Å, 50/100Å, 50/200Å), oscillator strength and exciton decay lifetime increase with increasing barrier thickness. The 50/200Å sample has a measured exciton lifetime of 1.6ns at transition energy of 2.47eV. For samples with same barrier thickness but different quantum well thickness (25/100Å, 50/100Å, 100/100Å), exciton decay lifetime was found to be extremely fast and exciton PL intensity was found to be very weak for sample with very thin well thickness ($L_z \approx a_B/2$) due to significant carrier penetration into barriers. The sample with well thickness above Bohr diameter (L_z=100Å>$2a_B$) was found to behave nearly bulk-like with fast exciton decay time and broad, relatively weak luminescence intensity. The 50Å sample was found to be the optimum of these three. It has a well thickness narrow enough to quantum confine carriers but not too narrow to allow significant carrier penetration to occur. The exciton decay lifetime of 50/100Å sample was found to be 1.4ns at transition energy of 2.464eV. Combine the results from the two groups of samples, 50/200Å sample seems to be the optimum structure for diode laser and LED applications. Although even thicker barrier may result in longer lifetime, this structure is already close to the optimum, since the difference in lifetime and transition intensity between this sample and 50/100Å

sample is much smaller compared to that between 50/100Å and 50/50Å samples.

Low Temperature Results: Exciton And Biexciton Dynamics

At low temperature, inelastic scattering of carriers by optical phonons is significantly reduced. The luminescence spectrum is characterized by emission lines with much higher intensities and narrower linewidths as compared to those at room temperature. Also different emission bands are separated due to reduced bandwidths and different processes associated with these emission bands can be identified by their characteristic energy positions. Low temperature luminescence technique has proved to be a very valuable technique to gain insights into the quality of the material as well as physical processes occurring in the material. The bulk semiconductor luminescence spectrum typically consists of various impurity-bound excitons, free excitons, donor-acceptor transitions, and deep level transitions. From the positions of each emission line, the impurity or dopant species present in the sample can be identified. In contrast, the luminescence spectrum of quantum well structures typically consists of free excitons, excitonic complexes, excited states of exciton and excitonic complexes, and deep-levels. The impurity-bound excitons are very difficult to observe in quantum wells due to the fact that the oscillator strength associated with bound excitons is very weak as compared to that of free exciton and exciton complexes in the quantum confined regime. Theoretical calculation by Herbert and Rorison (173) have shown that, where as confinement increases free-exciton oscillator strength as $1/L_z$, it slightly decreases that of bound excitons due to the decrease in carrier correlation. The dominance of free exciton

over bound exciton recombination in quantum wells was also verified experimentally by Weisbuch et al. (174) through spin-memory experiments under circularly polarized excitation light, which ascertains the symmetry of luminescent state as that of a correlated single electron and single hole, and also through the dependence of the high energy slope of the line on temperature and excitation intensity which indicates the free-moving nature of the exciton. In real quantum wells, the selection rule ($\Delta k=0$) governing the exciton transition is partially lifted because the wavefunctions are not exactly orthogonal in the presence of finite well depth, so the exciton luminescence should be even more efficient.

The low temperature experiments were conducted using the same experimental setup as that at room temperature, except the sample is mounted inside a close-cycle, helium-cooled cold chamber with temperature maintained at 10K. The beams were focused to a 0.5mm spot size on the sample. Different levels of excitation intensities, corresponding to excited carrier densities from 10^{15} to $10^{13}/cm^3$ were used in the experiment to study various processes associated with high carrier densities.

Analysis On Low Temperature Data

Observation of Biexcitons

Excitons are formed by electron and hole pairs bound together by Coulomb interaction. In the limit of low nonequilibrium density, the exciton gas can be considered as weak interacting Boltzmann gas. Lampert (175) first suggested that

in a high nonequilibrium electron-hole gas, free multiparticle complexes more complicated than the exciton can exist, namely, neutral excitonic molecules (bound states of two excitons, often called biexcitons). The stability of biexciton complexes was later confirmed by reliable variational calculations (176, 177). Since the introductory work by Lampert, many attempts have been made to observe these multiparticle complexes by spectroscopic techniques. The progress in experimental investigation of biexcitons became more evident during the past few years as more powerful excitation sources and more sophisticated detection techniques became available. Biexcitons have been observed in bulk semiconductors, such as CdS, CdSe, ZnSe, GaAs (178, 179), as well as quantum well structures, such as GaAs/AlGaAs, GaAs/AlAs (180-184). The biexciton binding energies were measured to be in the range of 1-10meV for these materials.

The recombination process of a biexciton involves the emission of a photo $h\upsilon_B$, leaving behind a free exciton. The energy conservation of this decay process gives (185)

$$h\upsilon_B=E_g-E_x-E_B+E_B^k-E_x^k, \qquad (6\text{-}16)$$

where E_g is the energy gap, E_x is the binding energy of the exciton, E_B is the binding energy of the biexciton, and E_B^k and E_x^k are the kinetic energies of the initial biexciton and resulting exciton, respectively. E_B^k can be considered to be negligible at very low temperatures, and E_x^k then should also be small due to momentum conservation. Both terms account for the lineshape of the biexciton transition.

Biexcitons have several unique characteristics that distinguish them from excitons and other multiparticle complexes. First, the presence of biexcitons is indicated by a second PL line at an energy below that of the exciton line corresponding to the binding energy of the two-particle state, as evident from energy conservation equation of the process. The biexciton line is further characterized by a superlinear PL intensity dependence on excitation density and a lifetime that should be shorter than that of the free exciton due to the fact that the biexciton density is proportional to the square of the free exciton density in quasi-equilibrium (x+x↔B). In contrast, the exciton line is characterized by a linear PL intensity dependence on excitation intensity.

Second, the biexciton line in PL in direct-gap semiconductors is distinguished by a reverse Boltzmann-like lineshape due to the recombination kinetics involved (186): the remaining exciton must recoil with sufficient energy to maintain the initial crystal momentum of the biexciton. Thus, hot biexcitons, i.e., those with large initial kinetic energy, result in luminescence to lower energy than do those with small initial biexciton kinetic energy. This feature was verified experimentally through time-resolved PL by Charbonneu et al. in GaAs (179): At shorter times the excitons and biexcitons are very hot and the peaks of regular and reverse Boltzmann distributions are far apart. As the distributions cool with increasing time delay after the laser pulse, the peak of the exciton distribution moves to lower energy while the peak of the biexciton distribution moves to higher

energy, exactly as expected for the temperature dependence of the reverse-Boltzmann-like distribution characteristic of biexcitons.

Third, the biexciton transition is a two-photon absorption process (from a no-exciton ground state). The biexciton transition can be described by a 4-level system (shown in figure 6-14) consisting a ground state $|g\rangle$, two single exciton states $|e_+\rangle$ and the $|e_-\rangle$ representing an exciton excited either by σ^+ or σ^- light, and a two exciton states $|2e\rangle=|e_+\rangle|e_-\rangle$ (both the $|e_+\rangle$ and $|e_-\rangle$ are excited) (187). The Coulombic interaction of the σ^+ and σ^- excitons with opposite spins result in the formation of a biexciton state which is lowered by the biexciton binding energy (Δ) with respect to the corresponding two-exciton scattering state. Calculations based on the resulting 5-level system have been used successfully to interpret results from time-resolved DFWM experiments and pump-probe experiments (187, 188, 189). Thus, the biexciton transition is strongly polarization dependent: it is probable when two beams are cross circularly polarized while it is not probable when two beams are co-circularly polarized.

Finally, very fast biexciton lifetimes and large biexciton binding energies observed experimentally couldn't be explained in terms of classical theories of biexcitons which neglected the effect of polaritons completely (190, 191). A recent self-consistent theory of biexcitons by Haug et al. (192, 193) takes into consideration the influence of polariton effects on the internal structure of the biexciton, and predicts a much faster biexciton lifetime and larger biexciton binding

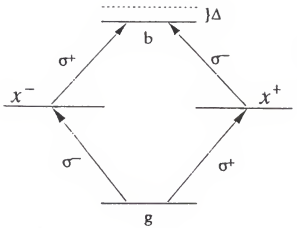

Figure 6-14 The four-level system consisting of a ground state g, two-exciton states $x^{\pm}$, and a biexciton state b with a binding energy Δ.

energy in quantum confined structures. Excellent agreement with experimental data was achieved by the theory.

Although there have been numerous reports of observation of biexcitons in GaAs QWs, there has not been any report on observation of biexcitons in ZnSe based QWs until very recently. Compared to GaAs based QWs, II-VI QWs have much larger biexciton binding energy which makes the observation of biexcitons less difficult. We will show evidences of biexciton formations in our CdZnSe/ZnSe MQW samples in the following paragraphs.

Figures 6-15 and 6-16 show 10K steady-state PL spectra for the two groups of samples. Two distinct emission features common to all samples are evident from the spectra. We attribute the higher energy peak to an exciton transition, and the lower energy peak to a biexciton transition. In order to confirm the assignments, we conducted three experiments.

The first experiment was to verify the superlinear PL intensity dependence of biexciton on excitation power density. A series of PL spectra were taken on the 50/100Å sample with different excitation densities and were plotted in figure 6-17. All spectra were normalized at the exciton peak and the small offsets are for clarity. It is evident that biexciton intensity increases much faster than that of the exciton with increasing excitation intensity. Assuming simple Gaussian lineshapes for the two peaks, the integrated areas of the two peaks below each curve were calculated and the biexciton intensity was plotted vs excitation power density in logarithmic scale as shown in the insert of the figure. A linear fit to the curve yields a slope of

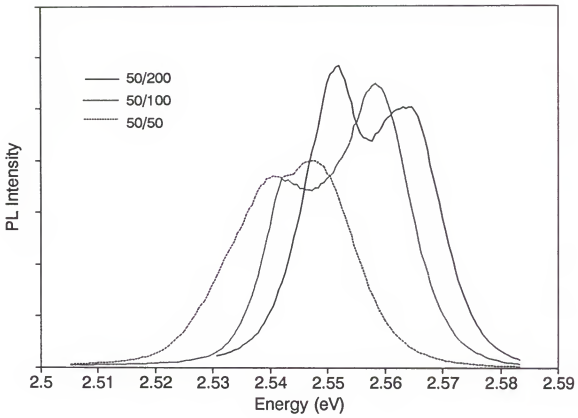

Figure 6-15 PL spectra of first group of samples (50/50Å, 50/100Å, 50/200Å) at 10K.

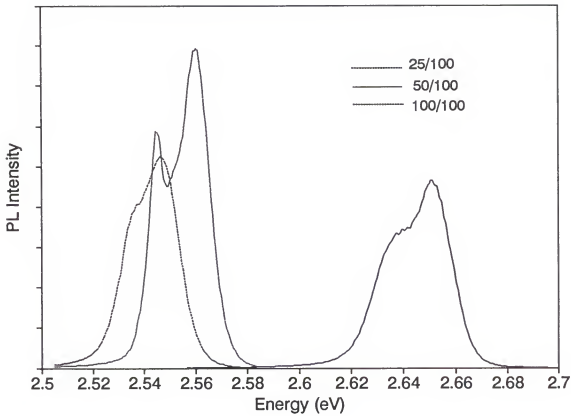

Figure 6-16 PL spectra of second group of samples (25/100Å, 50/100Å, 100/100Å) at 10K.

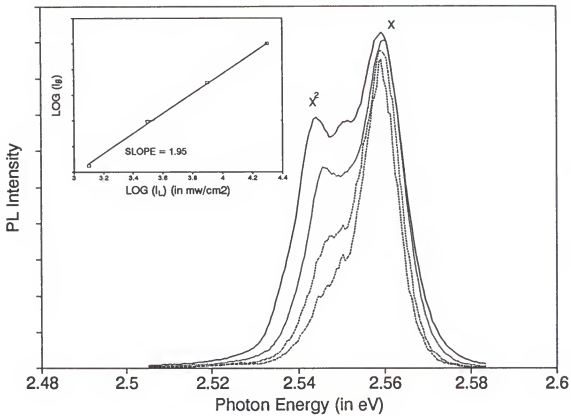

Figure 6-17 PL dependence on excitation power for 50/100Å MQW sample. The curves correspond to excitation densities of 200μJ/cm^2, 80μJ/cm^2, 32μJ/cm^2, and 13μJ/cm^2, respectively.

1.95, (i.e. $I_B \propto I_0^{1.95}$). The biexciton intensity indeed follows the superlinear dependence on excitation power as expected.

The second experiment is to verify the very fast biexciton decay lifetime. Population experiments were conducted to measure the decay lifetimes of biexcitons and excitons for the sample. Figure 6-18 shows the experimental results obtained with the two excitation beams cross circularly polarized. The PL correlation signal versus time delay was plotted on a logarithmic scale, and a straight line was obtained assuming an exponential decay behavior. The reciprocal of the slope yields the carrier decay lifetime. A biexciton decay time of 108ps and an exciton decay time of 266ps were obtained from the experimental data (The uncertainty of the decay lifetime measurements is <10ps). The biexciton indeed decays much faster than the exciton as current theory by Haug et al. predicted. Similar biexciton decay behavior in GaAs QWs has been reported by several groups (187, 188, 194).

The third experiment is to verify the polarization dependence of biexciton transition due to its two-photon absorption nature. We repeat the above population mixing experiment with the two excitation beams co-circularly polarized. The exciton decay behavior was unchanged. However, the biexciton PL correlation signal was completely absent, indicating no biexciton transition was present. This is exactly what is expected for the biexciton transition, since biexciton formation requires the interaction of σ^+ and σ^- excitons with opposite internal spins through a two-photon

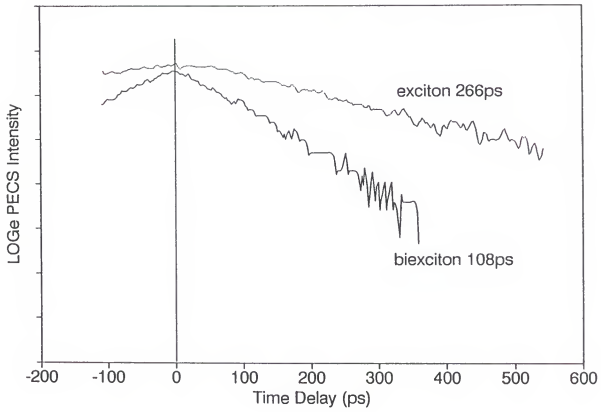

Figure 6-18 Exciton and biexciton PL decay spectra obtained from the population mixing experiments for 50/100Å sample at 10K.

absorption process, while exciton formation is independent of σ^+ and σ^- transitions.

The final evidence of biexciton formations is from the lineshape analysis of the biexciton. As discussed earlier, the biexciton line assumes a reversed Boltzmann distribution due to its recombination kinetics. Due to the lack of fast enough gated windows, a time-resolved luminescence experiment as conducted by Charbonneu et al. (179) couldn't be conducted to verify experimentally the reverse Boltzmann lineshape of the biexciton we observed. However, the spectral lineshapes could be fitted theoretically by generating forward and reverse Boltzmann distributions for the free exciton and biexciton respectively. The effects of collisions of biexcitons with excitons and biexcitons were taken into consideration by taking the convolution of a Lorentzian function with the Boltzmann function, as suggested by Shionoya et al.(178). Here Gaussian broadening is assumed due to the inhomogeneous broadening caused by well width fluctuations in the MQW sample. The reverse Boltzmann distribution equation is given by (178)

$I(E) \propto E^{1/2}\exp(-E/kT)$,

where $E=\hbar^2k^2/4M=E_{ex}-E_B-h\upsilon$ (6-17)

where E_{ex} is the energy of an exciton, E_B is the binding energy of the biexciton, and M is the mass of the exciton. With increasing density of excitonic molecules, elastic collisions between excitonic molecules and also that between a molecule and an exciton, which is produced as the result of radiative annihilation of a molecule, becomes considerable. Taking this effect into consideration, the biexciton spectrum is calculated as a function of E (defined in 6-21) as follows:

$$I(E) \propto A \int_0^{\infty} \frac{n(\varepsilon)\Gamma\varepsilon^{1/2} d\varepsilon}{(E-\Sigma-\varepsilon)^2+\Gamma^2} \begin{cases} A' E^{1/2} \exp(-E/kT) & \text{for } \Gamma \ll kT \\ \dfrac{A\Gamma}{(E-\Sigma)^2+\Gamma^2} & \text{for } \Gamma \gg kT \end{cases}$$

where $n(\varepsilon)$ is the Boltzmann distribution function; Γ is the sum of the relaxation frequencies of a single exciton and a biexciton. $\sum$ is given by $N(w_0-u_0)$, in which N is the number of biexcitons, and Nw_0 and Nu_0 are the shifts of energy levels of a biexciton and an exciton, respectively, due to the elastic collision with N biexcitons. The above equation indicates that the spectral shape changes from the inverse Boltzmann distribution in the low density limit to the Lorentzian type in the very high density case. The convolution of low density limit and high density limit was used for the fitting of our data.

The exciton line shape was fitted with a forward Boltzmann function in the form of $I(E) \propto \exp(-h\upsilon/kT)$, where $h\upsilon$ is the photon energy.

The fitted spectrum along with the experimental spectrum are shown in figure 6-19. Very good agreement between theory and experiment was achieved. A biexciton binding energy of 10meV and carrier temperature of 40K were obtained from the fitting. Comparable biexciton binding energies (10-14meV) have also been reported by two other groups in similar structures very recently (195, 196).

Based on all the evidences presented above, we confirmed the formation of biexcitons in the CdZnSe/ZnSe MQW samples. The observation of biexciton process in this material system is very significant not only for the sake of fundamental interest in photo-excited carrier dynamics but also for practical applications. At present, CdZnSe/ZnSe MQWs are the major candidate for

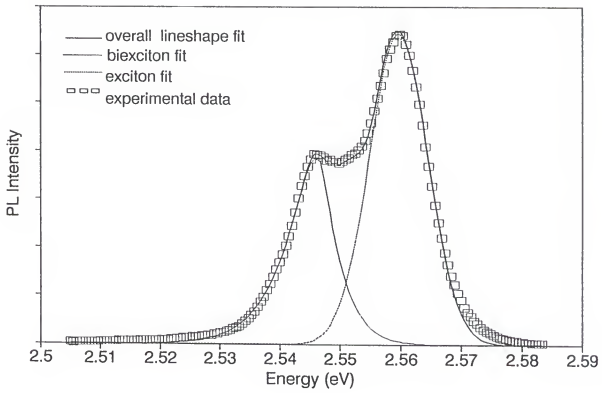

Figure 6-19 Theoretical fits of the exciton and biexciton PL spectra for 50/100Å sample at excitation density of 80$\mu J/cm^2$. The biexciton peak is fitted with reverse Boltzmann distribution function and the exciton peak is fitted with forward Boltzmann function.

fabricating short wavelength (blue-green) diode lasers. An understanding of high carrier density physics (i.e. biexcitons, exciton collisions) is evidently very important for investigating the lasing mechanisms in these structures. Our investigation of lasing mechanism in CdZnSe/ZnSe MQWs is presented in the section titled "Lasing Mechanism in CdZnSe/ZnSe QW Diode Lasers".

If we compare the binding energies of the exciton and biexcitons of the QWs, 40meV, 10meV, respectively, with those of the bulk material, 19meV (160), 3.5meV (197), respectively, we found that the binding energy of the biexciton increased more than that of the exciton over the bulk value, which means that biexcitons are more quantum confined or localized compared to excitons. We will come back to this conclusion in later sections.

The Role of Barrier Thickness

Table 6-5 is a summary of low temperature experimental results of the MQWs samples. Figure 6-15 shows the steady-state PL spectra for the first group of samples with different barrier thicknesses. As illustrated in the figure, all samples show free exciton and biexciton peaks. However, the 50/200Å sample shows the most pronounced biexciton peak, 50/100Å sample shows the intermediate, and 50/50Å sample shows the least pronounced biexciton peak. The energy positions of exciton and biexciton transitions for the three curves follow the order (from high to low): 50/200Å, 50/100Å, 50/50Å. The highest exciton and biexciton energy positions as well as most pronounced biexciton transition of 50/200Å indicate that this sample is most confined and has the highest transition oscillator strength. Since

the three samples have the same well thickness, the difference in oscillator strength can only be caused by the difference in barrier thickness. Barrier thickness influences the oscillator strength through the cross-coupling effect, as discussed in the room temperature results section. The presence of finite barriers in our samples allows wavefunctions of the wells to interact among nearest neighbors and leads to the formation of minibands. The bandwidth of those minibands decreases with increasing barrier thickness as the amplitude of wavefunctions get attenuated more severely in the barriers. The formation of minibands decreases the oscillator strength due to less degree of carrier localization. The 50/200Å sample has the largest barrier width, so strongest oscillator strength is expected for this sample. This is exactly what we have observed from the data. The largest relative intensity ratio of biexciton to exciton peaks in 50/200Å sample is due to the fact that the biexciton is more localized by quantum confinement than the exciton (a conclusion reached earlier from the comparison of enhancement in binding energies). As a consequence, the biexciton oscillator strength is more enhanced and its intensity increases more than that of the exciton.

If we compare figure 6-15 with figure 6-8, we notice that the difference in PL intensity between three samples is reduced at low temperature as compared to that at room temperature. This follows the expected behavior based on cross-coupling theory. Cross-coupling between neighboring wells is actually a carrier tunneling process. Due to well width fluctuations, the electronic levels of different wells are not at resonance, so carrier tunneling from one electronic level in one well to a level

in another well requires a momentum- and energy-conserving collision, such as impurity or interface roughness scattering, acoustic or optical phonon scattering. It has been shown both experimentally and theoretically (198, 199) that optical phonon assisted tunneling is considerably stronger than other mechanisms. Applying this conclusion to our data, the LO phonon effect is greatly reduced at low temperature (10K), so the tunneling probability is also reduced accordingly. As a result, the cross coupling effect is reduced for all samples and the difference in oscillator strength caused by cross coupling is reduced as well.

It worths noting that direct bandwidth comparison of the three samples at low temperatures is not appropriate here due to the overlapping of exciton and biexciton emissions. It is possible, however, to theoretically fit each transition lineshape by taking into consideration all possible interactions between these two processes, and then deduce the linewidth of each transition from the fitted spectrum.

Figure 6-20 shows the decay lifetime results of excitons and biexcitons for the three samples with upper portion showing exciton decay comparison and lower portion showing biexciton decay comparison. The exciton decay behavior for the three samples follows the same trend as that at room temperature: the 50/200Å sample exhibits the longest exciton decay time; the 50/50Å sample exhibits the shortest decay time. The same principle can be used to explain the decay behavior, i.e., $1/\tau_{tot} = 1/\tau_{esc} + 1/\tau_{rec}$ with other decay channels being equal for all samples and keeping in mind that carrier escape time τ_{esc} due to tunneling dominates over direct interband free exciton recombination lifetime τ_{rec}. Since 50/200Å sample has much

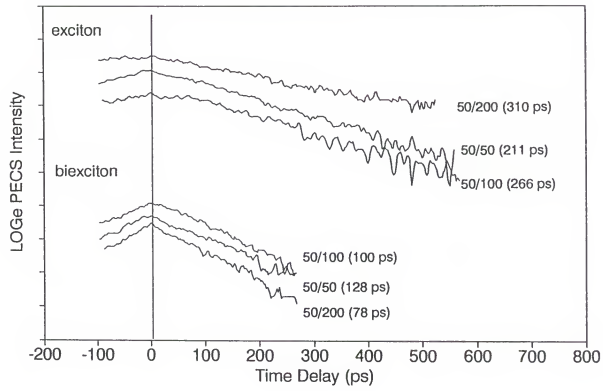

Figure 6-20 PL decay spectra of excitons and biexcitons for the first group of samples (50/50Å, 50/100Å, 50/200Å).

longer τ_{esc}, it displays the longest τ_{tot}; while 50/50Å sample has much shorter τ_{esc} thus the shortest τ_{tot}. Again, free exciton dynamics is proved to be dominated by carrier escape due to or tunneling rather than the transition oscillator strength.

If we compare the free exciton lifetime for the same sample at 10K with that at room temperature, we find that the free exciton lifetime is much shorter and its intensity is much stronger at low temperature. This behavior is mainly due to the more efficient interband exciton recombination rate in the absence of significant optical phonon scattering at low temperatures (8).

If we compare the difference in exciton decay lifetimes of the three samples at low temperature with that at room temperature, we find that the difference is much more reduced as in the case of difference in intensities. The reason is also due to the reduction of LO-phonon assisted tunneling.

The lower portion of figure 6-20 shows a comparison of biexciton decay lifetimes for the three samples. The biexcitons decay much faster than excitons for all samples, as expected. The 50/200Å sample exhibits the shortest biexciton lifetime, followed by the 50/100Å sample, while the 50/50Å sample exhibits the longest biexciton lifetime. This sequence indicates that transition oscillator strength is the dominant factor in determining the biexciton dynamics, since we still have $1/\tau_{tot} = 1/\tau_{esc} + 1/\tau_{rec}$. The 50/200 sample has the longest τ_{esc} and shortest τ_{rec}. Since τ_{rec} dominates over τ_{esc}, this sample displays the shortest τ_{tot}. The biexciton dynamics are thus very different from the exciton dynamics: the exciton dynamics is dominated by carrier escape from wells into barriers due to the cross-coupling

effect, whereas the biexciton dynamics are dominated by the transition oscillator strength. This difference reflects the enhanced localization of biexcitons as compared to excitons, a conclusion we reached earlier in the previous section.

The Role of Well Thickness

The role of well thickness on exciton and biexciton dynamics is determined by examining the steady-state and transient PL results of the second group of samples with the same well thickness (50Å) but different barrier thicknesses (25/100Å, 50/100Å, 100/100Å). Figure 6-16 shows the steady-state spectra for the three samples. Again all samples exhibit exciton and biexciton transitions. The trend in intensity and energy position follows that at room temperature. The 50/100Å sample exhibits the highest intensities and most pronounced biexciton peak, indicating its stronger oscillator strength. The emission energy position of the 25/100Å sample is blue shifted significantly from those of the other two samples due to the strong quantum confinement with its rather thin well width ($\approx a_B/2$). The rather weak intensity of this sample is due to its significant wavefunction penetration into barriers with $(V_0\text{-}E)\approx 40$meV being very small. A detailed analysis can be found in the room temperature results section. The emission intensity and peak energy position of the 100/100Å sample compared to those of 50/100Å sample indicate its weaker oscillator strength due to its larger well width. The largest intensity ratio of the biexciton to the exciton in the 50/100Å sample in comparison with the others indicated the enhanced confinement experienced by the biexciton with respect to the exciton.

The reduced difference in intensities of the three samples at low temperature as compared to those at room temperature, as we have observed for the first group of samples previously, is also due to the reduction in LO phonon-assisted carrier tunneling at low temperatures.

Figure 6-21 shows the exciton and biexciton decay lifetime results for the three samples. Again, the biexciton decays faster than the exciton for all the samples as expected. The exciton decay follows the sequence (from fast to slow): 25/100Å, 100/100Å, and 50/100Å. This sequence is the same as the room temperature sequence. We will apply the same theory here to explain this sequence. For the 25/100Å sample, due to significant wavefunction penetration into the barriers (V_0-E≈40meV) and large oscillator strength ($L_z \approx a_B/2$), both carrier escape time τ_{esc} and direct interband recombination lifetime τ_{rec} are short, consequently, the overall free exciton lifetime τ_{tot} is shorter than those of the other two samples. Between the 100/100Å sample and the 50/100Å sample, it seems first that 50/100Å sample should decay faster because (V_0-E) is smaller and oscillator strength is larger. However, 100/100Å sample behaves nearly bulk-like ($L_z > 2a_B$), and carrier escape is more probable since tunneling can always occur at close to resonance in the presence of more bulk-like continuous density of states. Therefore, τ_{esc} is shorter for this sample than for 50/100Å sample. Although τ_{rec} is slow because of the weak oscillator strength, the overall exciton lifetime τ_{tot} is expected to be shorter if our theory still holds. The measured exciton lifetime for

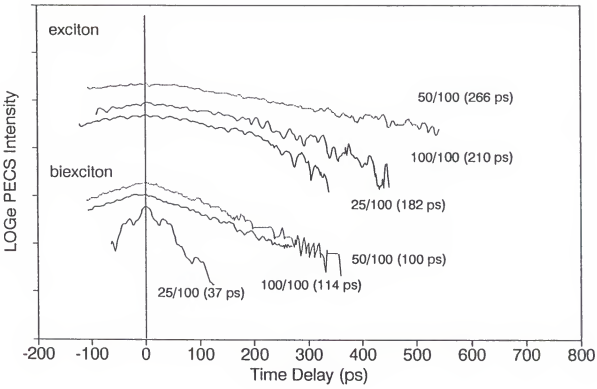

Figure 6-21 PL decay spectra of excitons and biexcitons for the second group of samples (25/100Å, 50/100Å, 100/100Å).

100/100Å sample is indeed shorter than that of 50/100Å sample, so we conclude once again than τ_{esc} dominates over τ_{rec} in exciton dynamics.

Table 6-5
Summary of Low Temperature Experimental Results of MQWs

sample	exciton position (eV)	biexciton position (eV)	exciton lifetime (ps)	biexciton lifetime (ps)	exciton intenisty	biexciton intensity
50/50Å	2.552	2.543	211	128	strong	strong
50/100Å	2.558	2.548	266	100	stronger	stronger
50/200Å	2.561	2.550	310	78	highest	highest
25/100Å	2.654	2.641	182	37	weak	weak
50/100Å	2.558	2.548	266	100	highest	highest
100/100Å	2.547	2.539	210	114	higher	higher

The reduced difference in exciton lifetimes of the three samples at low temperature compared to that at room temperature, as we also observed for the first group of samples, can be explained in terms of the reduction in LO phonon-assisted carrier tunneling as well.

The lower portion of figure 6-21 shows the biexciton lifetimes of the samples. The 25/100Å sample exhibits the shortest biexciton lifetime, followed by the 50/100Å sample, and the 100/100Å sample exhibits the longest biexciton lifetime. This sequence is consistent with our earlier conclusion from the biexciton behavior of the first group of samples that the biexciton is more quantum confined as compared to the exciton and its dynamics thus are determined mainly by the

transition oscillator strength. The 25/100Å sample has the largest oscillator strength thus the shortest biexciton lifetime, and the 100/100Å sample has the weakest oscillator strength thus the longest biexciton lifetime. The conclusion on exciton and biexciton dynamics is therefore verified again by the carrier lifetime data from the second group samples.

To summarize this section: biexciton transition has been observed in CdZnSe/ZnSe MQWs samples at 10K. The biexciton formation was confirmed by examining the superlinear intensity dependence on excitation power, spectral lineshape analysis, decay lifetime behavior, and transition polarization dependence. The roles of barrier thickness and well thickness on exciton and biexciton decay dynamics were investigated at low temperature by both steady-state and transient PL experiments. We found that the exciton decay dynamics are dominated by cross-coupling effects in the MQW structures, while the biexciton decay dynamics is dominated by the carrier confinement effect. We explain the difference between dynamics of excitons and biexcitons in terms of much enhanced quantum confinement experienced by biexcitons as compared to that by excitons, based on the fact that biexciton binding energy in MQWs is more enhanced over the bulk value than that of excitons. In the case of excitons, carrier tunneling from wells into barriers shorten the lifetime of the excitons when the barriers are very narrow.

Temperature Dependence Study of Carrier Lifetimes

The exciton and biexciton dynamics is studied as a function of temperature to investigate scattering effects by optical and acoustic phonons, by interfacial

defects, and by well thickness fluctuations. The exciton linewidth, which is fundamentally related to the exciton decay lifetime, can thus be determined as well. Understanding the mechanisms that contribute to the exciton linewidth broadening is not only of fundamental interest, but also of practical applications. It will be shown in later sections that the linewidth of excitons is an important factor in determining the operation characteristics of diode laser devices.

The relationship between the radiative free exciton lifetime and the exciton linewidth was derived by Feldmann et al. (70) for the infinite well case, and it is given by

$$\tau_x^{2D} \propto (E_x^{2D})^{-1}(M/\mu)\Gamma(T)/r(T)$$

where τ is the exciton lifetime, E_x is the exciton binding energy, Γ is the linewidth, r(T) is the fraction of excitons within the spectral width Γ that can contribute to recombination, which is given by (for Maxwell statistics) $r(T)=1-e^{-\Gamma(T)/kT}$. M and μ are given by: $M=m_e^*+m_h^*$, $\mu^{-1}=(m_e^*)^{-1}+(m_h^*)^{-1}$. The decay lifetime τ thus doesn't exhibit an explicit L_z dependence but depends on L_z implicitly through the exciton binding energy.

According to this equation, in the limit $\Gamma(T)<<kT$, the exciton lifetime τ is proportional to kT, while for $\Gamma(T)>>kT$, $\tau \propto \Gamma(T)$ is expected.

The free exciton lifetimes in the temperature range from 10K-298K were measured for the 50/200Å MQW sample by population mixing experiments. The temperature change is achieved by applying variable resistance heating to the

sample holder while keeping the cooling in operation. Figure 6-22 shows the plot of exciton lifetime versus temperature. In the low temperature regime (T<55K), the decay time versus temperature approximately follows a linear relationship, while for higher temperature regime (T>60), the decay time increases much faster with temperature. The behavior follows the above equation as demonstrated by the solid line. In the temperature range below 55K, the linewidth $\Gamma(T)$ is dominated by interface scattering and acoustic phonon scattering and is proportional to the phonon population which increases linearly with T for acoustic phonons: $\Gamma(T)=\gamma T$. γ was found to be 8.3μeV/K for CdZnSe/ZnSe QWs from four-wave mixing experiments (76), which yields $\Gamma(55K)=0.46meV$. Then $\Gamma/kT \approx 0.1$ and $\Gamma<<kT$ regime holds so we have $\tau \propto kT$.

For the temperature regime beyond 55K, we expect $\tau(T) \propto \Gamma(T)$. Assuming that the exciton transition is inhomogeneously broadened and neglecting impurity scattering (since these are undoped MQWs), the free exciton linewidth is given by the following equation derived by Lee et al. (200),

$\Gamma(T)=\Gamma_0+\gamma T+\Gamma_{LO}/\{\exp(E_{LO}/kT)-1\}$,

where Γ_0 is the inhomogeneous linewidth due to fluctuations of well thickness and interface roughness, γ is the acoustic phonon exciton coupling constant, and Γ_{LO} is the optical phonon-exciton coupling constant. Since $\tau \propto \Gamma$, we have

$\tau = A\{ \Gamma_0+\gamma T+\Gamma_{LO}/\{\exp(E_{LO}/kT)-1\}\}$, where A is a proportional constant.

We fitted the data with the above relation using the following parameters: LO phonon energy E_{LO}=31meV, Boltzmann constant $k=8.6\times10^{-5}$ eV/K. The fit is shown

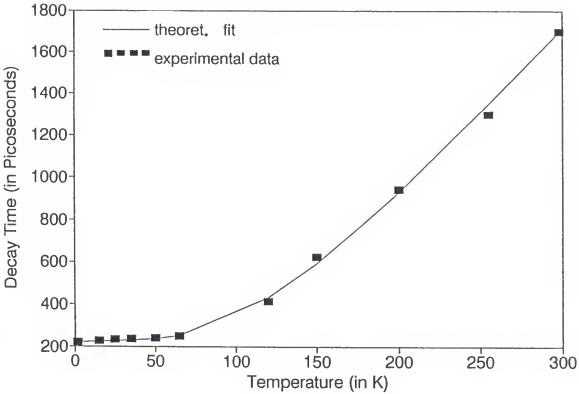

Figure 6-22 The dependence of exciton decay time on temperature. The squares represent data points and the solid line is the theoretical fit to the experimental data.

in the figure and yields Γ_{LO}=80meV, γ=8.3μeV/K, and Γ_0=5.4meV. The obtained values of Γ_{LO} and γ agree well with those reported by Hellmann et al. (201). The numerical values of Γ_{LO} and γ are much larger than those of GaAs wells (202), indicating stronger phonon scattering (both acoustic and optical) in ZnSe QWs. The inhomogeneous broadening linewidth (5.4meV) in the sample is also very large compared to high quality GaAs wells (<1meV (76)), which may be due to interface imperfections and well width fluctuations.

The biexciton decay time was also studied as a function of temperature up to 50K, above which temperature biexcitons begin to dissociate, and no definite relationship was found. The biexciton decay time seems to be independent of temperature. This conclusion agrees with recent theory on biexcitons (193) which includes the polariton effect.

To summarize this section, the heavy-hole exciton decay lifetime was studied as a function of temperature to determine the effect of exciton scattering by acoustic and optical phonons and also interface imperfections. Both acoustic phonon and optical phonon scatterings (Γ_{LO} and γ) were found to be much stronger than those of GaAs QWs. A very large inhomogeneous broadening was found as well.

Lasing Mechanism in CdZnSe/ZnSe QW Diode Lasers

CdZnSe/ZnSe quantum well structures have become a primary candidate for fabricating diode lasers in the blue-green spectral range. At present, device operation is still limited to cryogenic temperatures. The room temperature operation is difficult to achieve due to a significant reduction in gain in the presence of large

homogenous broadening by LO phonon scattering and large inhomogeneous broadening by native defects in the material. Room temperature operation has been demonstrated by several groups recently by using SCH-QW (separate confinement heterostructure quantum well) structures (203, 204), however, device operation is limited to less than an hour. Clearly, much progress is required, e.g., in improving intrinsic heterostructure, the contact resistance, and QW design.

A major issue concerning CdZnSe/ZnSe diode lasers, beyond the device structure optimization, is the mechanism giving rise to the stimulated emission and gain in these devices. In conventional GaAs QW based lasers, a degenerate free electron-hole plasma (EHP) induces population inversion which gives rise to stimulated emission and gain. In GaAs QWs, the exciton binding energy (≈8meV) is much smaller than the LO phonon energy (36meV), so exciton dissociation into free electron hole pairs by LO phonon scattering is very strong and the EHP model holds in describing the lasing process. In contrast, in CdZnSe QWs, the exciton binding energy (≈40meV) is larger than LO phonon energy (31meV), consequently the dissociation of excitons into free electron and hole pair continuum is much weakened. The strong, distinct exciton absorption features in CdZnSe QWs persist even beyond room temperature (205). The unusual robustness of excitons raises the basic question about the presence of correlated electron and hole pairs in the stimulated emission process in CdZnSe QWs. Is there any departure from the EHP model? It should be emphasized that EHP model will always come into play under sufficiently high injection current conditions at room temperature or above where

dissociation of excitons into free electron-hole pairs becomes more probable. However, the pertinent question concerns the possibility of stimulated emission by excitonic processes and the conditions under which this can be achieved.

Ding et al. (206) investigated the lasing mechanism in CdZnSe/ZnSe MQW lasers at cryogenic temperatures by optical pumping and pump-probe experiments. Their experiments were conducted on a MQW structure composed of six $Cd_{0.24}Zn_{0.76}Se$/ZnSe QWs with a 90Å well thickness and a 500Å barrier thickness. Optically pumped laser action was studied in cleaved structures of various lengths, with pump excitation directed along the z direction perpendicular to the QW layer plane. They found several experimental evidences that clearly indicate that the EHP doesn't play a role in the lasing mechanism in these lasers. First, the electron-hole pair densities remain sufficiently low at which laser emission commences so that the dissociation of excitons into degenerate electron-hole plasma is not probable. They found the electron-hole pair density at lasing threshold is in the order of $7x10^{11}$ cm^{-2}, which is an order of magnitude below the density at which the exciton phase becomes unstable with respect to an EHP ($n_c \approx (\pi a_B^2)^{-1} \approx 6x10^{12}$ cm^{-2}).

Second, stimulated emission emerges directly from the spontaneous emission line on the low energy side of the exciton resonance and doesn't exhibit any spectral shift under optical pumping at hh exciton resonance over several orders of magnitude of excitation level. This behavior is not consistent with the EHP picture of stimulated emission. From the conventional EHP model, the many body electron-hole Coulomb interactions renormalize the bandgap according to a carrier

density dependence. The bandgap or the emission energy decreases with increasing carrier density.

Third, results from pump-probe experiments at a pumping intensity close to the lasing threshold show that the exciton resonance remains present while supplying gain to the low-energy tail of the resonance. If the EHP process is responsible for lasing, excitonic absorption shouldn't be present at lasing threshold.

Finally, laser action commences readily once the excitation is tuned to the n=1 heavy-hole exciton resonance. This behavior indicates that stimulated emission is clearly related to excitonic processes. In the EHP model, the stimulated emission occurs as long as pumping is above the bandgap.

Based on these evidences, the EHP model is definitely not the lasing mechanism in CdZnSe QW lasers at cryogenic temperatures. The same group suggests exciton gain as the mechanism for stimulated emission based on a phase-space filling argument applied to an inhomogeneous system. In their model, an inhomogeneous exciton linewidth due to imperfections which substantially exceeds the homogenous linewidth is required. The exciton states in their model are non-overlapping and have a density below the electron-hole plasma transition. Large repulsive exchange interactions among them exist so that a given localization site can only be occupied by one exciton and the population inversion condition can be met. The occupied states lie at the bottom of the inhomogeneous exciton band. As a result, lasing involves excitons lying below the center of the exciton line, i.e., lasing occurs at the lower-energy tail of the heavy-hole exciton resonance. Their

mechanism requires the presence of imperfections in the QWs to localize excitons and could not operate in the absence of disorders or defects.

Flatte et al. (207) suggests that lasing in CdZnSe QWs is associated with a BCS-like condensed (coherent) exciton states. This state is most stable at low temperatures for densities in the transition region separating exciton Bose gas and the coherent exciton state. As a result, the gain region lies below the exciton line by the transparency region width, about 80meV from their calculations. Their mechanism requires the BCS like states of excitons, whose existence has never been observed experimentally. Also, the 80meV separation between lasing position and the exciton absorption is far too large compared to the experimental data by Ding et al. (206).

Here we propose a different lasing mechanism which doesn't rely on either imperfections or BCS condensed states. We suggest biexciton gain as the mechanism for stimulated emission in CdZnSe QW lasers. We have observed the biexciton transitions in our CdZnSe/ZnSe MQW samples with structures very similar to the sample studied by Ding et al. (206). Figure 6-23a shows the PL spectrum as well as the absorption spectrum for our 50/200Å sample at 10K. The two spectra were plotted on top of each other for peak energy position comparison. The energy separation between hh exciton resonance and hh exciton PL peak is known as Stokes shift resulted from localization of excitons (about 4meV from the figure). The relative position between the biexciton transition and the hh exciton absorption resonance (≈14meV from the figure) is found to be in coincidence with the energy

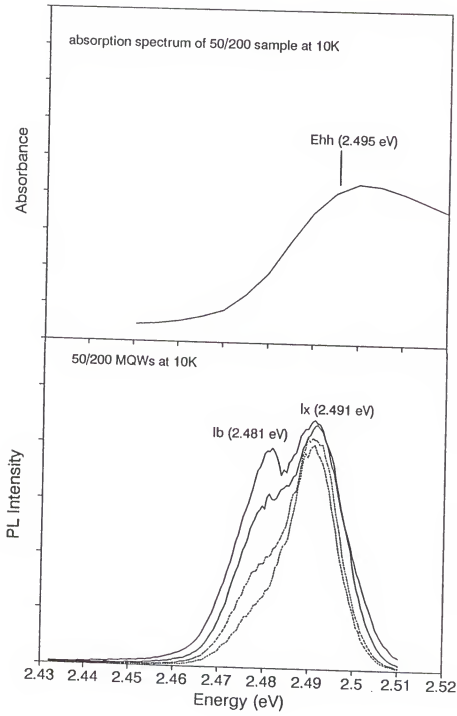

Figure 6-23a PL and absorption spectra of 50/200Å $Cd_{0.25}Zn_{0.85}Se/ZnSe$ MQW sample at 10K.

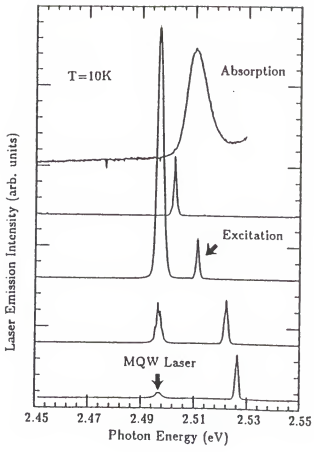

Figure 6-23b Resonant pumping of CdZnSe/ZnSe MQW laser at T=10K, with the top trace showing the n=1 heavy-hole exciton absorption resonance for reference (206).

separation between lasing position and hh exciton resonance observed by Ding et al. (12-14meV as shown in Figure 6-23b). We suspect that the lasing action observed by them is from the biexciton transition. To confirm our postulation, we made the following analysis.

Although the structure of our sample (50Å well width, 200Å barrier width with) is not exactly the same as their sample (90Å well width, 500Å barrier width), the hh exciton binding energy of our sample (E_{ghh}-E_{hh}≈40meV from the absorption spectrum) is found to be the same as their sample (reported to be 40meV), indicating the overall confinement level for the two samples is nearly the same. Consequently, the biexciton binding energies are expected to be the same. The energy position of the stimulated emission then coincides with that of the biexciton emission line.

The threshold electron-hole pair density of biexciton formation is well below that for degenerate electron-hole plasm, since an EHP is formed from the dissociation of both excitons and biexcitons at even higher densities (186). Therefore, biexciton gains occur at lower electron-hole pair densities than the case of conventional EHP model as they have observed.

Biexcitons are excitonic molecules formed from the condensation of excitons at high densities. The dissociation of a biexciton involves the emission of a photon, leaving behind a free exciton. The excitons resulting from dissociation can in turn form biexcitons again. The process between excitons and biexcitons is thus

recursive. The coupled dynamics of excitons and biexcitons can be described by (208)

$dn_B/dt=C(n_x)^2-n_B/\tau_B$,

$dn_x/dt=G-n_x/\tau_x-2C(n_x)^2+n_B/\tau_B$,

where n_B and n_x are the biexciton and exciton densities, respectively; C and G ($G\approx(n_0/\tau_1)\cdot\exp(t/\tau_1)$, with n_0 is the excitation carrier density, τ_1 is the exciton formation rate) are biexciton and exciton formation rates, respectively; τ_B and τ_x are the biexciton and exciton lifetimes, respectively. The above equations are based on the following assumptions: the effects of carrier-exciton, exciton-biexciton, and biexciton-biexciton collisions are not important; all the excited e-h pairs are assumed to first form from free excitons; the biexcitons are assumed to be formed from free excitons only; the role of bound excitons in the exciton dynamics is less important. At the excitation density level we are considering, these assumptions are valid within approximation, since exciton-biexciton, biexciton-biexciton collisions only become very significant at excitation levels where biexciton transitions are close to saturation. The bound excitons are not an issue here since they are nonexistent in QW structures as we have discussed previously.

Based on the above equations, the biexciton dynamics depends on the exciton dynamics and vice versa. The density of biexcitons goes as the square of that of excitons ($n_B \propto n_x^2$) while the biexciton decays more than twice as fast as the exciton ($1/\tau_B \geq 2/\tau_x$), so the biexciton population is expected to build up much faster than that of the exciton population. The population inversion can be readily

achieved once the biexciton formation rate becomes comparable to that of the exciton. When pumping at the exciton absorption resonance, exciton transitions have the highest absorption efficiency, so the generation rate of excitons is very high and the threshold for population inversion can be readily achieved. If pumping at non-resonance, the generation of excitons will be much less efficient, so lasing action is difficult to achieve. This explains the observation of laser emission once the pump is tuned directly into the hh exciton resonance.

The large binding energy (10meV) of biexcitons in CdZnSe/ZnSe QWs (10meV) makes biexcitons very stable. The opposite spins of two excitons (σ^+ and σ^-) in a biexciton cause the cancellation of screening effect at high biexciton densities (186). As a consequence, the biexciton binding energy remains remarkably constant over different levels of electron-hole pair densities. This explains the absence of spectral shift of stimulated emission in figure 6-23b.

The biexciton gain is consistent with the pump-probe results. Since the exciton state is the intermediate state, it will remain present on the absorption spectrum with reduced absorption while in the mean time biexciton transition induces gain.

The advantages of biexciton gain include the lower electron-hole pair density required at lasing threshold compared to the case of EHP and large internal efficiency due to enhanced biexciton oscillator strength. However, biexciton gain mechanism becomes invalid at higher temperatures (above 65K), where biexcitons become unstable and dissociate into excitons.

To summarize this section, the mechanism for stimulated emission in CdZnSe/ZnSe QW lasers has been examined. Based on experimental data from optical pumping studies of laser devices by Ding et al., we propose that biexciton gain is the lasing mechanism in these structures. This mechanism is consistent with the observations that stimulated emission occurs at the low energy tail of the exciton resonance, the emission exhibits no spectral shift with pumping intensities, and exciton absorption remains present in the pump-probe experiment.

Optical Degradation Study

CdZnSe/ZnSe MQW structures have become the primary candidate for fabricating diode lasers in the blue-green spectral range. Recent achievement of continuous wave operation of SCH-QW device at room temperature shows great promise and marks a major improvement in heterostructure design (209, 210). However, the lifetimes of these devices are limited to less than an hour, due to the pre-existing defects and subsequent propagation into the active region (211). Material degradation thus become a major problem in the further development of these lasers. Given the mechanical properties of relatively polar semiconductors, which imply more sophisticated dislocation dynamics, coupled with the low MBE growth temperature, the control of the defects and associated device degradation poses an inherently larger challenge than in III-V QW lasers. Structural degradation studies by transmission electron microscopy (TEM) and luminescence microscopy (211, 212) have confirmed the formation of dislocation networks in the active region, originating from the stacking faults in the epilayer substrate interface

introduced during the MBE growth. These dislocation networks act as non-radiative recombination centers and disable the lasing process.

In this study, we simulate the degradation process of these devices by optical excitation of the MQW sample at a carrier density level ($10^{12}/cm^2$), similar to that in a real device at room temperature. The change of luminescence intensity and carrier lifetime change as a function of time yields information on dislocation dynamics (1, 54): the presence of deep-level recombination centers (both radiative and non-radiative) decreases carrier lifetime and luminescence intensity. Second harmonic from the Ti:Sapphire Rega amplifier (400nm, 280fs, 250kHz) was used to excite the 50/50Å MQW sample constantly. A series of steady-state and transient luminescence spectra were taken at different time intervals after the start of the excitation. The excitation density was chosen to be $16\mu J/cm^2$, corresponding to $10^{12}/cm^3$ electron-hole pair density which is similar to that in a real device structure (111). The laser output power was monitored by an oscilloscope and kept constant to avoid any changes in luminescence intensity and carrier lifetime induced by laser power fluctuations. The population mixing technique was used to measure the carrier lifetimes. Figure 6-24a shows the plot of luminescence intensity versus degradation time and figure 6-24b shows the plot of carrier lifetime versus degradation time for a period of 60 minutes. Both curves are plotted on logarithmic scales. The two curves are very consistent with each other. Both curves show two linear regimes in logarithmic scale: fast degradation regime within the first 10 minutes, as evidenced by the significant drop in luminescence intensity and carrier

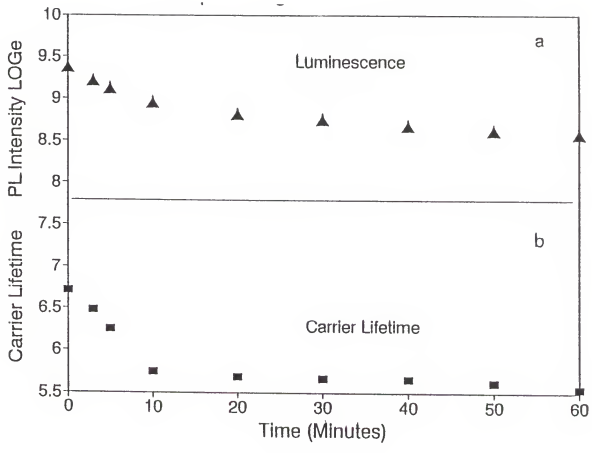

Figure 6-24 Experimental data from optical degradation study of 50/50Å MQW sample at room temperature. (a) luminescence degradation curve; (b) carrier lifetime degradation curve.

lifetime; slow degradation regime beyond 10 minutes, as evidenced by the slow change of luminescence intensity and carrier lifetime with time.

We interpret the data in terms of dislocation propagation kinetics. Before the excitation, the material consists of native defects from growth, mainly stacking faults in the epilayer-QW interface originated from those at the substrate-epilayer interface. After the start of excitation, these stacking faults serve as non-radiative recombination centers as carriers are created in the QW region by photon excitation. The energy released from these non-radiative recombination processes is transferred to the lattice by a multi-phonon process and speeds up the dislocation dynamics. Those stacking faults at the QW-epilayer interface which act as sources for misfit dislocations (213) in the QW region thus get activated and dislocation start to propagate into the QW region. Dislocations also act like non-radiative recombination centers and release energy back to the lattice. Thus, dislocation propagation is kept active by energy released from non-radiative recombination. Carrier trapping by these non-radiative centers decreases luminescence intensity and shortens the carrier lifetime. This explains the significant drop in both luminescence intensity and carrier lifetime we observed in the first 10 minutes. When the dislocations in the QW region build up to a certain density, dislocation networks form. The interaction between these networks will prevent the dislocations from further propagation and the density of dislocations tends to saturate. Accordingly, the luminescence intensity and carrier lifetime tend to saturate also. This explains what is observed beyond 10 minutes.

The luminescence intensity is given by $I_L \propto p \cdot n$, and the carrier lifetime in the presence of non-radiative centers can be approximated by $\tau = 1/\{Bnp + <\sigma v> N_t\}$ (167), where n and p are electron and hole densities participating in radiative recombinations, B is the radiative recombination rate coefficient, σ is the electron or hole capture cross-section, v is the thermal velocity, N_t is the concentration of non-radiative centers, and the average is over the energy distribution of electrons or holes. If I_L and τ follow exponential behaviors with time as shown in the data, then the trap concentration has to follow exponential behavior also. This indicates that the density of dislocations goes exponentially with time and so is the dislocation propagation rate during the degradation process. Structural studies need to be conducted to verify this behavior.

The shortening of carrier lifetime is more detrimental to a laser device than to a LED, since the population inversion necessary for lasing process is greatly reduced when carriers relax too fast to the ground state. As a result, lasing failure occurs at a much faster rate than in LED's.

Numerous structural studies by transmission electron microscopy (TEM) and X-ray diffraction (XRD) have been conducted on CdZnSe/ZnSe MQW structures (211-218). TEM micrographs clearly show the presence of stacking faults and dislocation loops in the ZnSe buffer layer. Below 180nm critical thickness, stacking faults are found to lie in the {111} planes in pairs and bounded by Frank partial dislocations in the [110] direction. Above the critical thickness, misfit dislocations develop and was found to lie along [110] directions in the {110} interface plane.

These dislocations are predominately of 60^0 type with small portions of Lomer edge type, which is formed from interactions of two 60^0 type dislocations (215). As the layer thickness increases, the ratio of edge to 60^0 type dislocations increases (216). The predominant mechanism for dislocation nucleation in the buffer layer was proposed to be surface sources, based on the fact that the majority of misfit dislocations just exceeding the critical thickness are of the 60^0 type and they are the only type obtainable from glide along {111} planes from the surface to the interface (217). The degradation of QW layer involves nucleation of dislocations at buffer layer/QW interface and dislocation propagation in the QW region. Nuleated dislocation dipoles form networks and appear as dark triangular patches bounded by <011>, and point defect segregation as a result of dislocation motion within the QW layer froms dark line defects along <100> direction. The well defined directions of degradation defects arise since patches are often bounded on one or more sides by misfit dislocations--a consequence of the interaction between the stress fields of misfit dislocations and degradation defects. These dark patches are non-radiative recombination centers and thus disable the lasing process. The kinetics of dislocation propagation in these structures is still under investigation at present.

To conclude this section, degradation of CdZnSe/ZnSe MQWs was studied by optical excitation at a carrier density equivalent to that in a real device. The luminescence intensity and carrier lifetime were found to decrease exponentially with time at a rate fast in the beginning and much slower afterwards. The data were

well explained in terms of dislocation propagation kinetics and confirmed the role of non-radiative recombination centers on the degradation process.

Hot Phonon Effect

Hot-phonon effect refers to the creation of a large nonequilibrium population of phonons in the semiconductor so that a free carrier has an increased probability of absorbing a phonon. Such a process leads to a reduction in the probability of emission of a phonon and therefore reduces the energy loss rate from carriers to the lattice. This effect is present in bulk as well as quasi-2D systems.

An excited electron in the conduction band must lose energy to the surroundings as it comes to equilibrium at the bottom of the band. In a polar material (such as GaAs, ZnSe), the most efficient energy relaxation process for energetic carriers is via LO-phonon emission, which continues until it is forbidden by energy conservation, i.e., until the electron is within one LO phonon energy (ω_{LO}) above the band bottom ($E<\omega_{LO}$). Afterwards, energy relaxation slows down and proceeds via acoustic phonon emission only. The emission of a LO phonon, by itself, doesn't take energy out of the combined electron plus lattice system. The emitted LO phonon must decay into acoustic phonons, which then thermalize with surrounding heat bath fairly quickly. The decay of a LO phonon into acoustic phonons (via anharmonic phonon-phonon interaction term) is, however, not instantaneous and involves a LO phonon lifetime τ_{LO}. When phonon emission time $\tau >> \tau_{LO}$, we can consider LO phonon decaying instantaneously, and τ by itself

defines the energy relaxation time. For $\tau \leq \tau_{LO}$, however, it is possible to build up a significant non-equilibrium phonon population and the hot electron may reabsorb some of these hot or nonequilibrium phonons, considerably slowing down its own relaxation. This hot-phonon effect is also referred to as the phonon bottleneck phenomenon.

In quantum well structures, like electronic states, phonon modes are also modified due to the confinement with respect to those in the bulk. Evidence for phonon mode modifications in QW structures has been found from Raman scattering experiments (219, 220). The LO phonon lifetimes, thus are expected to be different from those of the bulk. As discussed above, long LO phonon lifetimes compared to LO phonon emission times are essential for hot-phonon effects to be important. Theoretical models for phonon lifetimes are rather involved and only provide estimates (221). However, there are experimental evidences that the phonon lifetimes in 2D QWs are close to the bulk values and insensitive to well thickness (222, 223). Strong LO-phonon buildup in the cooling of hot carriers has been verified explicitly in GaAs QWs (224, 225). These observations lead to strong support that hot phonon effect is also important in QW structures.

In our experiment, we excited the 50/100Å MQWs sample with 400nm laser pulses (250fs, 250kHz) from Ti:Sapphire Rega amplifier, well above the heavy-hole exciton transition energy. The exciton decay lifetimes were measured by population mixing luminescence technique at exciton resonance at different excitation intensities corresponding to photoexcited carrier densities from 10^{15}-10^{13}/cm^3. Since

the excitation energy is well above the exciton transition energy (484.7nm), the carriers are first excited to the excited states in the conduction band. Then, excited carriers relax to the bottom level of electron states for interband recombination by emitting LO phonons. This thermalization time τ was measured to be much less than 1ps (77, 226). In the presence of a large density of carriers, as in our case, a large number of phonons are created. However, the LO phonon lifetime for II-VI QWs is known to be in the order of several picoseconds (227). Since $\tau < \tau_{LO}$, a non-equilibrium phonon population is thus created. The subsequent recombination of excitons is thus influenced by hot phonon population. By varying the photoexcited carrier density thus the hot phonon population, the influence of hot phonons on exciton recombination lifetime can be monitored.

Figure 6-25 shows the experimental results. The three curves correspond to three different excitation densities. It is evident from the spectrum that the exciton recombination lifetime becomes longer with increasing carrier densities, indicating hot-phonon induced reduction in combination rate.

We realize that interband recombination rate is not only influenced by hot-phonons, but also by exciton densities at high excitation intensities. However, exciton recombination rate is expected to increase with increasing exciton density, since the exciton decay time is given by (228)

$$\tau = \frac{2\pi\epsilon_0 m_0 c^3}{ne^2\omega^2 f}$$

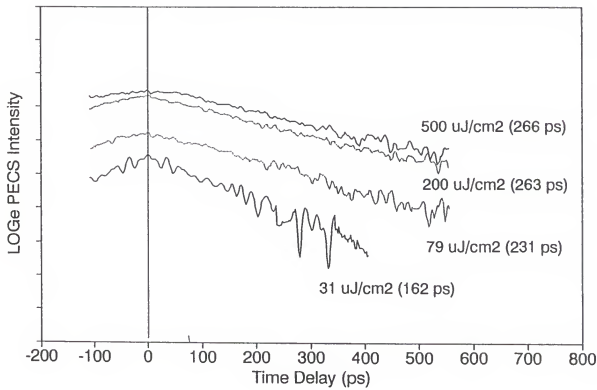

Figure 6-25 The dependence of exciton lifetime on excitation density for 50/100Å MQW sample at 10K showing the hot-phonon effect.

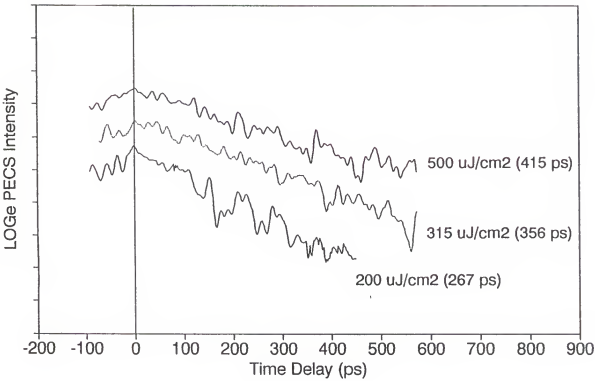

Figure 6-26 The dependence of exciton lifetime on excitation density for 50/50Å sample at room temperature also showing the hot-phonon effect.

where n is the exciton density, f is the oscillator strength, ω is the transition frequency. Below the EHP formation limit, this relation holds and $\tau \propto 1/n$. In our experimental conditions, the excitation densities used is far from the EHP limit, as evidenced by the presence of exciton and biexciton transitions in the steady-state PL spectrum. Therefore, the increase in exciton density under high excitation intensity doesn't contribute to the increase in exciton recombination lifetime, and the only possible mechanism that causes this increase is the hot-phonon effect.

The same experiment was repeated on the 50/50Å MQW sample at room temperature. Figure 6-26 shows the exciton decay time comparison at different excitation intensities. It is evident from the figure that exciton decays more slowly with increasing excitation intensities.

Carrier Tunneling Study

Carrier tunneling study was conducted on all the MQW samples at 10K to determine the importance of cross-coupling effect on carrier dynamics in each structure. The results will be used to verify the validity of our earlier conclusions on carrier tunneling.

In this experiment, we measure the decay lifetimes of donor-bound excitons I_d in the ZnSe barriers for each sample. The ZnSe barriers are actually undoped; however, the donors are unintentionally introduced during growth and are present in all MBE grown samples. The photoexcited carriers in the barrier material of a superlattice structure are subject to capture by wells as well as recombination in the barrier. The decay dynamics of these carriers are thus determined by both effects.

If we assume the recombination dynamics in the barrier are the same for all samples, then the differences in overall decay lifetime of the carriers reflect carrier capture dynamics by wells. The ZnSe barriers of all samples have nearly similar quality, since they were grown at exactly same conditions. The only difference is the layer thickness. To minimize the possible difference in recombination dynamics in the barriers caused by barrier thickness, we chose donor bound exciton transition as the probing process since bound excitons are more localized than free excitons and the recombination is not sensitive to layer thickness.

Figure 6-27 shows the steady state PL spectrum of ZnSe barrier showing the donor bound exciton emission at 2.796eV. Figure 6-28 shows donor-bound exciton decay time results from population mixing experiments for three samples with same well thickness but different barrier width (50/50Å, 50/100Å, 50/200Å). The 50/200Å sample exhibits the shortest decay time, followed by 50/100Å sample, and 50/50Å sample has the longest decay time. The difference in decay lifetimes is due to the difference in carrier capture efficiency of photoexcited carriers into the wells. If the capture efficiency is high, carrier capture time τ_{cap} will be short and bound exciton lifetime will be short also, since $1/\tau_{tot} = 1/\tau_{rec} + 1/\tau_{cap}$ with τ_{rec} being equal for all samples approximately. The carrier capture efficiency, thus, is highest for 50/200Å sample and lowest for 50/50Å sample. Higher carrier capture efficiency indicates less cross-coupling effect present, therefore, 50/200Å sample has the least cross-coupling, 50/100Å sample has stronger cross-coupling, and 50/50Å sample has the strongest. This is consistent with our earlier conclusions.

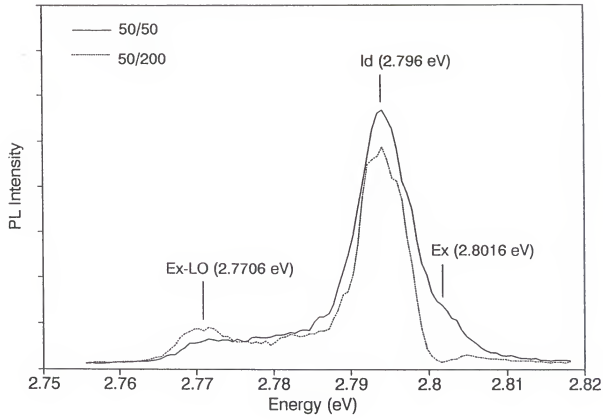

Figure 6-27 PL spectra of ZnSe barriers of CdZnSe/ZnSe MQWs at 10K.

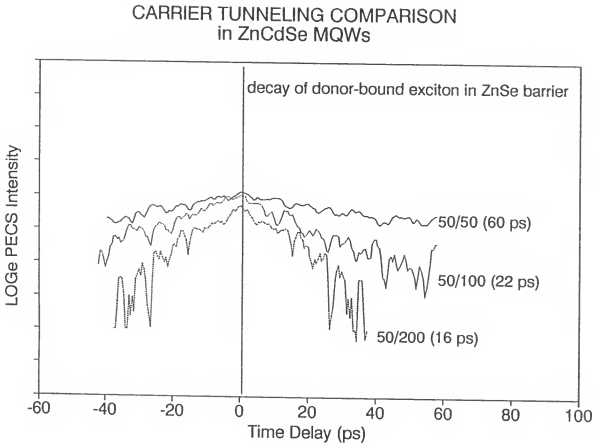

Figure 6-28 Donor-bound exciton decay spectra for the first group of MQW samples (50/50Å, 50/100Å, 50/200Å) at 10K.

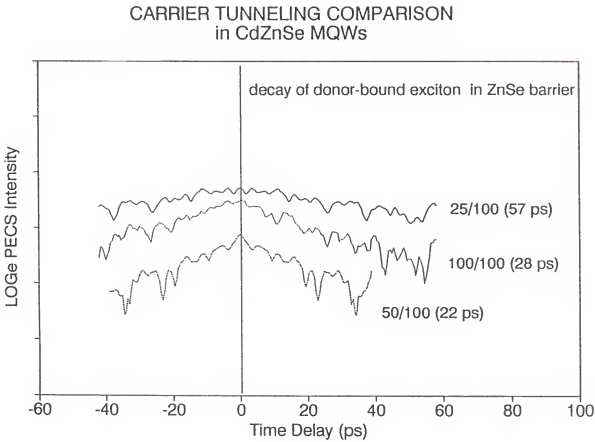

Figure 6-29 Donor-bound exciton decay spectra for the second group of MQW samples (25/100Å, 50/100Å, 100/100Å) at 10K.

Figure 6-29 shows the donor-bound exciton decay times for the other three samples with same barrier width but different well width (25/100Å, 50/100Å, 100/100Å). The 25/100Å sample exhibits longest decay time, and 100/100Å sample is the second, and 50/100Å sample exhibits the shortest decay time. 25/100Å sample has strong wavefunction penetration into barriers due to very small (V_0-E), so it has the least carrier capture efficiency and exhibits the longest bound exciton lifetime. The 100/100Å sample is more bulk-like and has strong carrier tunneling present, so its carrier capture efficiency is lower and bound exciton lifetime is longer compared to those of 50/100Å sample. The results are thus in excellent agreement with our previous conclusions.

To summarize, experimental results from carrier tunneling study further verified our previous conclusion on the importance of cross-coupling effects present in multiple quantum well structures on carrier dynamic behavior. The dominant role of carrier tunneling on carrier dynamics is once again confirmed.

Transient Differential Absorption Results

Transient differential absorption experiments were conducted on the 50/200Å MQW sample grown on ZnSe substrate to study carrier thermalization dynamics. Since ZnSe substrate has an absorption edge at a higher energy than the MQWs, absorption spectrum of the MQWs can be obtained without the need of removing the substrate. The experimental setup was described in detail in Chapter 5. Figure 6-30 is the absorption spectrum of the sample obtained by using the white light continuum output from the OPA as the probe. Several absorption features are

present: heavy-hole exciton edge at 499nm, heavy-hole gap at 492nm, and light-hole exciton edge at 483nm. These energy positions are identical to those shown in figure 6-7 for the same sample, which were determined by using commercial Perkin-Elmer UV-VIS-IR spectrometer. The pump beam is the signal output from the OPA tuned to 496nm and its spectrum is also shown in the figure for comparison. The 496nm pumping energy yields an excess carrier energy about 15meV ($=E_{pump}-E_{hh}$). Taking into the consideration that electron effective mass $m_e^*=0.153m_0$ and hh hole effective mass $m_{hh}^*=0.663m_0$ for $Cd_{0.25}Zn_{0.75}Se$, this gives an excess electron energy of approximately 12meV and an excess heavy-hole energy of approximately 3meV. The LO phonon energy of CdZnSe is about 30meV and the acoustic phonon energy is about 6meV. We thus expect both electron and hole thermalization to occur without the emission of LO phonons. Early thermalization should be dominated by carrier-carrier scattering, while at later times cooling will take place via acoustic phonon emission. The excitation density is approximately $0.16\mu J/cm^2$, which corresponds to an excited carrier density of $10^9/cm^2$. The white light continuum probe beam from the OPA was attenuated to energies such that there is no self-bleaching with respect to the exciton peak. The transient absorption of the sample derives from both coherent and population effects in the sample. In order to minimize the coherent artifacts, the pump and probe beams are cross-polarized. The zero time delay was calibrated through the two-photon absorption (TPA) of thin InP plate. The pulse duration of both the pump

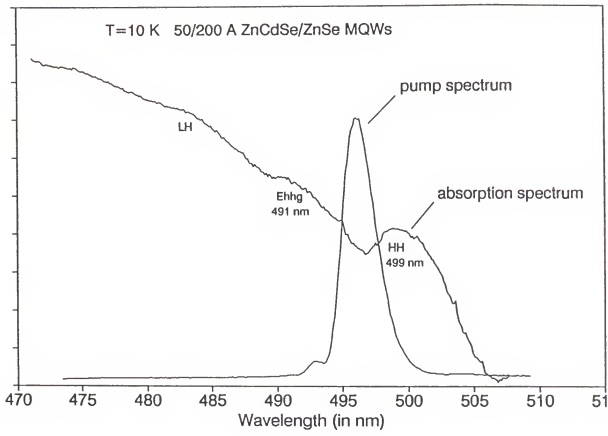

Figure 6-30 10K absorption spectrum of 50/200 $Cd_{0.25}Zn_{0.75}Se/ZnSe$ MQW sample and the spectrum of the pump pulse used in the experiment.

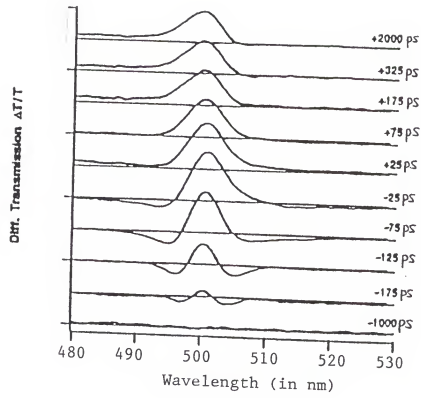

Figure 6-31 Spectrally resolved differential transmission of $Cd_{0.25}Zn_{0.75}Se/ZnSe$ MQWs, at various relative delays between the pump and the probe at 10K. Each curve is normalized and displaced in the vertical axis for clarity.

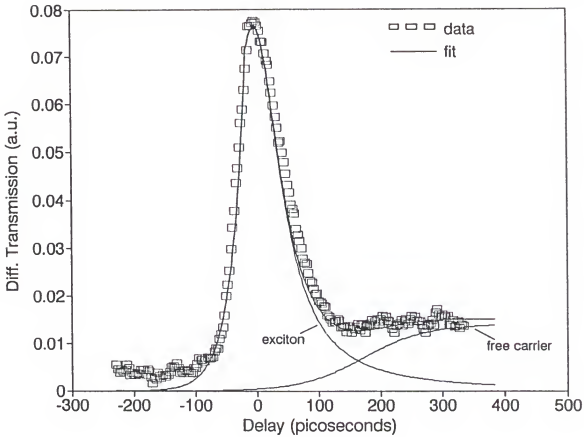

Figure 6-32 Pump probe differential transmission of 50/200Å $Cd_{0.25}Zn_{0.75}Se$/ZnSe MQWs at heavy-hole exciton resonance (499nm). Experimental data are shown in empty squares, and the theoretical fit is shown in solid line. Separate contributions of excitons and free e-h pairs are shown in dashed lines.

and the probe beams is about 200fs. The sample was maintained in a close-cycle Helium cryostat at 10K during the experiments.

Figure 6-31 shows the differential transmission spectra of the sample at different time delays between the pump and the probe. The oscillatory behavior at negative delays is due to the coherence effects between the pump and the probe and was well explained theoretically (229, 230). The origin of the oscillations is a transient population grating generated by the pump and probe together. The amplitude of the oscillation decreases exponentially with decreasing delay |t|, and their period is proportional to 1/|t|. The oscillations shown in the data are fully consistent with these predictions. From the figure, the hh exciton transmission experiences a rapid rise in the first 25ps and then decays with a time constant about 200ps. To take a closer examination on this behavior, we plot the differential transmission versus time delay at hh exciton resonance in figure 6-32 and the curve clearly shows the initial rise and subsequent decay dynamics. The initial rapid rise of transmission corresponds to the generation of excitons. The subsequent decay is due to exciton thermalization by exciton-exciton scattering and exciton recombination. The curve stabilizes to a smaller value at longer times because of the effects of free electron-hole pairs. Since free carriers are long-lived, hence their dynamic bleaching strength is constant at time scales we are interested. The ratio of the amplitude of the peak near zero delay to that of the plateau at longer times reflects the relative bleaching effects of excitons compared to free carriers. A slight increase in transmission following the excitation is also observed in the high

energy side of hh exciton absorption, which is due to the generation of free carriers. For the MQW sample under study, the hh exciton binding energy is about 40meV (E_{hhg}-E_{hh} from fig.6-30). The rather large exciton binding energy prevent excitons from dissociation into free carriers either by inelastic exciton-exciton collisions or LO phonon scatterings. At the temperature of our experiment (10K), the LO phonon scattering is minimized, so the free carrier generation is mainly from inelastic exciton-exciton collisions and is expected to be very weak due to the robustness of the excitons. The large binding energy of the excitons explains the rather large amplitude ratio of peak to plateau in figure 6-32. We theoretically analyzed the dynamics of the differential transmission in the resonant pumping situation using the following simple model (231, 232):

In the small signal regime, the change in exciton oscillator strength is linear in the density of excitons, N_x, or free electron-hole pairs, N_{eh} and we can write

$$\frac{\Delta f}{f} \propto \left(\frac{N_x}{N_s^x} + \frac{N_{eh}}{N_s^{eh}}\right) \propto \left(R_{eh/x} N_x + N_{eh}\right)$$

Here N_s^x and N_s^{eh} are exciton and electron-hole pair plasma saturation densities, respectively, and $R_{eh/x} = N_s^{eh}/N_s^x$. The mechanisms of carrier relaxation include generation of excitons by the resonant pump, exciton ionization into free carriers, and exciton recombination. The rate equations describing the exciton and free carrier populations can be written as follows:

$dN_x/dt = G_x(t) - N_x/\tau - N_x/\tau_r$

$dN_{eh}/dt=N_x/\tau$

where τ is the exciton ionization time, τ_r is the exciton recombination lifetime, and $G_x(t)$ is the generation rate of excitons which has the same time dependence as the pump pulse. The differential transmission response is the sum of the contributions from excitons and free carriers and can be written as:

$A=A_x(t)+A_{fc}(t)=\alpha_x\exp(-t/\tau)+\alpha_{fc}(1-\exp(-t/\tau))$

where α_x and α_{fc} are the bleaching strengths of the excitons and free carriers respectively, and $R_{eh/x}=\alpha_x/\alpha_{fc}$.

The fits to figure 6-32 were generated from the above equations. The solid line shows the total pump-probe response, and the contributions from excitons and free carriers were shown in dotted lines separately. The fitted parameters are the following: $R_{eh/x}=0.03$, $\tau=20$ ps, $\tau_r=220$ ps. The exciton recombination lifetime is in agreement with the value measured by population mixing technique for similar samples in section D of this chapter. The rather small $R_{eh/x}$ is due to the rather large exciton binding energy as we expected. The value of $R_{eh/x}$ for InGaAs QWs is about 3 (231). The exciton ionization time (20ps) is also considerably long as compared to other semiconductor QW structures such as GaAs, InGaAs, and ZnTe (231, 232, 77). Since the exciton binding energy is so large as compared to thermal energy at 10K, exciton ionization via thermal collisions is not probable. We suggest that an extrinsic ionization mechanism might be responsible for exciton dissociation at low temperatures. This extrinsic mechanism might be random electric fields generated by ionized impurities, which has been observed in GaAs QWs (232). A temperature

dependence study of differential transmission spectra will be conducted in the future and can help verify this postulate. From figure 6-32, the pump-probe response from free carriers is very small as compared to that of excitons, indicating that exciton ionization is not a very probable thermalization process and pump-probe response strongly depend on exciton recombination.

CHAPTER 7
EXPERIMENTAL RESULTS ON EPITAXIAL FILMS AND BULK CRYSTAL

In this chapter, major experimental results from carrier dynamics studies in ZnSe epitaxial films (undoped and doped) and single crystal (undoped) are presented. Theoretical analyses of these results are given and the basic physics involved is elucidated.

Room Temperature Results: Free Carrier Dynamics

At room temperature, the photoluminescence spectra of bulk materials are characterized by broad band-edge emissions. The exciton binding energy for bulk ZnSe is close to 19meV (157), and the LO phonon energy is 31meV, so excitons dissociate effectively into free carriers beyond cryogenic temperatures. Since the free carriers are not bound, the oscillator strength of the band-edge transition is much weaker than in the quantum well case. The band to band recombination dynamics are mainly determined by the quality of the material, e.g., the presence of defects or dopants.

Both steady-state and time-resolved PL were conducted on ZnSe epitaxial thin films grown on GaAs substrates by MBE and single crystal. Characteristics of these samples are shown in Table 4-3. The lattice mismatch between GaAs (5.6653Å) and ZnSe (5.667Å) is very small and yields a critical thickness of 180nm

for pseudomorphic layers. The epitaxial films under study are of 2μm thick, well above the critical thickness, so the strains are fully relaxed to misfit dislocations in the layers. The presence of defects (both radiative and non-radiative) affects free carrier lifetime by providing alternative paths for carrier recombination, so the free carrier lifetime is a direct measure of the quality of each sample.

Figure 7-1 shows the steady-state PL spectrum for the films. The PL spectrum from the crystal was not plotted on the figure for comparison because the crystal has a different thickness of 1mm and was fabricated by a different technique called vapor phase transport. Both the n-type and p-type sample have a dopant concentration in the order of $10^{17}/cm^3$ as confirmed by Hall measurements and sheet conductivity measurements. All samples show band-edge emission at 2.68eV. The doped samples show stronger intensity than the undoped sample. This difference is due to the presence of extra carriers introduced into the sample through doping, since luminescence intensity $I_s \propto n \cdot p$. The n-type film shows stronger emission than p-type film because the chlorine donor is shallower than the nitrogen acceptor (shown in the 10K PL spectrum) and the donor-to-band transition contributes to the band-edge emission more than the acceptor-to-band transition, assuming the quality of the two samples is the same.

Figure 7-2 shows the decay lifetimes of all samples measured from population mixing experiments. The crystal exhibits the longest decay (1.1ns), consistent with the decay time of ZnSe crystals reported by Charbonneau et al. (61). The films, however, decay much faster compared to the crystal: p-type and n-

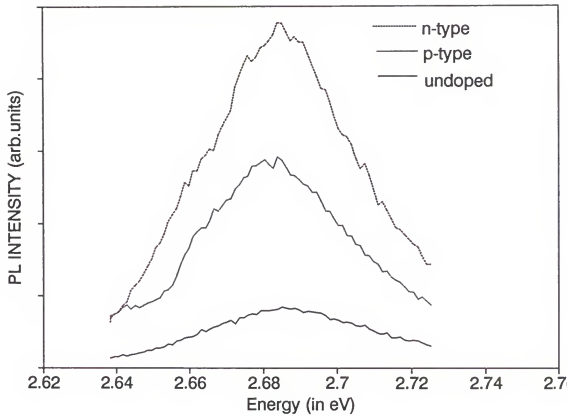

Figure 7-1 Room temperature PL spectra of ZnSe epitaxial films (both doped and undoped).

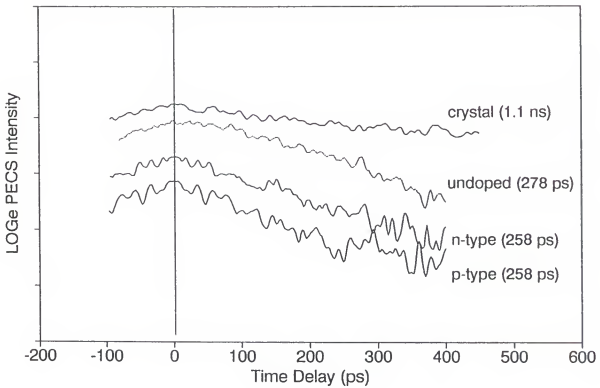

Figure 7-2 Free carrier PL decay spectra of ZnSe epitaxial films and crystal at room temperature.

type samples exhibit a similar decay lifetime, and the undoped one decays more slowly. The film decay times also agree with those values reported recently (56, 57). The much faster decay behavior of films as compared to the crystal is mainly due to the difference in material quality, e. g., more non-radiative recombination centers such as stacking faults and dislocations present in the films than in the crystal. The much thinner thickness of the epitaxial films doesn't contribute to this effect, since the laser penetration depth L for direct band transitions is given by (233)

$L = 1/\alpha \approx 0.5(h\upsilon - E_g)^{-1/2}$ μm,

where α is the absorption coefficient, E_g is the energy gap in eV, $h\upsilon$ is the excitation energy of the light source in eV.

At $h\upsilon$=400nm, L is about 0.5μm, which is much less than the film thickness (2μm), so carrier recombination at ZnSe/GaAs interfacial states is not probable. Also, carrier diffusion can be neglected since the diffusion length for free carriers in subnanosecond scale is less than 0.5μm assuming an ambipolar diffusion coefficient of $2.5 cm^2 s^{-1}$ (234). Therefore, recombination only occurs in the film or at the surface in the subnanosecond time scale.

The rate equations describing bandedge luminescence decay for a n-type material, assuming a three-level system (conduction and valence bands, deep-acceptor level) and minority carrier trapping via acceptors in the dominant recombination pathway, is given by (60)

$dn/dt = -Bnp - bp_1 n,$

$dp/dt = -Bnp - s(p_2 - p_1)p,$

$dp_t/dt = s(p_2-p_t)p-bp_tn$,

where n and p are electron and hole concentrations, p_t is the trapped hole concentration, B is the radiative coefficient for band-edge recombinations, s is the ratio of capture of holes by traps, p_2 is the trap concentration, and b is the recombination rate for trapped holes. The band to band PL intensity is given by $I_B=Bnp$ and deep-level PL intensity by $I_t=bnp_t$.

The rate equations for the p-type material with deep donor levels can be obtained by simple exchange of n and p in the above equations. For heavily doped n-type sample at low excitation densities (i.e. n>>p and p_2>>p), the band edge luminescence decay can be described by $\tau_{Bn}=1/(Bn+sp_2)$. In the case of p-type sample, this will be written as $\tau_{Bp}=1/(Bp+sn_2)$.

The undoped sample is actually slightly n-type ($\approx 10^8/cm^3$) due to the unintentionally introduced dopants during growth as well as the defects present. Figure 7-2 shows that the n-type sample exhibits slightly shorter decay time than the undoped one. From luminescence decay lifetime $\tau_{Bn}=1/(Bn+sp_2)$, this behavior indicates that the decay is dominated by the trap capture term, sp_2, since the decay rate doesn't increase proportionally with doping level. The upper limit of B was found to be $\approx 1.1x10^{-9}$ $cm^{-3}s^{-1}$, which agrees with values reported in the literature (56, 60), indicating the material is of average quality.

The possible trapping mechanisms in doped n-type and p-type samples might be dislocations, stacking faults, nitrogen interstitials, selenium vacancies, and

selenium vacancy complexes, which are typically present in higher level doped ZnSe samples (57).

To summarize, room temperature time-resolved PL has been conducted on ZnSe epitaxial films and bulk crystal. The free carrier lifetime is a direct measure of the quality of the sample. The single crystal is found to be of higher quality than the films. The dominant bandedge recombination mechanism of films is found to be the carrier trapping via deep centers.

Low Temperature Results: Free and Bound Exciton Dynamics

At low temperatures, LO phonon effects are greatly reduced. Photoluminescence lines from different optical processes are separated. The PL spectra of bulk semiconductors are characterized by a series of distinct emission bands from free excitons, donor or acceptor bound excitons, and other complexes. Different processes associated with these emission bands can be identified and studied. Low temperature PL has always been a very valuable tool to evaluate the quality of materials. From emission energy positions of donor and acceptor bound excitons, impurity and dopant species present in the sample can be identified. From the energy positions of donor-to-acceptor transitions, the average distance between donors and acceptors can be determined. In addition, many novel processes which are of fundamental research interest, such as biexcitons, phonon-plasmons, and two-electron-satellites, can only be observed at low temperature photoluminescences. Carrier dynamics studies at low temperatures yield information on dynamic behaviors of different processes of interest including free

and bound exciton dynamics, deep-level dynamics, lattice (phonon) dynamics, carrier-carrier scattering dynamics, and carrier-phonon interaction dynamics. In this section, experimental results on exciton dynamics of ZnSe epitaxial films (n-, p-type) and bulk crystal are presented and analyzed.

Both steady-state and time-resolved PL were conducted on these samples with second harmonic from the Ti:Sapphire Rega amplifier (400nm, 280fs) as the excitation source. Figures 7-3 to 7-5 show the steady-state PL results for the samples at two different excitation densities (corresponding to photoexcited carrier densities of 10^{14} and $10^{12}/cm^3$). Bound exciton emission lines dominate in all spectra. The specific process that each emission line corresponds to was identified and shown on the graphs. The following notations were used in the figures: E_x for free exciton; I_d for donor-bound exciton; I_a for acceptor-bound exciton; LO for longitudinal optical phonon replica; TA for transverse acoustic phonon replica; and s for strain induced splitting. The assignment of each process is based on the following criteria. First, characteristic transition energies of common processes for epitaxial MBE grown ZnSe films are well known from the literature (235, 236): free exciton at ≈2.802eV, neutral-shallow-donor bound exciton at ≈2.799, neutral-shallow-acceptor bound exciton at ≈2.790eV, donor-to-acceptor pair emission at ≈2.69eV. Second, the LO-phonon energy of ZnSe is 31meV, so all phonon replica are separated from their parent emission lines by integral multiples of 31meV in energy. Finally, decay lifetime behavior can be used to identify different processes, since it reflects the intrinsic dynamics of each individual process. This is especially

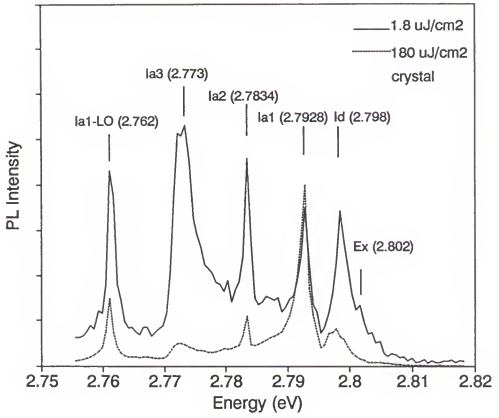

Figure 7-3 PL spectra of ZnSe crystal at 10K.

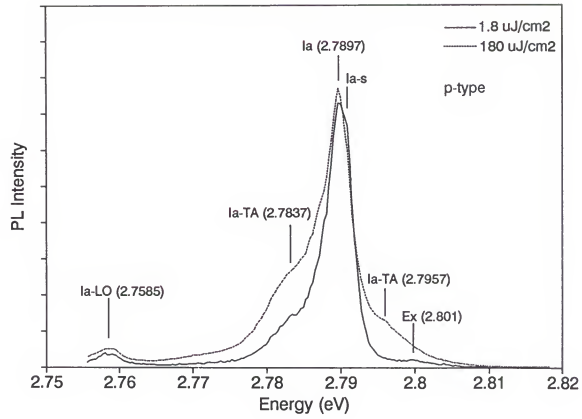

Figure 7-4 PL spectra of p-type ZnSe epitaxial film at 10K.

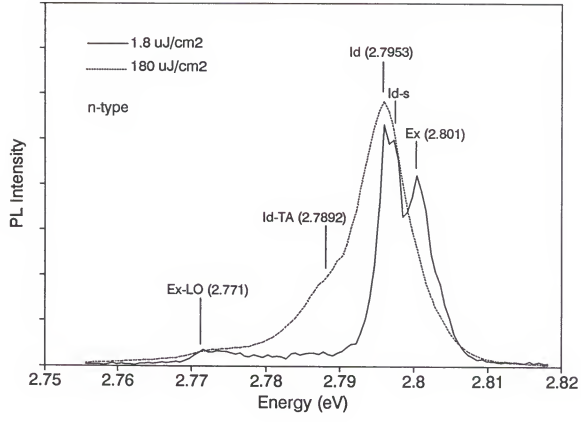

Figure 7-5 PL spectra of n-type ZnSe epitaxial film at 10K.

useful when several processes happen to have same transition energies. At low excitation density, the spectrum of p-type sample is dominated by acceptor-bound exciton I_a and donor-to-acceptor transition (DAP), while that of the n-type sample is dominated by free exciton E_x and donor-bound exciton I_d, and that of crystal is by donor and acceptor bound excitons and LO phonon replica. At high excitation density, the emission lines are less distinct for all spectra compared to those at low excitation densities. The free excitons are almost disappeared, while the relative intensity ratio of the LO phonon replica to their parent emission lines is reduced. This behavior reflects the more pronounced role of carrier-carrier scattering on the carrier relaxation process as explained below.

At the excitation energy of $h\upsilon$=3.1eV, well above the bandgap of ZnSe (E_g=2.82eV), the carriers are excited to higher energy states above the bottom of the conduction band. The relaxation of these carriers to the bottom of the conduction band for recombination can be achieved by LO-phonon emission, inelastic carrier-carrier scattering, and intervalley scattering. In our case, the intervalley scattering is not possible since the excess energy $h\upsilon$-E_g is below the energy threshold for intervalley transfer. At low carrier densities, the dominant carrier relaxation mechanism is LO-phonon emission, which doesn't broaden the initial electron distribution significantly and the spectra are characterized by a series of peaks separated by the LO phonon energy. At high carrier densities, carrier-carrier scattering begins to play a role, which broadens the carrier energy distribution rapidly, and the spectrum is characterized by broad emission lines with

less pronounced LO phonon replicas (6). This is exactly what we observed from our data. The spectrum of the crystal shows this effect the most. All emission lines are broadened and the relative intensity ratio of LO-phonon replica to their parent emission lines is more reduced at higher excitation density than the case of low excitation density. The free exciton lines disappeared at high carrier density due to the screening effect; the bound excitons, however, remain strong since they are localized and less affected by screening.

Hot carrier relaxation through carrier-carrier scattering occurs in a very short time scale ($\tau_{c\text{-}c}$<500fs) (5, 42), beyond the temporal resolution of our experiment, so this process can't be time resolved in these samples. The carrier lifetimes thus measured by the population mixing technique are the recombination times only, since $\tau_{tot}=\tau_{c\text{-}c}+\tau_{rec}$ and $\tau_{c\text{-}c}$ is very short, so $\tau_{tot}\approx\tau_{rec}$.

The decay lifetimes of different processes for these samples are shown in figures 7-6 to 7-8. There are several features that are common for all samples: first, free excitons exhibit longer lifetimes compared to bound excitons; second, free exciton LO-phonon replica exhibit longer decay lifetime compared to the corresponding free excitons; finally, the bound exciton LO phonon replica exhibit similar decay lifetimes as the corresponding bound excitons. The longer decay times of free exciton LO-phonon replica can be explained in terms of the polariton nature of the free excitons (176). The LO-phonon assisted luminescence is not reabsorbed by the sample, so its intensity is

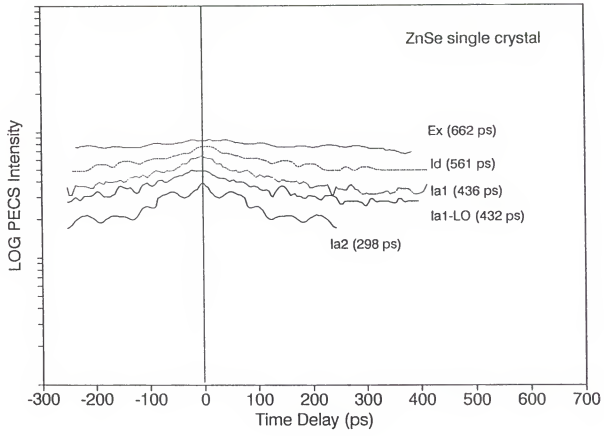

Figure 7-6 time-resolved PL spectra of ZnSe crystal at 10K.

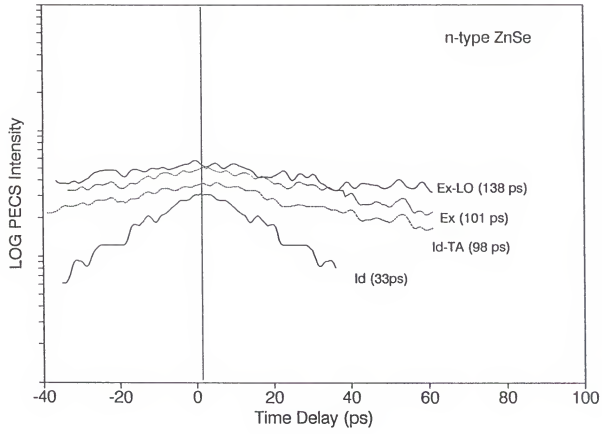

Figure 7-7 time-resolved PL spectra of n-type ZnSe film at 10K.

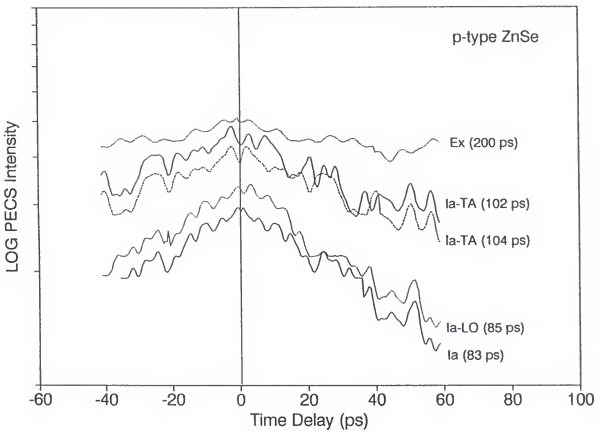

Figure 7-8 time-resolved PL spectra of p-type ZnSe film at 10K.

proportional to the total number of free excitons, but the no-phonon exciton line results only from fraction of the diffusing exciton cloud that reaches the sample surface and transmitted as photons. Thus, the longer lifetime of the LO replica, which is the true lifetime of the free exciton population, reflects this diffusion away from the sample surface.

The longer decay lifetimes exhibited by free excitons as compared to bound excitons can be explained in terms of the giant oscillator strength theory developed by Rashba et al. (237). The transition oscillator strength is proportional to the ratio of unit cell volume and exciton volume. For free exciton, $f=(a/a_{ex})^3$, for bound excitons, since they are more localized, the exciton volume is much reduced and can be approximated by

$f_{BE}=(a_{ex}/a)^3 f$,

where a_{ex} is the exciton Bohr radius, a is the lattice parameter, f is the free exciton oscillator strength. For ZnSe, $(a_{ex}/a)^3 \approx 10^4$. Thus the oscillator strength of bound excitons is much higher than that of the exciton. Since exciton decay lifetime is given by the equation (228)

$$\tau=\frac{2\pi\epsilon_0 m_0 c^3}{ne^2\omega^2 f}$$

then $\tau \propto 1/f$. Bound excitons having very large oscillator strength are expected to exhibit very short lifetimes while free excitons having smaller oscillator strength are expected to have very long lifetimes. However, in real material, the difference in lifetimes of free excitons and bound excitons is much reduced due to free exciton

trapping by impurities. The giant oscillator strength of bound excitons explains the strong and narrow bound exciton emission lines observed in GaAs at impurity concentration as low as 10^{-10} cm^{-3}.

Unlike free excitons, the bound excitons are not polaritons. The LO-phonon emissions result from the spontaneous recombination of bound excitons, so LO-phonon replica of bound excitons should follow exactly same decay behavior as the no-phonon bound excitons. This is indeed what we observed.

In the spectrum of the bulk crystal, both donor and acceptor bound exciton lines exist. The data show that the decay lifetime of acceptor bound exciton I_{a1} is shorter than that of the donor-bound exciton I_d. This behavior can be explained also in terms of transition oscillator strength. The localization energy of acceptor bound exciton I_{a1} is larger than that of the donor bound exciton I_d, as reflected from their relative positions to the free exciton line, so I_{a1} is more localized and has a smaller exciton volume than I_d. Consequently, oscillator strength for I_{a1} (a/a_{ex}) is larger than that of I_d and I_{a1} exhibits a shorter decay lifetime. Similarly, I_{a2}, which is more localized than I_{a1}, exhibits a shorter lifetime.

In the p-type film, two features appear around the shoulders of the acceptor-bound exciton line at high excitation densities as shown in figure 7-4. They are equally spaced around the acceptor emission line in energy. Their temporal behaviors were resolved and shown in figure 7-8. Their rather long decay times exclude their origin as bound excitons. We attribute them to forbidden transverse acoustic phonon (TA) replica. The energy position of each line with respect to the

acceptor exciton is about 6.9meV, corresponding to the TA phonon energy in ZnSe. The mechanism can be understood as follows: at high carrier densities, both carrier-carrier scattering and carrier phonon scattering contribute to the carrier thermalization process. However, carrier-carrier scattering only causes the redistribution of carrier energies but doesn't take energy out of the system. To lose energy, carriers have to interact with phonon modes. For LO phonons, the interaction is the long-range Frohlich interaction, whereas for acoustic phonons, both the deformation-potential coupling and the piezoelectric coupling have to be taken into account, which is much weaker than the Frohlich interaction. Thus, the relaxation time for acoustic emission is substantially longer. Since the carrier-acoustic phonon interaction is weak, this emission only appears at high carrier densities where other carrier thermalization channels besides LO-phonons come into play. The acoustic phonon emission also shows up on the n-type sample spectrum and can be explained similarly.

Comparing the exciton decay lifetimes of the crystal with those of epitaxial films, it is found that the crystal exhibits much longer lifetimes than epitaxial films, which is consistent with the room temperature result. The reason is due to the presence of non-radiative recombination centers in films such as stacking faults and dislocations resulting from the lattice mismatch during epitaxial MBE growth. The crystal, however, is not epitaxially grown and has a lower concentration of this type of non-radiative centers. Although there are impurities present in the crystal, as evidenced in the PL spectra by several bound exciton emission lines, these

impurities are shallow and radiative, and have far less impacts on carrier lifetimes than non-radiative centers. The structural aspects of these samples were verified by TEM and the films indeed show a larger density of Shockley-Reed type dislocations as well as stacking faults.

To conclude this section, low temperature dynamics of various processes such as free and bound excitons, LO-phonon replica were investigated through both steady-state and transient luminescence experiments. The lifetimes of bound excitons are found to be shorter than those of the free excitons and the reason was attributed to the higher oscillator strength of bound excitons due to the enhanced localization. The free exciton dynamics reflect their polariton nature. The carrier-carrier interaction was found to play a role on carrier relaxation process at high excitation densities.

CHAPTER 8
CONCLUSIONS AND FUTURE WORK

Conclusions of Carrier Dynamics Study

In this study, we have investigated carrier dynamics in CdZnSe/ZnSe multiple quantum well structures, ZnSe epitaxial films, and ZnSe bulk crystal at both room temperature and low temperatures. For quantum well structures, exciton process dominates at both room temperature and low temperature due to the large exciton binding energy as a result of quantum confinement effect. The exciton dynamics was found to be consistent at both room and low temperatures: the cross-coupling effect caused by the presence of finite potential barriers dominates over the interband direct recombination on the exciton dynamics. For the samples with the same well thickness but different barrier thicknesses (50/50Å, 50/100Å, 50/200Å), the sample with the largest barrier thickness 200 Å was found to exhibit the longest exciton lifetime and highest emission intensity. For the samples with the same barrier thickness but different well thicknesses (25/100Å, 50/100Å, 100/100Å), the sample with well thickness (25Å) about one half of Bohr radius was found to decay very fast due to significant wavefunction penetration into barriers when the electron states are too close to the barrier potential as a result of strong confinement; the sample with well thickness (100Å) larger than Bohr diameter was found to decay fast also due to strong cross-coupling effect present when the

density of states is close to continuous bulk-like; The sample with well thickness in between exhibits the longest exciton decay and highest luminescence intensity because the confinement effect is not too strong to cause significant carrier penetration into barriers and in the meantime is not too weak to cause significant cross-coupling between wells. The dominance of cross-coupling effect on exciton decay was further verified by carrier tunneling study.

The most significant result from low temperature carrier dynamics study of CdZnSe/ZnSe MQWs is the observation of biexcitons. A biexciton consists of two excitons with opposite internal spins bound by the Coulomb interaction. The formation of a biexciton was confirmed by its luminescence intensity dependence on excitation power, its very fast decay lifetime, polarization transition dependence, and its reverse Boltzmann lineshape. The biexciton binding energy in these structures was found to be about 14meV, much larger than that of GaAs. Unlike the dynamics of excitons, which is dominated by cross-coupling effect, biexciton dynamics is dominated by the interband transition oscillator strength. Consequently, the sample has the highest oscillator strength decays the fastest. Biexciton dynamics reflect the more localized nature of biexcitons as compared to excitons, This conclusion is also verified through the comparison of enhancements in binding energies of excitons and biexcitons in QWs over the bulk.

The formation of biexcitons has a profound effect on the nonlinear optical properties of CdZnSe/ZnSe MQW structures. Biexcitons are more localized and have stronger oscillator strength, thus nonlinearity associated with biexciton

transition is much higher. The density of biexcitons goes as the square of that of excitons while the decay lifetime is twice as fast as excitons, so the biexciton population can build up much faster than that of excitons to allow population inversion and subsequent lasing to occur. Based on the characteristics of CdZnSe/ZnSe MQW diode lasers operating at cryogenic temperatures, we propose biexciton gain as the lasing mechanism in these lasers. The advantages of biexciton gain include the lower electron-hole pair density required to reach the lasing threshold than that in conventional degenerate electron-hole plasma picture and higher internal efficiency.

Carrier lifetime dependence on temperature was also conducted on the MQWs to determine the inhomogeneous linewidth and phonon-exciton interaction strength. The inhomogeneous linewidth was found to be about 5meV, much larger than that of high quality GaAs, indicating the material quality still needs to be improved. The exciton-phonon interaction constants were found to be very large as expected, since ZnSe has more polar structure and the Frolich interaction is very strong. These parameters are very important in understanding the lasing behavior of these structures. Due to current concern on device lifetimes and degradation, optical degradation was conducted to investigate the degradation mechanism through luminescence and carrier lifetime behaviors. Both luminescence and lifetime data show two exponential regimes: initial fast degradation regime and subsequent slow and saturated regime. The data were consistent with the formation

kinetics of dislocations and dislocation networks in the QW regions that confirmed by TEM structural studies.

Hot phonon effect on carrier cooling was also observed in MQW structures. The increase of exciton decay lifetime was observed when nonequilibrium hot phonons are created by injection of high density of carriers well above the electron ground state.

Finally, the band state calculation of the MQW structure using envelope wavefunction approximation approach with tight-binding expansion was a success, from the fact that excellent agreement between experimental data and theoretical calculations was achieved.

For epitaxial films and bulk crystal, the room temperature dynamics were dominated by free carriers at the bandedge. The carrier lifetimes for the films were found to be dominated by carrier trapping based on the fact that carrier lifetime in doped film doesn't decrease with doping level in proportion. The carrier lifetimes of epitaxial films are much shorter than the crystal because of the presence of non-radiative dislocations and stacking faults in films introduced from MBE growth due to the lattice mismatch.

The low temperature dynamics of ZnSe films and crystal were dominated by free and bound excitons as well as their phonon replicas. The temporal behavior of each process reflects the intrinsic nature of the process and allows us to identify it accurately. The bound excitons were found to decay faster than the free excitons and the reason was attributed to the giant oscillator strength associated with bound

excitons. The polariton nature of free excitons was manifested through the small difference in lifetime between the free exciton and its phonon replicas.

Future Work

Future work includes investigation of coherent dynamics by time-resolved coherent spectroscopy such as degenerate four-wave mixing and coherent Raman scattering. Coherent dynamics probed by four-wave mixing yields direct information on the dephasing process of electronic polarization just after the photoexcitation and before carrier recombination, which is extremely useful to determine the exciton nonlinearity and the role of disorders and traps on exciton dynamics. For our MQW samples, the exciton dephasing dynamics can be used to verify the role of cross-coupling effect, since interband recombinations are not involved in the coherent process and the dephasing time is a direct measure of carrier tunneling effect. Also, since the dephasing time is directly related to the homogeneous linewidth, its temperature dependence will allows us to determine the exciton-phonon (both acoustic and optical phonon) interactions accurately.

Coherent Raman spectroscopy yields information on phonon dynamics. Phonon modes in QW structures are modified from the bulk due to quantum confinement effect, the dynamics thus are expected to be different from the bulk. The understanding of phonon dynamics will allow us to gain insights into carrier thermalization processes by phonon scatterings.

Asymmetric MQW structures (wells have different thicknesses or compositions within one MQW structure) will be designed such that the electron

energy levels of the adjacent wells are the same while the hole energy levels are different. When the optical excitation energy is tuned to excite smaller gap well only, the luminescence signal due to recombination in the bigger gap well directly measures the carrier tunneling time.

Doped MQW structures will be fabricated to study many-body physics such as the effect of carrier-plasma, phonon-plasma interactions on carrier relaxation dynamics. These interactions are very important for designing and understanding these structures for diode laser and LED applications.

Temporal resolution of current Ti:Sapphire laser system will be improved by using a combination of grating and prism pulse compression scheme so that processes occurring on a femtosecond scale can be probed. Processes of fundamental research interest include carrier thermalization processes via carrier-carrier scattering, carrier-impurity scattering, and carrier-phonon scattering in both MQWs and bulk. The fundamental understanding of carrier thermalization has to be achieved before ultrafast response devices such as quantum interference switches and resonant tunneling hot-electron transistors can be realized.

For real device in-situ characterizations, time-resolved technique such as time-of-flight measurements and all-optical technique can be used to study the time evolution of minority carrier drift velocity or carrier mobility. Optical gain spectroscopy can be used to evaluate performance of diode lasers.

REFERENCES

1. Pankove, Jacques I. ,Optical Processes in Semiconductors, Dover Publications, Inc. New Yrok, 1971

2. Shah, Jagdeep, Hot Carriers in Semiconductor Nanostructures—Physics and Application, Academic Press, San Diego, 1992

3. Petersen, C. L, & Lyon, S. A., Phys. Rev. Lett. 65, 760 (1990)

4. Elsaesser, T, Shah, J., Rota, L., Lugli, P., Phys. Rev. Lett. 66, 1757 (1991)

5. Hohenester, U., Supancic, P., Kocevar, P., Zhou, X., Kutt, W., Kurz, H., Phys. Rev. B 47, 13233 (1993)

6. Kane, M., Sun, K., Lyon, S., Semiconductor Sci. & Tech. 9, 697 (1994)

7. Gong, T., Young, J., Wicks, G., Kelly, P., Fauchet, P., Semiconductor Sci. & Tech. 9, 459 (1994)

8. Weisbuch, C., Vinter, B., Quantum Semiconductor Structures, Academic Press, San Diego, 1991

9. Yokoyama, N., Imamura, K., Ohnishi, T., Nishi, H., Muto, S., Kondo, K., and Hiyamizu, S., Japan. J. Appl. Phy. 23, L311 (1985)

10. Kaiser, W. Ultrashort Laser Pulses and Applications, Springer-Verlag, Topics in Applied Physics, vol.60, 1988

11. Levenson, M. D., Kano, S. S., Introduction to Nonlinear Laser Spectroscopy, Academic Press, San Diego,1988

12. Oudar, J. L., Shen, Y. R., Phys. Rev. 22, 1141 (1980)

13. Ye, P., Shen, Y. R., Phys. Rev. 25, 2183 (1982)

14. Fisher, R. A. Optical Phase Conjugation, Academic Press, San Diego, 1983

15. Yajima, T., Taira, Y., J. Phys. Soc. Jpn. 47, 1620 (1979)

16. Yariv, A., Introduction to Optical Electronics, Holt, Rinehardt, Winston series 1976

17. Honold, A., Schultheis, L., Kuhl, J., Tu, C. W., Appl. Phys. Lett. 52, 2105 (1988)

18. Haug, H., Banyai, L., Optical Switching in Low-Dimensional Systems, NATO ASI series, vol 194, Plenum Press, New York, 1989

19. Rodrigues, R., Juen, S. A., Lamprecht, K. F., Hopfel, R. A., Semiconductor Sci. & Techno. 9, 456-458 (1994)

20. Alfano, R. R, Semiconductors Probed by Ultrafast Laser Spectroscopy, vol. 2, Academic Press, San Diego, 1988

21. Ippen, E., Shank, C., Appl. Phy. Lett. 26, 92 (1975)

22. Ho, P. P, Alfano, R. R., Phy. Rev. A 21, 1730 (1979)

23. Schiller, N., Alfano, R. R., 15th Inter. Conf. Photography and Photonics of the SPIE, SPIE proceedings, 1982

24. Sibbett, W., Niu, H., Baggs, M. R., Rev. Sci. Instrum. 53, 758 (1982)

25. Ware, W. R., Creation and Detection of the Excited States, vol. I, 213-302. Marcel Dekker, New York, 1971

26. Kinoshita, S., Kushida, T., Rev. Sci. Instrum. 53, 469 (1982)

27. Rosen, D., Doukas, A. G., Budansky, Y., Katz, A., Alfano, R. R., Appl. Phys. Lett. 39, 935 (1981)

28. Mahr, H., Sagan, A. G., Appl. Phys. Lett. 39, 269 (1981)

29. Mahr, H., Sagan, A. G., Hememway, C. P., Frigo, N. J., Chem. Phys. Lett. 79, 3 (1981)

30. Olsson, A., Erskine, D. J., Xu, J. Y., Schremer, A., Tang, C. L., Appl. Phys. Lett. 47, 659 (1982)

31. Tanaka, K., Ohtake, H., Nansei, H., Suemoto, T., IQEC'94 (Int. Conf. Quantum Electronics, OSA), 9, QMF 20, Anaheim, CA (1994)

32. Tanaka, K., Ohtake, H., Nansei, H., Suemoto, T., Phys. Rev. Lett. 71, 1935 (1993)

33. Son, J., Rhee, J., Norris, T. B., Whitaker, J. F., IQEC'94 (Int. Conf. Quantum Electronics, OSA), 9, QMF 20, Anaheim, CA (1994)

34. Van Exter, M., Fattinger, Ch., Grischkowsky, D., Appl. Phys. Lett. 55, 337 (1989)

35. Son, J., Sha, W., Kim, J., Norris, T. B., Whitaker, J. F., Mourou, G. A., Appl. Phys. Lett. 63, 923 (1993)

36. Goldman, J. R., Prybyla, J. A., IQEC'94 (Int. Conf. Quantum Electronics, OSA), 9, QMF 20, Anaheim, CA (1994)

37. Rappen, T., Peter, U., Schafer, W., Wegener, M., IQEC'94 (Int. Conf. Quantum Electronics, OSA), 9, QMF 20, Anaheim, CA (1994)

38. Bennhardt, D., Thomas, P., Eccleston, R., Mayer, E. J., Kuhl, J., Phys. Rev. B47, 13485 (1993)

39. Shah, J., Iafrate, G. J., Proceedings of the Fifth International Conference on Hot Carriers in Semiconductors, Boston, Massachussetts, 1987

40. Gupta, S., Whitaker, J. F., Mourou, G. A., IEEE Journal. Quan. Elec. 28, 2464 (1992)

41. Kash, J., Tsang, J., Hvam, J., Phys. Rev. Lett. 54, 2151 (1985)

42. Kash, J. A., Phys. Rev. B. 40, 3455 (1989)

43. Zhou, X. Q., Ruhle, W. W., Schullatz, P., Kocevar, P., Van Driel, H. M., Ploog, K., Semicond. Sci. Technol. 9, 704 (1994)

44. Zhou, X. Q., Van Driel, H. M., Ruhle, W. W., Gogolak, Z., Ploog, K., Appl. Phys. Lett. 61, 3020 (1992)

45. Potz, W., Kocevar, P., in Hot Carriers in Semiconductor Nanostructures, ed J. Shah, P. 87, Academic Press, 1992

46. Haase, M. A., Qui, J., DePuydt, J. M., Cheng, H., Appl. Phys. Lett. 59, 1272 (1991)

47. Wang, S. Y., Hauksson, I., Simpson, J., Stewart, H., Adams, S. J., Wallace, J., Kawakami, Y., Prior, K., Cavenett, B., Appl. Phys. Lett. 61, 506 (1992)

48. Wherrett, B. S., Semicond. Sci. Technol. 6, A65 (1991)

49. Park, R. M., Troffer, M. B., Roulean, C. M., DePuydt, J. M., Haase, M. A., Appl. Phys. Lett. 57, 2127 (1990)

50. Ohkawa, K., Karasawa, T., Mitssuyu, T., J. Cryst. Growth 111, 797 (1991)

51. Yang, X. H., Hays, J., Shan, W., Song, J. J., Cantwell, E., Aldridge, J., Appl. Phys. Lett. 59, 1681 (1991)

52. Zmudzinski, C. A., Guan, Y., Zory, P. S., IEEE Photon. Tech. Lett. 2, 94 (1990)

53. Guha, S., Cheng, H., DePuydt, J. M., Haase, M. A., Qiu, J., Wu, B., Hofler, G. E., IQEC'94 (Int. Conf. Quantum Electronics, OSA proceedings), 9, CTu20 (1994)

54. Talas, J. J., Allen, J. W., Semicond. Sci. Technol. 6, A138 (1991)

55. Milward, J. R., Ji, W., Kar, A. K., Pidgeon, C. R., Wherrett, B. S., Appl. Phys. Lett. 69, 2708 (1990)

56. Bolger, J. A., Kar, A. K., Wherrett, B. S., Prior, K. A., Simpson, J., Wang, S. Y., Cavenett, B. C., Appl. Phys. Lett. 63, 571 (1993)

57. Hauksson, I. S., Simpson, J., Wang, S. Y., Prior, K. A., Cavenett, Appl. Phys. Lett. 61, 2208 (1992)

58. Zheng, J., Allen, J. W., Spence, D. E., Sleat, W. E., Sibbett, W., Appl. Phys. Lett. 62, 63 (1992)

59. Dumke, W. P., Phys. Rev. 132, 1998 (1963)

60. Massa, J. S., Buller, G. S., Walker, A. C., Simpon, J., Prior, K. A., Cavenett, B. C., Appl. Phys. Lett. 64, 589 (1994)

61. Charbonneau, S., Thewalt, M., Isshiki, M., Masumoto, K., Solid State Comm. 67, 187 (1988)

62. Steiner, T., Thewalt, M., Bhargava, R. N., Solid State Comm. 56, 933 (1985)

63. Rashba, E. I., Gurgenishvilli, G. E., Sov. Phys. Solid State, 4, 759 (1962)

64. Sanders, G. D., Chang, Y., Phys. Rev. B28, 5887 (1983)

65. Miyao, M., Nakagawa, K., Jpn. J. Appl. Phys. 33, 3791, (1994)

66. Karunasiri, G., Jpn. J. Appl. Phys. 33, 2401 (1994)

67. Glaser, E. R., Kennedy, T. A., Klein, P. B., Godbey, D. J., Thompson, P. E., Jpn. J. Appl. Phys. 33, 2357 (1994)

68. Geiler, H. D., Kruegel, S., Nuetzel, J., Friess, E., Abstreiter, G., Appl. Surface Sci. 63, 260 (1993)

69. Gobel, E. O., Jung, H., Kuhl, J., Ploog, K., Phys. Rev. Lett. 51, 1588 (1983)

70. Feldmann, J., Peter, G., Gobel, E. O., Dawson, P., Moore, K., Foxon, C., Elliott, R. J., Phys. Rev. Lett. 59, 2337 (1987)

71. Kim, D., Shah, J., Cunningham, J., Damen, T., Schafer, W., Hartmann, M., Schmitt-Rink, S., Phys. Rev. Lett. 68, 1006 (1992)

72. Schultheis, L., Kuhl, J., Honold, A., Tu, C., Phys. Rev. Lett. 57, 1635 (1986)

73. Schultheis, L., Kuhl, J., Honold, A., Tu, C., Phys. Rev. Lett. 57, 1797 (1986)

74. Sucha, G., Bolton, S. R., Chemla, D. S., Sivco, D. L., Cho, A., Appl. Phys. Lett. 65, 1486 (1994)

75. Smith, G. O., Mayer, E. J., Kuhl, J., Ploog, K., Solid State Comm. 92, 325 (1994)

76. Kim, D. S., Fischer, A. J., Hays, J., Shan, W., Song, J. J., Eason, D. B., Ren, J., Schetzina, J. F., Appl. Phys. Lett. 65, 1534 (1994)

77. Becker, P. C., Lee, D., Barros, M., Johnson, A., Prossor, A., Feldman, R., Austin, R., Behringer, R. E., IEEE J. Quan. Elec. 28, 2535 (1992)

78. Schmitt-Rink, S., Chemla, D. S., Miller, D.A.B., Phys. Rev. B 22, 671 (1988)

79. Ding, J., Hagerott, M., Kelkar, P., Nurmikko, A. V., Grillo, D. C., He, L., Han, J., Gunshor, R. L., J. Cryst. Growth, 138, 719 (1994)

80. Ding, J., Jeon, H., Ishihara, T., Nurmikko, A. V., Luo, H., Samarth, N., Furdyna, J., Surface Science, 267, 616 (1992)

81. Kreller, F., Schulzgen, A., Henneberger, F., Puls, J., Streller, U., Solid State Commun. 37, 1137 (1994)

82. Stevens, C. J., Taylor, R. A., Ryan, J. F., Cingolani, R., Dabbicco, M., Ferrara, M., Suemune, I., Semicond. Sci. Technol. 9, 762 (1994)

83. Frensley, W. R., Rev. Mod. Phys. 62, 745 (1990)

84. Tsuchiya, M., Matsusue, T., Sakaki, H., Phys. Rev. Lett. 59, 2356 (1987)

85. Norris, T. B., Song, X., Schafe, W., Eastman, L., Wicks, G., Mourou, G., Appl. Phys. Lett. 54, 60 (1989)

86. Jackson, M. K., Johnson, M. B., Chow, D. H., McGill, T. C., Nieh, C. W., Appl. Phys. Lett. 54, 552 (1989)

87. Whittaker, J. F., Mourou, G. A., Sollner, T., Goodhue, W. D., Appl. Phys. Lett. 53, 385 (1988)

88. Tackeuchi, A., Japan. J. Appl. Phys. 28, L1098 (1989)

89. Tada, T., Yamaguchi, A., Ninomiya, T., Uchiki, H., Kobayashi, T., Yao, T., J. Appl. Phys. 63, 5491 (1988)

90. Norris, T. B., Vodjani, N., Vinter, B., Weisbuch, C., Phys. Rev. B 40, 1074 (1989)

91. Oberli, D. Y., Shah, J., Deveaud, B., Damen, T. C., in Proc. Topical Meeting on Picosecond Electronics and Optoelectronics (ed. Sollner and Bloom, Opt. Soc. America, Washington, DC, 1989), p.94

92. Oberli, D. Y., Shah, J., Damen, Kopf, R. F., Kuo, J. M., Henry, J. E., in OSA Proceedings on Picosecond Electronics and Optoelectronics (ed. Sollner and Bloom, 1989), p.111

93. Oberli, D. Y., Shah, J., Damen, T. C., Tu, C. W., Miller, D. A.B., Opt. Soc. Am. Tech. Digest Ser. 10, 272 (1989)

94. Oberli, D. Y., Shah, J., Damen, Chang, T. Y., Tu, C. W., Miller, D. A. B., Henry, J. E., Kopf, R. F., Sauer, N., DiGiovanni, A. E., Phys. Rev. B 40, 3028 (1989)

95. Deveaud, B., Clerot, F., Chomettr, A., Regreny, A., Ferreira, R., Bastard, G., Europhys. Lett. 11, 367 (1990)

96. Deveaud, B., Chomettr, A., Clerot, F., Auvray, P., Regreny, A., Ferreira, R., Bastard, G., Phys. Rev. B 42, 7021 (1990)

97. Alexander, M. G. W., Nido, M., Ruhle, W. W., Kohler, K., Phys. Rev. B 41, 12295 (1990)

98. Nido, M., Alexander, M. G. W., Ruhle, W. W., Kohler, K., in Proc. SPIE, 1268, 177 (1990)

99. Tackeuchi, A., Inata, T., Muto, S., Miyauchi, E., Japan. J. Appl. Phys. L750 (1989)

100. Deveaud, B., Lambert, B., Chromette, A., Clerot, F., Regreny, A., Shah, J., Damen, T. C., Miller, D. A. B., Sermage, B., in Optical Switching in Low-Dimensional Systems (ed. Haug and Banyai), Plenum, 1989

101. Leo, K., Shah, J., Gordon, J. P., Damen, T. C., Miller, D. A. B., Tu, C. W., Cunningham, J. E., Phys. Rev. B 42, 7065 (1990)

102. Leo, K., Shah, J., Gordon, J. P., Damen, T. C., Miller, D. A. B., Tu, C. W., Cunningham, J. E., Henry, J. E. in Proc. SPIE Conf. on QW and Superlattice Physics III (ed. Dohler, Koteles, and Schulman, SPIE, 1990), 1283, p.35

103. Van Wees, B. J., Van Houton, H., Beenakker, C. W. J., Williamson, J. G., Kouwenhoven, L. P., Van der Marel, D., Foxon, C. T., Phys. Rev. Lett. 60, 848 (1988)

104. Wharam, D. A., Thornton, T. J., Newbury, R., Pepper, M., Ahmed, H., Frost, J., Hasko, D., Peacock, D., Ritchie, D., Jones, G., J. Phys. C 21, L209 (1988)

105. Van Houton, H., van Wees, B. J., Mooij, J. E., Beenakker, J. G., Williamson, J. G., Foxon, C. T., Europhys. Lett. 5, 721 (1988)

106. Spector, J., Stomer, H. L., Baldwin, K. W., Pfeiffer, L. N., West, K. W., Surf. Sci. 228, 283 (1990)

107. Heiblum, M., Sivan, U., in Hot Carriers in Semiconductor Nanostructures (ed. Shah, J. Academic, 1992), p. 411

108. Chelikowsky, J. R., Cohen, M. L., Phys. Rev. B 14, 556 (1976)

109. Pollak, F. H., in II-VI Semiconductoring Compounds, edited by D. G. Thomas (Benjamin, New York, 1967)

110. Lowisch, M., Kreller, F., Puls, J., Henneberger, Phys. Stat. Sol. (b), 188, 165 (1995)

111. Nurmikko, A. V., Gunshor, R. L., IEEE J. Quan. Elec. 30, 619 (1994)

112. DiLorenzo, J. V., Niehaus, W. C., Cho, A. Y., J. Appl. Phys. 50, 951 (1979)

113. Schneider, M. V., Linke, R. A., Cho, A. Y., Appl. Phys. Lett. 31, 219 (1977)

114. Cho, A. Y., Dixon, R. W., Casey, H. C., Hartman, R. L., Appl. Phys. Lett. 28, 501 (1976)

115. Cho, A. Y., Molecular Beam Epitaxy, AIP Press, New York, 1994

116. Foxon, C. T., Harvey, J. A., Joyce, B. A., Surf. Sci. 44, 69 (1974)

117. Tomomura, Y., Hirata, S., Okumura, T., Kitagawa, M., Suzuki, A., Takiguchi, H., J. Cryst. Growth, 138, 764 (1994)

118. Shank, C. V., in Ultrashort Laser Pulses (ed. Kaiser, Springer, 1988), p. 5

119. Hargrove, L. E., Fork, R. L., Pollack, M. A., Appl. Phys. Lett. 5, 4 (1964)

120. DeMaria, A. J., Stetser, D. A., Heyman, H., Appl. Phys. Lett. 8, 22 (1966)

121. Fork, R. L., Greene, B. I., Shank, C. V., Appl. Phys. Lett. 38, 671 (1981)

122. Coherent Mira Model 900 Laser Operator's Manual, Coherent, Inc. San Jose, chapter 7, 1993

123. Coherent Rega Model 9000 Laser Operator's Manual, Coherent, Inc. San Jose, chapter 8, 1994

124. Coherent OPA Model 9400 Operator's Manual, Coherent Inc., San Jose, chapter 6, 1995

125. Johnson, M. B., McGill, T. C., Hunter, A. T., J. Appl. Phys. 63, 2077 (1988)

126. Ippen, E. P., Shank, C. V., Techniques of measurement, in Ultrafast Light Pulses, S. L. Shapiro, ed. Springer-Verlag, 1977, p. 108

127. Chemla, D. S., Miller, D. A. B., Schmitt-Rink, S., Optical Properties of Quantum Wells in Nonlinearities and Instabilities in Semiconductors, Academic, 1988

128. Bastard, G., Brum, J. A., IEEE J. Quantum Electron. QE-22, 1625 (1986)

129. Bastard, G., Phys. Rev. B 24, 5693 (1981)

130. Kane, E. O., J. Phys. Chem. Solids 1, 249 (1957)

131. Bohm, D., Qauntum Mechanics, Prentice-Hall, 1951

132. Altarelli, M., Phys. Rev. B 28, 842 (1983)

133. Altarelli, M., in Heterojunctions and Semiconductor Superlattices (ed. Allen, G., Bastard, G., Boccara, N., Lannoo, M., and Voor, M., Springer, 1986), p.12

134. Luttinger, J. M., Phys. Rev. 102, 1030 (1956)

135. Fasolino, A., Altarelli, M., Springer Ser. Solid-State Sci. 59, 176 (1984)

136. Maan, J. C., Fasolino, A., Belle, G., Altarelli, M., Ploog, K., Physica (Amsterdam) 127B, 426 (1984)

137. Nedozerov, S. S., Fiz. Tverd. Tela 12, 2269 (1970)

138. Ando, T., Fowler, A. B., Stern, F., Rev. Mod. Phys. 54, 437 (1982)

139. Shinada, M., Sugano, S., J. Phys. Soc. Jpn. 21, 1936 (1966)

140. Stern, F., Howard, W. E., Phys. Rev. 163, 816 (1967)

141. Greene, R. L., Bajaj, K. K., Phelps, D. E., Phys. Rev. B 29, 1807 (1984)

142. Knox, R. S., Theory of Excitons, Solid State Phys., Suppl.5. Academic Press, 1963

143. Phillips, J. C., Bonds and Bands in Semiconductors, Academic, 1973

144. Chemla, D. S., Miller, D. A. B., J. Opt. Soc. Am. B2, 1155 (1985)

145. Esaki, L., Tsu, R., IBM J. Dev. 14, 61 (1970)

146. Schulman, J. N., McGill, T. C., Phys. Rev. B 19, 6341 (1979)

147. Tsu, R., Esaki, L., Appl. Phys. Lett. 22, 562 (1973)

148. Dingle, R., Gossard, A. C., Wiegmann, W., Phys. Rev. Lett. 34, 1327 (1975)

149. Bastard, G., Acta Electron. 25, 147 (1983)

150. Shahzad, K., Olego, D., Van de Walle, C., Phys. Rev. B38, 1417 (1988)

151. Gutowski, J., Presser, N., Kudlek, G., Phys. Stat. Sol. (a) 120, 11 (1990)

152. Pikus, G. E., Bir, G. L., Sov. Phys.–Solid State 1, 1502 (1959)

153. Hensel, C. J., Feher, G., Phys. Rev. 129, 1041 (1963)

154. Van de Walle, C. G., Martin, R. M., Phys. Rev. B34, 5621 (1986)

155. Tsay, Y. F., Mitra, S. S., Bendow, B., Phys. Rev. B 10, 1476 (1974)

156. Bairamov, B. H., Gol'tsev, Toporov, V. V., Laiho, R., Levola, T., Phys. Rev. B33, 5875 (1986)

157. Kurakake, H., IEEE J. Quantum Electron. 30, 909 (1994)

158. Chand, N., Chu, S., Dutta, N., IEEE J. Qauntum Electron. 30, 424 (1994)

159. Bastard, G., Phys. Rev. B24, 5693 (1981)

160. Madelung, O., Landolt-Bornstein New Series III/22a, Springer-Verlag, 1991

161. Lozykowski, H. J., Shastri, V. K., J. Appl. Phys. 69, 3235 (1991)

162. Kolodziejski, L., Lu, K., Ho, E., Coronado, C. A., Fisher, P. A., Petrich, G. S., in Proc. Int. Conf. on II-VI Compounds, 1993

163. Gustowski, J., Diessel, A., Neukirch, U., Weckendrup, D., Behr, T., Jobst, B., Hommel, D., Phys. Stat. Sol. (b) 187, 423 (1995)

164. Pelekanos, N., Phys. Rev. B45, 6037 (1992)

165. Adachi, S., Taguchi, T., Phys. Rev. B 43, 9569 (1991)

166. Nurmikko, A. V., Gunshor, R. L., IEEE J. Quantum Electron. 30, 619 (1994)

167. Landsberg, T., Recombination in Semiconductors, Cambridge University Press, 1991

168. Ding et al. in Gain and dynamics in ZnSe quantum wells, in Proc. Int. Conf. II-VI Compounds, Newport RI, September, 1993

169. Ruhle, W. W., in Proc. 20th Int. Conf. on Physics of Semiconductors, (ed. Anastassakis and Joanopoulos, World Scientific, 1990), p. 1226

170. Schmitt-Rink, S., Chemla, D. S., Miller, D. A. B., Advances in Physics, 38, 89 (1989)

171. Greene, R. L., Bajaj, K. K., Solid State Commun. 45, 831 (1983)

172. Greene, R. L., Bajaj, K. K., Phelps, D. E., Phys. Rev. B 29, 1807 (1984)

173. Herbert, D. C., Rorison, J. M., Solid State Commun. 54, 343 (1985)

174. Weisbuch, C., Miller, R. C., Dingle, R., Gossard, A. C., Wiegmann, W., Solid State Commun. 37, 219 (1981)

175. Lampert, M. A., Phys. Rev. Lett. 1, 450 (1958)

176. Wehner, R. K., Solid State Commun. 9, 457 (1969)

177. Brinkman, W. F., Rice, T. H., Bell, B., Phys. Rev. 8, 1570 (1973)

178. Shionoya, S., Saito, H., Hanamura, E., Akimoto, O., Solid State Commun. 12, 223 (1973)

179. Charbonneau, S., Optical Engineering, 28, 1101 (1989)

180. Citrin, D. S., Phys. Rev. B50, 17655 (1994)

181. Lovering, D. J., Phillips, R. T., Denton, G. J., Smith, G. W., Phys. Rev. Lett. 68, 1880 (1992)

182. Pantke, K. H., Oberhauster, D., Lyssenko, V. G., Hvam, J. M., Phys. Rev. B 47, 2413 (1993)

183. Albrecht, T. F., Schulze, Koch, M., Meier, T., Bott, K., Feldmann, J., QELS'95 (Int. Quant. Elect. Conf., OSA proceedings), QFB2, Baltimore, MD, 1995

184. Phillips, R. T., Lovering, D. J., Denton, G. J., Smith, G. W., Phys. Rev. B 45, 4308 (1992)

185. Mysyrowicz, A., Gun, A., Levy, J. B., Biras, R., Nikitine, A., Phys. Rev. Lett. 26A, 615 (1968)

186. Nikitine, S., in Excitons at High Density, (ed. Haken and Nikitine, Springer, 1975)

187. Bott, K., Heller, O., Bennhardt, D., Cundiff, S. T., Thomas, P., Mayer, E. J., Smith, G. O., Eccleston, R., Kuhl, J., Phys. Rev. B48, 17418 (1993)

188. Smith, G. O., Mayer, E. J., Kuhl, J., Ploog, K., Solid State Commun. 92, 325 (1994)

189. Wang, H., Shah, J., Damen, T. C., Pfeiffer, L. N., Solid State Commun. 91, 869 (1994)

190. Akimoto, O., Hanamura, E., Solid State Commun. 10, 253 (1972)

191. Hanamura, E., Solid State Commun. 12, 951 (1973)

192. Ivanov, A. L., Haug, H., Phys. Rev. B48, 1490 (1993)

193. Ivanov, A. L., Haug, H., Phys. Rev. Lett. 74, 438 (1995)

194. Wang, H., Shah, J., Damen, T. C., Pfeiffer, L. N., QELS'95 (Int. Quan. Electron. Conf. OSA proceedings), QThc4, 16, Baltimore, MD, 1995

195. Lowisch, M., Kreller, F., Puls, J., Henneberger, F., Phys. Stat. Sol. (b) 188, 165 (1995)

196. Yamada, Y., Mishina, T., Masumoto, Y., Kawakami, Y., Yamaguchi, S., Ichino, K., Fujita, S., Taguchi, T., Phys. Rev. B51, 2596 (1995)

197. Nozue, Y., Itoh, M., Cho, K., J. Phys. Soc. Jpn. 50, 889 (1981)

198. Lary, J., Goodnick, S., Lugli, P., Shah, J., Oberli, D. Y., Solid State Elect. 32, 1283 (1989)

199. Oberli, D. Y., Shah, J., Damen, T. C., Kuo, J. M., Appl. Phys. Lett. 56, 1239 (1990)

200. Lee, J., Koteles, E. S., Vassell, M. O., Phys. Rev. B 33, 5512 (1986)

201. Hellmann, R., Koch, M., Feldmann, J., Cundiff, S. T., Gobel, E. O., Phys. Rev. B 48, 2847 (1993)

202. Chemla, D. S., Miller, D. A. B., Smith, P. W., Gossard, A. C., Wiegmann, W., IEEE J. Quantum Electron. QE-20, 265 (1984)

203. Gaines, J. M., Drenten, R. R., Haberern, K. W., Marshall, T., Mensz, P., Petruzzello, J., Appl. Phys. Lett. 62, 2462 (1993)

204. Haase, M. A., Baude, J. F., Hagedorn, M. S., Appl. Phys. Lett. 63, 2315 (1993)

205. Ohkawa, K., Karasawa, T., Yamazaki, O., Jpn. J. Appl. Phys. 30, L152 (1991)

206. Ding, J., Jeon, H., Ishihara, T., Hagerott, M., Nurmikko, A. V., Phys. Rev. Lett. 69, 1707 (1992)

207. Flatte, M. E., Runge, E., Ehrenreich, H., Appl. Phys. Lett. 66, 1313 (1995)

208. Klingshirn, C., Haug, H., Phys. Rep. 70, 315 (1981)

209. Nakayma, N., Itoh, S., Ohata, T., Nakano, K., Okuyama, H., Ozawa, M., Ishibashi, A., Electron. Lett. 29, 1488 (1993)

210. Salokatve, A., Jeon, H., Ding, J., Hovinen, M., Nurmikko, A. V., Grillo, D. C., Ringle, M., Otsuka, N., Electron. Lett. 29, 2192 (1993)

211. Hovinen, M., Ding, J., Nurmikko, A. V., Hua, G. C., Grillo, D. C., He, L., Han, J., Gunshor, R. L., Appl. Phys. Lett. 66, 2013 (1995)

212. Guha, S., Depuydt, J. M., Haase, M. A., Qiu, J., Cheng, H., Appl. Phys. Lett. 63, 3107 (1993)

213. Guha, S., Depuydt, J. M., Qiu, J., Hofler, G., Haase, M. A., Wu, B. J., Cheng, H., Appl. Phys. Lett. 63, 3023 (1993)

214. Petruzzello, J., Greenberg, B. L., Cammack, D. A., Dalby, R., J. Appl. Phys. 63, 2299 (1988)

215. Ahearn, J. S., Laird, C., J. Mater. Sci., 12, 699 (1977)

216. Kleiman, J., Park, R. M., Quadri, S. B., J. Appl. Phys. 61, 2067 (1987)

217. Takeuchi, S., Suzuki, K., Maeda, K., Iwanaga, H., Philos. Mag. A 50, 171 (1984)

218. Yao, T., Jpn. J. Appl. Phys. 25, L544 (1986)

219. Ishibashi, A., Mori, Y., Kaneko, K., Kawado, S., Watanabe, N., Phys. Rev. B33, 2887 (1986)

220. Sood, A. K., Menendez, J., Cardona, M., Ploog, K., Phys. Rev. Lett. 54, 2111 (1985)

221. Cowley, R. A., J. Phys. (Paris) 26, 659 (1965)

222. Tsen, K. T., Morkoc, H., Phys. Rev. B34, 4412 (1986)

223. Tsen, K. T., Morkoc, H., Phys. Rev. B37, 7137 (1988)

224. Tsen, K. T., Joshi, R. P., Ferry, D. K., Morkoc, H., Phys. Rev. B39, 1446 (1989)

225. Elsasser, T., Bauerle, R. J., Kaiser, W., Solid State Elect. 32, 1701 (1989)

226. Becker, P. C., Lee, D., Johnson, A. M., Phys. Rev. Lett. 68, 1876 (1992)

227. Kash, J. A., Tsang, J. C., Hvam, J. M., Phys. Rev. Lett. 54, 2151 (1985)

228. Dexter, D. L. in Solid State Physics vol.6 (ed. Seitz and Turnbull), Academic Press, 1958

229. Brito Cruz, C., Gordon, G. P., Becker, P. C., Fork, R. L., Shank, C. V., IEEE J. Quantum Electron., vol. 24, p.261, 1988

230. Koch, S. W., Peyghambarian, N., Lindberg, M., Fluegel, B., in Optical Switching in Low Dimensional Systems (eds, Haug and Banyai), p. 139, Plenum Press, New York and London, 1988

231. Chemla, D. S., in in Optical Switching in Low Dimensional Systems (eds, Haug and Banyai), p. 129, Plenum Press, New York and London, 1988

232. Schmitt-Rink, S., Chemla, D. S., Miller, D. A. B., Phys. Rev. B32, 6601 (1985)

233. Adachi, S., Taguchi, T., Phys. Rev. B 43, 9569 (1991)

234. Jarasiunas, K., Gerritsen, H. J., Appl. Phys. Lett. 33, 190 (1978)

235. Mitsuyu, T., Ohkawa, K., Yamazaki, O., Appl. Phys. Lett. 49, 1348 (1986)

236. Shahzad, K., Phys. Rev. B38, 8309, 1988

237. Rashba, E. I., Gurgenishvili, G. E., Sov. Phys. Solid State 4, 759 (1962)

BIOGRAPHICAL SKETCH

Li Wang was born in Liaoning Province, China on December 29, 1971. She attended Central Institute of Science & Technology from 1988-1991 and received her bachelor degree in applied physics. Li came to the US in 1991 as an exchange student at North Central College in Illinois and received another bachelor degree in physics there in 1992. Afterwards, she entered the Ph.D program in materials science in the Department of Materials Science and Engineering at the University of Florida. She learned a large amount of new knowledge from working on her Ph.D research project under the guidance of Dr. Joseph Simmons. Li is always dedicated to science and spends most of her time on learning and researching. She hopes that her future career will fulfill her goal of being an excellent scientist.

I certify that I have read this study and that in my opinion it conforms to acceptable standards of scholarly presentation and is fully adequate, in scope and quality, as a dissertation for the degree of Doctor of Philosophy.

Joseph H. Simmons, Chairman
Professor of Materials Science and Engineering

I certify that I have read this study and that in my opinion it conforms to acceptable standards of scholarly presentation and is fully adequate, in scope and quality, as a dissertation for the degree of Doctor of Philosophy.

Larry M. Hench
Graduate Research Professor of Materials Science and Engineering

I certify that I have read this study and that in my opinion it conforms to acceptable standards of scholarly presentation and is fully adequate, in scope and quality, as a dissertation for the degree of Doctor of Philosophy.

Robert M. Park
Professor of Materials Science and Engineering

I certify that I have read this study and that in my opinion it conforms to acceptable standards of scholarly presentation and is fully adequate, in scope and quality, as a dissertation for the degree of Doctor of Philosophy.

Paul H. Holloway
Professor of Materials Science and Engineering

I certify that I have read this study and that in my opinion it conforms to acceptable standards of scholarly presentation and is fully adequate, in scope and quality, as a dissertation for the degree of Doctor of Philosophy.

John M. Graybeal
Associate Professor of Physics

This dissertation was submitted to the Graduate Faculty of the College of Engineering and to the Graduate School and was accepted as partial fulfillment of the requirements for the degree of Doctor of Philosophy.

May, 1996

Winfred M. Phillips
Dean, College of Engineering

Karen A. Holbrook
Dean, Graduate School